Measurement of organ volume using three dimensional ultrasound

by Stephen William Hughes

King's College

submitted for
The degree of Doctor of Philosophy

University of London

July 1997

Abstract

A system has been developed for calculating volume from a sequence of multiplanar two dimensional ultrasound images. Ultrasound image capture is via a video digitising card installed in a personal computer. Regions of interest are transformed from 2D image space to 3D space using position and orientation data obtained from an electromagnetic device (Fastrak, Polhemus Inc, VT) attached to the ultrasound probe. The accuracy of the system was assessed by scanning 10 water filled balloons (13 - 141 ml), 10 kidneys (147 - 200 ml) and 16 fetal livers (8 - 37 ml) immersed in water using an Acuson 128XP/10 (5 MHz curvilinear probe). Volume was calculated using the ellipsoid and planimetry methods, two tetrahedral methods, and two integral methods - a ray tracing algorithm and one based on Gauss' theorem. Actual volume was estimated by weighing (balloons) and water displacement (kidneys and livers). The mean percentage error (± one standard deviation) for the ray tracing algorithm was 0.9 ± 2.4%, 2.7 ± 2.3%, 6.6 ± 5.4% for balloons, kidneys and livers respectively. Four sets of 10 kidneys were scanned using three scan techniques on four different ultrasound machines of varying image quality. There was no significant difference between scan techniques or machines. Twelve of the 16 fetal livers were scanned by computed tomography and magnetic resonance. The mean percentage errors were 5.3 ± 4.7%, -3.1 ± 9.6%, -0.03 ± 9.7 for ultrasound (radial scans, ray volumes), magnetic resonance and X-ray computed tomography (voxel counting) respectively. Tests carried out on the Fastrak showed that it is suitable for use in a clinical environment if care is exercised. These *in vitro* studies suggest that the system has the potential to be a useful tool in measuring organ volume *in vivo*.

Contents

Figures

Tables

6.4 The mean and standard deviation of the percentage error for all four machines for the radial scans.

6.5 The mean and standard deviation of the slice separation and the distance between outline points for the kidneys scanned on the Tosbee machine.

6.6 Mean and standard deviation of the absolute (ml) and percentage error for the four volume estimation algorithms for each ultrasound scan technique on the 16 livers.

6.7 Mean and standard deviation of the absolute (ml) and percentage error for voxel count and planimetry volumes for 11 CT and 12 MR livers.

7.1 Accuracy and resolution values (mm) for ultrasound scanners. LSCA = Large Scale Caliper Accuracy.

7.2 The weight, overflow and level volume values.

7.3 Repeatability of the level, overflow and weighing displacement methods of measuring volume expressed as the mean ± SD of the difference in ml between two successive measurements.

7.4 Agreement between the level, overflow and weighing displacement methods of measuring volume expressed as the mean ± SD of the difference between measurments made by two of the techniques.

7.5 Agreement between voxel counting and the three displacement methods of calculating volume.

8.1 Summary of the advatages and disadvantages of the various volume algorithms.

CHAPTER 1

Introduction

1.1 Volume measurement

In medicine, abnormal volume is often an indication of impaired organ function. For example, an abnormally enlarged prostate gland is indicative of benign prostatic hyperplasia or (more rarely) cancer. The volume fraction of blood ejected by the heart per beat (ejection fraction) is a very important measure of cardiac function. A larger than normal kidney could be the result of cancer, or, in the case of a transplanted kidney, indicate rejection. Fetal volumes are measured in utero using ultrasound to try to identify babies that are growth retarded (intra-uterine growth retardation or IUGR).

However, in medicine, changes in volume are often more important that absolute volume. For example, it is well known that malignant tumours have a higher growth rate than benign tumours. Therefore a rapidly growing neoplasm is of greater clinical concern than one which is more or less static.

Any tomographic imaging modality (i.e. techniques that produce cross-sectional images of the body) can be used to calculate organ volume. The requirements are that the image calibration factors in the x and y directions are known (i.e. pixel size) and also the separation between image planes. The accuracy of measuring volume will primarily depend on the ratio of the pixel size to the dimensions of the organ in the image, and also the number of image planes sampling the organ. The principal tomographic imaging modalities are ultrasound (US), X-ray computed tomography (CT) and magnetic resonance (MR) imaging. There are others, for example, positron emission tomography (PET), single photon emission computed tomography (SPECT), and applied potential tomography (APT). However PET and APT are physiological rather than anatomical imaging modalities and so will not be discussed further.

1.2 The place of ultrasound in medical imaging

Ultrasound imaging has become established as a major tomographic imaging modality alongside X-ray computed tomography (CT) and magnetic resonance (MR) imaging. No one imaging modality is inherently superior to the other, rather they are complimentary, each has its own strengths and weaknesses. Broadly speaking, CT is the best modality for imaging bone, and MR for soft tissues. Ultrasound can only be used for imaging soft tissues, such as the heart, eyes, liver, spleen, gall bladder, stomach, kidneys, bladder, intestines, prostate gland (men), cervix and uterus (women). It is also used extensively in vascular imaging, for example the carotid arteries in the neck, and the veins in the legs - typically to check for blood clots. Ultrasound is particularly useful for measuring flow using the Doppler principle. Flow can be measured using helical CT after injection of a suitable contrast agent, and also by magnetic spin labeling in MR. However CT and MR do not have the same convenience as US.

As a result, ultrasound imaging generally has wider use than CT or MR for a number of reasons. The capital cost of ultrasound imaging equipment is less than either CT or MR. In addition a high cost is required for equipping a suitable room to receive a CT or MR scanner (in some cases the building costs are comparable to the cost of the scanner). Ultrasound machines are much cheaper to maintain than CT or MR scanners.

Hospitals generally have many more ultrasound scanners than CT or MR units, for example, at Guy's and St. Thomas' Hospitals there are three CT and three MR scanners but of the order of 100 ultrasound machines. The cost of ultrasound equipment is low enough to enable ownership by individual wards or departments. In contrast, CT and MR machines are nearly always in centralised units (e.g. the radiology department).

1.3 Three dimensional ultrasound

The term three dimensional imaging is generally applied to all systems that acquire sequences of transverse 2D images of known position and orientation. This technique is sometimes referred to as 'two-and-a-half D' imaging. However, as the separation of the image planes decreases the image data set becomes more truly 3D. Both CT and MR scanners generate sequences of parallel images of known separation from which it is possible to readily extract ROIs and carry out surface and volume rendering of the image

data. Ultrasound images are generally acquired using a hand held probe, therefore the spatial relationship of the images is unknown. To overcome this problem, various techniques have been developed for registering ultrasound images, (which will be described in more detail in the review section of this chapter).

1.4 Safety issues

The relative safety of the imaging modalities is an important issue to discuss. There are two strands to the discussion. The first is, why use US instead of MR or CT to measure volume? In some applications, especially obstetric use, CT and MR pose unacceptable risks to the fetus. US is considered to be inherently safer than either CT or MR. However, it could be countered that since the absolute safety of ultrasound has been called into question, it is unethical to add to the risk by performing 3D-US studies. This is on the assumption that 3D imaging studies of any modality result in a higher dose of radiation than a 2D study. This is certainly true for CT studies compared to plain X-rays, however, it is not necessarily true of ultrasound. It should be born in mind that US and CT images are acquired quite differently. In CT, the number of images to be acquired is carefully planned (in conjunction with a scout film); in contrast, an ultrasound the probe is moved more or less randomly over a wide volume as the ultrasonographer seeks appropriate images to hardcopy. Obstetric ultrasound sessions usually last for several minutes, but 3D acquisitions can be carried out in a fraction of this time (10 s for example), therefore the fractional increase in dose is very small.

Ultrasound is the only imaging modality used extensively in obstetrics. The main reasons being safety, convenience and cost. CT scans are never (knowingly) carried out on fetuses because of the radiation risks. It is recommended that MR is not used on fetuses during the first trimester (12 weeks) the period known as *organogenesis* as the magnetic fields may disturb the morphogenic processes (Saunders, 1991).

However, it is possible that neural tissue remains susceptible to magnetic and thermal effects for much longer (even neonates may be susceptible). This could be due to the induction of ion movement by the gradient field or heating (by frequencies over 100 kHz). One study (Pleet et al. 1981), particularly relevant to the current discussion, has found that mothers suffering from fever for a period of one or two days at between four

and 14 weeks gestation had babies with neural and facial defects. However, it may be that prolonged periods of thermal elevation are required to produce defects, as is the case with fever, rather than short periods, for example, induced by ultrasound.

Heating effects have a bearing on the safety of ultrasound as ultrasound induces heating in the medium of propagation. Ultrasound is used therapeutically to induce heating to improve local circulation (damaged muscles for example). Diagnostic ultrasound units (especially Doppler) are now reaching the power output of therapeutic machines, therefore some heating must be occurring. It is know that the body can respond to a relatively small increase in local temperature, for instance only a $\sim 1^{o}$ C is required to increase the blood flow to maintain thermal homeostasis. Apparently locally induced damage (thermal, cavitation, streaming, shearing) stimulates angiogenesis. These effects are beneficial in wound healing, but could be damaging to the fetus. Embryos, fetuses and neonates are not able to maintain homeostasis as well as children and adults, therefore any elevation in temperature is likely to persist for longer. Thermal damage is also more likely to occur in avascular regions.

Another possible mechanism for causing damage is cavitation (Docker and Duck, 1991) induced in regions of high negative pressure (i.e. rarefaction). Fluids, or at higher intensities, tissues, are torn apart by the negative pressure, producing vacuum bubbles into which gases infuse over a short space of time. The bubbles then collapse producing a shock wave of high intensity (analogous to a thunderclap) that can damage nearby tissues. Cavitation effects are known to be enhanced in fluids containing gas bubbles (a kind of seeding effect), which includes all body fluids to some extent. Therefore it is possible that cavitation could occur within the amniotic fluid, but close enough to the embryo or fetus to cause damage. In addition, mechanical damage could be caused by streaming (high velocity jets of fluid impelled by the ultrasound beam).

In spite of these potential bio-effects of ultrasound, the prudent use of ultrasound is considered to be safe (Wells 1987). However, a distinction should be drawn between imaging and Doppler ultrasound. Ultrasound intensities tend to be lower for diagnostic imaging than for Doppler and are therefore of less concern (Henderson et al. 1995). More

care probably needs to be taken with Doppler imaging as significant temperature rises can be induced within tissues which could be damaging to a fetus.

It should be born in mind that to date ultrasound examinations have been carried on several million fetuses, many of which have reached adulthood, with no obvious ill effects. However, a report presented by a Norwegian group (Salvesen et al. 1993 a) has shown a significant increase in left-handedness in babies born to a group of mothers who received two extra scans at 19 and 32 weeks of pregnancy compared to a control group. Subsequently it has been pointed out that some kind of statistically significant effect is bound to be found in this type of study just by chance. The same group of children (Salvesen et al. 1993 b) were subjected to dyslexia tests between the ages of eight and nine years and the results showed no difference in reading and spelling and intelligence scores between the two groups.

Another study reported in the same year (Newnham et al. 1993) by a group in Western Australia showed a small (25g), but significant reduction in the birth in a group of mothers who received on average five ultrasound scans in pregnancy compared to a single scan for a control group. However, there was no associated increase in mortality or morbidity in the intensive scan group. This study set out to test the hypothesis that frequent scanning improves the outcome for complicated pregnancies. The authors have shown that this is not the case and as a side effect discovered the link between frequency of ultrasound scanning and low birth rate. This study has been criticised on the grounds that it was not designed to investigate the relation between ultrasound and growth and therefore the results may just be statistical.

It is interesting to note that in the Australian group, there were 10 deaths due to fetal abnormalities in the control group compared to only three in the intensive scan group. The authors put this down to chance. One wonders whether the same interpretation would have been applied if the results were the other way around.

In relation to the studies above, it is possible that other factors are being brought into play other than ultrasound, for example, were mothers who received more examinations more anxious about there babies for some reason - perhaps just by visiting a clinic more often?

Another complicating factor is that mothers with problem pregnancies generally receive a greater number of ultrasound examinations than those with uncomplicated pregnancies. Any abnormalities could be either the cause or effect of a difficult pregnancy, and be unrelated to any physical effects of the ultrasound.

Other studies have shown no adverse effects of ultrasound even with very intensive scanning. For example, Zimmermann et al. (1993) exposed 19 mothers for between six and nine hours and 12 mothers for 20 hours at periods *before* 20 weeks gestation for investigating fetal movement patterns. This is far greater exposure than most mothers receive, and the fetus is thought to be more susceptible to damage below 20 weeks than at higher gestational ages.

Care has to be exercised when a number of independent research groups are investigating the same phenomenon. Most research groups use a p value of 0.05 for assessing the significance of their results. If the results achieved in a particular experiment have a probability of occurring only 1 in 20 times by chance, they are generally assumed to be significant. However, if 20 independent groups were to carry out the same experiment, the probability of at least one of the groups achieving a significant result by chance is very high. Wells et al (1986) stress the need for better experimental design to more effectively address the safety, or otherwise, of ultrasound.

Guidelines produced by the British Institute of Radiology (Docker and Duck, 1991) recommend that when a patient is scanned, if possible, the power output is kept to the minimum level required to produce a diagnostically useful image. (In practice, this might involve reducing the power output for a slim patient, as thinner tissue layers attenuate the beam less). The dwell time on any particular structure should be kept to a minimum. This reduces the likelihood of excessive heating and the build up of standing waves, which can be particularly damaging at tissue interfaces. Excessive dwell times can occur in routine clinical use, for example, when an ultrasonographer is attempting to determine the gender of a fetus. There is general tendency is for the power output of succeeding generations of ultrasound machines to increase. Therefore, there is the need for more work on the safety issues.

In summary it can be said that at present there is no evidence that ultrasound is harmful to the fetus and therefore is totally safe if care is taken. Admittedly some studies suggest that ultrasound has some influence on growth - i.e. a slight prevalence of non right-handedness and tiny decrease in mean birth weight. However, even if these effects are real, do they really matter?

1.5 Aims of the project

The primary purpose of this project was to develop an easy to use system for estimating organ volumes from a sequence of multiplanar two dimensional (2D) ultrasound images acquired using a hand-held ultrasound probe. A secondary aim was to develop a low cost system, by using off-the-shelf components, which could be connected to a wide range of 2D scanners. Currently available 3D scanners are much more expensive (~ £180,000) than 2D machines and therefore are beyond the reach of many research budgets. 3D machines that are available are likely to have a high clinical workload, with limited access for research. However, hospital and university research groups often do have access to older scanners no longer in routine clinical use. A low cost 3D system could be of value to such groups. The system was also designed to be portable on a trolley to enable it to be used on a variety of ultrasound scanners in different locations.

1.6 Structure of the thesis

This thesis is divided up into eight chapters. The second part of this chapter briefly surveys techniques which have been developed for registering ultrasound images and calculating volume from regions of interest (ROIs). The second chapter describes the algorithms developed in this project for registering images, meshing ROIs, and calculating volume. The third chapter covers theoretical and experimental validation of the volume calculation algorithms described in chapter 2. The fourth chapter briefly describes the system hardware and software. In the fifth chapter, the accuracy of the electromagnetic localiser system is assessed. The sixth chapter covers the main *in vitro* experiments. Chapter seven includes a discussion of some of the factors which affect the overall error in measuring volume using 3D ultrasound. The eighth, concluding chapter summarises the main findings of this project and offers suggestions for future work.

1.7 Review of methods for registering ultrasound images

This section reviews techniques reported in the literature for registering planar and multiplanar ultrasound images and algorithms for calculating volume from regions of interest (ROIs). Advantages and disadvantages of the various techniques and algorithms are discussed.

1.7.1 Parallel scanning

An ultrasound transducer can be attached to a mechanism to ensure that parallel images of known separation are acquired. Klein et al (1993) describe a mechanically driven frame which scans a transducer across the body to acquire parallel images. The height is adjusted to follow body contours and maintain good skin contact. The authors present an example of a surface reconstruction of a fetal face scanned in this manner.

Blankenhorn, et al. (1983) attached an 8 MHz transducer to a rack and pinion mechanism for scanning carotid arteries as a means of assessing the degree of athersclerosis. Picot, et al. (1993), Pretorius, et al. (1992) described a parallel system for imaging blood vessels. Matsumoto et al. 1981, Raichlen et al. 1986) describe a similar system for the heart. The male prostate gland has also been imaged in this way (Hastak, et al. 1982). Hell et al. (1993) describe a similar parallel system for producing surface reconstructions of facial anatomy for planning maxillo-facial surgery.

An advantage of parallel image acquisition is that ROI volumes can be calculated with relative ease, and surface and volume rendering techniques can be readily applied. A disadvantage is that the site must be carefully selected and a water bolus may be required, which will degrade the image. Another problem is that it may not be possible to image the whole structure from the available insonation window.

1.7.2 Pull-back systems

Motorised pull-back systems for use with intracavity transducers have been reported for imaging the prostate (Sehgal. et al. 1993) and female urethra (Kirschener et al. 1994). A transesophageal system has also been developed by Wollschlager et al. (1989) for imaging the heart. In motorised pull-back systems, the distance between image planes is found by multiplying the pull-back velocity by the time interval between image acquisitions. If the catheter is pulled back manually, the image separation is measured using a scale beside the catheter.

Intravascular pull-back systems have also been developed, for example, as described by Ennis et al. (1993) and Rosenfield et al. (1991,1992). Some systems involve rotating the catheter about the central axis (Kok-Hwee et al. 1994). Most intra-vascular catheters have a rotating mirror at the end of the catheter which deflects the ultrasound beam produced by a piezoelectric element also at the end of the catheter. The ultrasound beam is deflected at right angles to the catheter axis and sweeps around the catheter in a similar manner to a light-house beam.

Work is being done on producing a catheter with a number of piezoelectric elements (about 64) arranged equally around the perimeter of the catheter (private communication with a member of Intravascular Research, Putney, London). Catheters of this design can be made smaller than those of the rotating mirror type and therefore can be deployed in smaller vessels and cavities (and so could, for example, penetrate further down the coronary artery tree).

1.7.3 Transducer angulation

Gosh et al. (1982), Pini et al. (1989) and Klein et al (1993) describe a system in which the transducer is held in a rig allowing only central axis rotation of the transducer. Fine et al. (1991) describe a similar technique using a hand held transducer. Knowledge of the angle between image planes enables images to be registered. The sections through the organ are similar to orange segments.

Brann et al (1990 a,b) describe a technique for calculating the volume of brain ventricles in premature neonates. The transducer, attached to a protractor, is held against the head

and swept through an angle such that image planes have a common origin. A cylindrical coordinate system is used to define the position of image points.

1.7.4 Articulating arms

Any system in which the ultrasound probe is attached to a mechanical device obviously restricts freedom of movement in some way. This problem can be overcome to some extent by connecting the transducer to an articulated arm which records the position and orientation as the transducer is scanned across the body. Sawada et al. (1983) describe an arm with three axes of rotation with the transducer able to rotate about its central axis. The angle of the three joints was measured using potentiometers. The angle of the transducer at the end of the arm was measured by a protractor, which is read by visual inspection. The system was used to measure left ventricular volumes in 11 excised porcine hearts. Such arms usually have variable potentiometers placed at each joint to measure limb angle. The real-world location and orientation of the tip of the probe can be easily calculated from the length of each limb and angle of each joint.

Martin et al. (1979, 1990, 1993) developed a 2D phased array transesophageal probe capable of being mechanically swept through $\pm 30^{o}$ by a pulley system. The system was developed for anaesthetists to monitor the cardiac output before and during cardiac surgery. An advantage of this system is that the probe can be held in place for several hours.

1.7.5 Dedicated 3D transducers

In principle, dedicated 3D scanners are no different from many of the systems reviewed so far in that a 2D transducer is mechanically moved to acquire images through a volume. The main difference is that the transducer is housed in a case containing a mechanism for rotating or translating the array. The coordinate system is referenced to the transducer case. In some cases the transducer is attached to an external sweeping mechanism such as a stepping motor.

At present not many dedicated 3D volume scanners are commercially available, probably due to restrictions imposed by the Federal Drugs Administration in the US. The FDA has decreed that 3D ultrasound has to be considered as a new imaging modality and not just

an extension of 2D ultrasound (private communication with a Kretztechnik representative 1996). Hence, the first truly commercially available 3D scanner, the Combison 530, was produced by an Austrian company (Kretztechnik). This has a 2D phased array transducer housed in a case and is swept through $\pm 30^{o}$ producing a 60^{o} insonation wedge.

Hamper et al. (1994) describe the use of an experimental dedicated 3D scanner developed by Acoustic Imaging (Tempe, Arizona, USA). Standard 3.5, 5 and 7.5 MHz transducers were modified so that they could be rotated $\pm 30^{o}$ by a stepping motor. Between 24 and 60 images are acquired in 10-15 seconds. Linear interpolation was carried out to produce orthogonal images including C-plane images normal to the central axis of the ultrasound beam. The authors used the system to compare the usefulness of 3D-US with 2D-US in imaging a wide variety of normal and abnormal anatomy in adults and fetuses. The authors concluded that 3D-US does have a part to play in complementing 2D-US. They also found that procedures were easier to perform and interpret, and enabled cross-sectional views to be obtained that are not possible with 2D-US. However, in only a few cases did 3D-US result in diagnoses that could not be obtained with 2D-US. It is important to note that the authors did not carry out any volume or surface rendering, although they could have done so with their image data.

Gilja et al. (1995) carried out an *in vivo* comparison of a 3D ultrasound system and MR in estimating the volume of human kidneys. They attached a commercially available sector scanner to a custom built tilt motor which produced an 88^{o} insonation wedge in 81 steps.

Blaas et al (1995) developed a system using a mechanical 7.5 MHz annular array transvaginal transducer attached to a stepping motor which rotated the transducer 180^{o} about its central axis acquiring 132 sector images in 4 s. The image data was reformatted into parallel slices and ROIs drawn around brain cavities in human embryos to produce exquisite 3D reconstructions.

1.7.6 Remote systems

To allow more or less complete freedom of movement (apart from cable attachments), remote 3D tracking devices are required. Remote acoustic localiser systems are described by Brinkley et al. (1978), King et al. (1990), Moritz et al. (1983) and Levine et al. (1989). Acoustic system utilise three spark gaps positioned around the perimeter of a

Perspex disc connected to the transducer, and three microphones placed at the ends and the junction of a stationary right-angled bar. The distance between the microphones and spark gaps is calculated from the time-of-flight of the sound. The receivers are tuned to 100 kHz, which is above the frequency range of normal sounds in a clinic, thereby reducing the likelihood of interference. Acoustic velocity is a function of temperature and humidity, temperature being the most important factor. As the velocity of sound in air changes at a rate of about 2% per 10^{o}C, to avoid significant errors, the air temperature must be continually monitored. Also, there must be a clear path between the spark gaps and microphones. The accuracy of acoustic system is of the order of $\pm$ 1 mm and $\pm 1^{o}$ for distance and angle respectively.

Electromagnetic systems for image registration are reported by Gardener et al (1991), Lees et al. (1991, 1993), Kelly et al. (1992), and Hodges et al. (1994). In all of these systems, an electromagnetic signal is emitted from a stationary transmitter, and detected by a mobile receiver. Both the transmitter and receiver are constructed from three mutually orthogonal coils of copper wire. The distance and orientation of the receiver are calculated from the relative strength of the signals received in each sensing coil. The advantage of electromagnetic systems is that the receiver is small and light and so can easily be attached to an ultrasound transducer. A disadvantage is that nearby metal and stray electromagnetic signals can produce errors in the measurements.

1.8 Review of volume algorithms

1.8.1 Geometric models

Before the advent of tomographic imaging modalities, attempts were made to estimate the volume of an organ or structure from linear dimensions taken from plain X-rays. For instance, Keats and Enge (1965), estimated cardiac volume from plane X-rays. McLachlan et al. (1968) estimated the volume of pituitary glands from plane X-rays of the sella turcica. Austin and Gooding, (1971), describe the measurement of skull size in children using X-rays.

The most commonly employed geometric model used in medicine is the ellipsoid model. This involves measuring the length, breadth and height of the organ and calculating the volume of an ellipsoid having these dimensions. The ellipsoid method is commonly employed in calculating the volume of the left ventricle using cineangiography and ultrasound, (Dodge et al. 1960, Geuret et al 1983, Schiller et al. 1979, Teichholz et al. 1974, Tortoledo et al 1983, Wyatt et al 1979,1980). Prostate volumes are also routinely estimated from 2D ultrasound images (Blum et al. 1985, Littrup et al. 1991, Styles et al. 1988). The ellipsoid method has also been applied to the uterus (Levine et al. 1979).

The ellipsoid technique is easy to implement, but can lead to significant errors if the organ is not ellipsoidal in shape, which is often the case, especially if an organ is diseased. Another disadvantage is that the ellipsoid method is dependent on the correct views of the organ being obtained. A slight deviation can lead to large errors, even if the organ is nearly ellipsoidal. In some cases, a combination of linear dimensions are used to calculate volume. For example, regression equations are often used to estimate fetal volume *in utero* from the bi-parital diameter, abdominal circumference and femur length (Shinozuka et al. 1987).

Work on the ellipsoid method, or some variant, continues even with the availability of tomographic image modalities. For example, Schlesinger et al (1994) obtained a good correlation ($r = 0.97$) between the product of length, width and thickness of the spleen in 50 children and volume calculated from axial CT scans. Estimating volume using geometric models is obviously to be preferred to acquiring a sequence of transverse images, especially if this reduces the radiation dose received by the patient. Ultrasound is a convenient modality for obtaining the images required for application of a geometric model.

1.8.2 Planimetry

The planimetry technique, in its purest form, is used in cases where parallel images are available. The organ is delineated on each slice, and the volume of the slice calculated by multiplying the area by the local slice thickness. If slices are parallel, the volume of each slice is found multiplying by the area of each ROI by slice thickness (Bartsch et al. 1982,

Eaton et al. 1979, Geirson et al. 1982, Helak and Reichek, 1981, Littrup et al. 1991, Raichlen et al. 1986, Matsumoto et al. 1981, Hastak et al. 1982).

If slices are not parallel, then various options are available, for example, re-sample, or re-format ROIs into parallel outlines normal to the long axis of the organ. This approach is described by Brinkley et al (1978), Geiser et al (1980), Linker et al (1986), Nanda et al (1982), Sawada et al (1983). Another option is to decompose the structure into regular geometrical elements, for example, radial wedges (like sections of an orange), as described by Moritz et al (1983), Martin et al (1990), Jiang et al (1994).

Another approach is to work directly on the multi-planar images without reformatting. Watanabe (1982) has developed an algorithm for applying the planimetry method to multi-planar ROIs. The technique involves creating ROIs and calculating centroids. Vector areas are calculated from the dot product of the ROI area and vectors connecting adjacent ROI centroids. Watanabe validated the algorithm on computer generated phantoms using six different cutting modes and obtained an overall error of less than 3% when 10 slices were used.

Sawada et al. (1983) used an articulating arm system to measure the volume of left ventricles in 11 excised porcine hearts. The hearts were placed in normal saline at 37^{o}C about 10 short-axis images were taken through each left ventricle and outlined on computer. The ROI points were connected into triangular and quadrilateral surface elements. Each left ventricular object was then divided up into 50 parallel ROIs normal to the long axis of the ventricle. In this case the long axis was defined as the line joining the centroids of the first and last short axis images for a particular ventricle.

The total volume of each ventricle was found simply by summing the ROI areas and multiplying by the separation of ROIs. Actual left ventricular volume was measured by water displacement. The results (mean $\pm$ SD) for the 11 hearts were 230.4 $\pm$ 30.9 ml and 234.4 $\pm$ 29.3 ml for water displacement and ultrasound respectively, therefore, on average, ultrasound overestimated volume by 1.7%. Regression analysis yielded a correlation coefficient of $r = 0.928$.

Basset et al. (1991) scanned a selection of agar gel phantoms with transverse and sagittal images using a transrectal probe. The aim of this study was to compare the accuracy of measuring prostate volume using transverse and sagittal images. ROIs were outlined and the algorithm of Watanabe used to obtain the volume. An overall accuracy of 10 ± 2% was obtained. However, some results were better than this, for example, the results for a cylindrical phantom were -4.8 ± 0.55% and -5.7 ± 1% for transverse and sagittal scans respectively.

The limitations of Watanabe's technique is that the slices must be close together with little difference between the angle of successive image planes, and image planes should be approximately normal to the long axis of the organ. However, an advantage of the planimetry technique is ROI points do not need to be connected into a mesh.

A technique described by Brann et al (1990) is a variation on the planimetry scheme. The method can be classified as planimetry as the area of each ROI is used in the calculation. Brann used a cylindrical coordinate system to register images and the trapezoid rule to approximate a triple volume integral. *In vitro* validation was performed on 17 water filled latex balloons embedded in gelatin containing talc and produced a correlation coefficient of 0.96. *In vivo* validation was performed by measuring the volume of the ventricles of six hydrocephalic neonates before and after fluid drainage, a correlation coefficient of 0.91 was obtained. Brann's algorithm takes into account the complicated shape of the ventricle and can handle multiple ROIs in the same image plane.

1.8.3 Volume elements

A number of techniques have been reported for dividing organs into volume elements. These techniques can be sub-divided into exact and inexact methods. Exact methods involve drawing ROIs on a series of image planes through the object and connecting the ROI points into a triangular surface mesh. Inexact methods involve approximating the shape of the object with curved geometrical elements, for example, cylindrical sections.

Martin et al. (1993) acquired multiplanar cardiac images using a trans-oesophageal transducer. End-diastolic (ED) and end-systolic (ES) ROIs were traced manually, and the centroid of the ED and ES chambers calculated. Surface points were interpolated and the

object divided into pyramidal regions of equal solid angle. The volume of each pyramid was found by multiplying the volume of a sphere of diameter equal to the local radius by the solid angle. In effect, the ventricular wall was modeled by quadrilateral spherical sections of varying radii. An advantage of this technique is that normalised regional ejection fractions can be calculated.

This technique depends on surface elements being approximately normal to a line projecting from the centroid to the surface element, and no sections of the surface must be obscured. Another technique involves reformatting outlines into a series of cylindrical wedges (Martin et al. 1990). The wedges radiate out from the central axis of the organ to the surface, the assumption is made that the curvature of each surface element is approximately cylindrical.

Another technique involves scanning the organ with a sequence of radial scans that have a constant axis of rotation (Watanabe et al. 1981). ROI points are connected to form a triangle mesh describing the surface of the organ. An origin is chosen on the rotation axis of the transducer and tetrahedra formed by connecting the origin to each triangle vertex. The volume of the organ is calculated by subtracting the total volume of tetrahedra facing the origin from the total volume of tetrahedra facing away from the origin.

Blaas et al (1995) drew parallel ROIs around embryonic brain cavities *in utero* and used a polyhedral technique to calculate volume. They do not give a precise description of the technique - presumably polyhedra were constructed in strips utilising adjacent ROIs.

Liver volume has been determined by taking a series of images at 10^0 intervals, with each image aimed at a common point in the spinal chord (Rasmussen 1972). In this case registration was performed by actually marking the 10^0 lines on a protractor. The transducer was attached to a mechanical arm for stabilisation. The liver was modelled as a series of 10^0 wedges. The radii of the inner and outer surfaces of each wedge were calculated with respect to the axis of rotation.

Another volume technique described by (Cook et al. 1980) involves filling the space between adjacent ROIs with tetrahedra constructed by connecting triangles vertices to

ROI centroids. The limitations of this technique are that an ROI must not cross over itself and ROIs must not intersect each other. If an object contains holes then the volume of these holes must be calculated separately and subtracted from the total volume.

Martin et al. (1983) acquired multiplanar sections through 10 formalin-fixed canine hearts. Complete, or in-complete, ventricular ROIs were drawn on the images and converted into cylindrical coordinates. The points in each ROI were connected to form a three dimensional line - i.e. the first point is connected to the second, the second to the third and so on. Polar planes were passed through this collection of lines and the intercepts calculated. The intercept points were connected to form ROIs of constant angle (rather like sections of an orange). Volume was found by approximating the triple volume integral by a stack of wedge shaped cylindrical sections. The actual volume of the ventricles was measured by filling the chambers with water from a graduated cylinder, the mean error was 5%. An advantage of this volume algorithm is that over-lapping and in-complete ROIs can be handled.

Gilja et al (1995) scanned 20 healthy volunteers with a 3D-US ultrasound system and MR. Radial images were acquired and reformatted into planar images by tri-linear interpolation. ROIs were outlined manually on the planar images and filled with polyhedra. The accuracy, expressed as the mean difference ± SD, was 155.7 ± 26.4 ml and 171.8 ± 24.6 ml for US and MR respectively, demonstrating that 3D-US is of comparable accuracy to MR.

1.9 Rationale

Many different techniques have been used to register sequences of 2D ultrasound images, either for the purpose of producing qualitative or quantitative 3D images. For this project, it was decided to use the Polhemus Fastrak, following the lead of John Gardners' group at University College Hospital Medical Physics Department. Gardners' group has a successful track record of using the Polhemus to register multi-planar ultrasound images prior to the production of surface rendered images.

An important consideration is that the Fastrak receiver is small and light, and so can be attached unobtrusively to an ultrasound probe. This is particularly important to enable an ultrasonographer is to acquire conventional 2D scans as well as 3D acquisitions without having to remove the receiver attachment. A mechanical device would tend to get in the way, and could possibly fall onto a mother with a danger of harming the baby.

Many groups acquire multi-planar ultrasound images and then reformat the data into parallel planes. Multi-planar reformatting was not chosen for this project as it was felt that significant interpolation errors could arise because of inherent image noise (speckle etc.) and shadowing. Missing parts of a volume or surface reconstruction are not so critical if 3D images are for qualitative viewing only. The human visual system is very good at perceiving structure in images with a low signal to noise ratio. However, missing surface elements could cause errors in volume calculations.

Another consideration was that a large number of closely spaced images would be required to achieve reasonable interpolation which would be computationally time consuming. In contrast, drawing ROIs directly onto multi-planar images carries no computational overhead. This approach also requires fewer images and therefore fewer computer resources (memory etc).

CHAPTER 2

Algorithms

2.1 Introduction

The first part of this chapter describes the algorithm developed by the author for registering multiplanar ultrasound images. The second section describes a triangulation algorithm, also developed by the author, to connect transformed ROI points into a triangular surface mesh, essential for some of the volume calculation algorithms. The last section describes the algorithms used for calculating volume.

Three of the volume algorithms (centroid-terahedral, Gauss and ray tracing), were developed by the author and have not been previously described in the literature. The other three algorithms (ellipsoid, planimetry, slice-tetrahedral) have been previously reported in the literature, but were modified by the author for the purposes of this project.

2.2 Registration of multiplanar images

To transform a point from image space (x_i,y_i) to world space (x_w,$y_{w,}$,z_w) the position of a reference point on the localising sensor and orientation of the coordinate system of the sensor are required. The orientation of the sensor coordinate system is generally defined using one of three methods - Euler angles, direction cosines or quaternions. All three methods are interchageable with each other, but each has its own advantages and disadvantages. For instance, Euler angles are easy to understand, especially when applied to ships - a ship *pitches* up and down, *rolls* from side to side and *yaws* sideways to the direction of travel. Euler angles are appropriate for ships, but not for aircraft, spacecraft, or tracking devices, as there is an ambiguity between yaw and roll at high pitch angles. (If the long axis of an object is pitched near to the vertical, rotation about the long axis becomes equivalent to yaw, and *vice versa*). This ambiguity would not normally be a problem in the case of a ship (unless it was sinking). Euler angles are the most efficient of the three methods at encoding angle as only three numbers are required, as opposed to four and six numbers for quarternions and direction cosines respectively. However,

quarternions are the most robust way of encoding angle and therefore were chosen for this project.

2.2.1 Orientation quarternions

The orientation of an object in space can be described as a rotation (θ) about a vector **v** (figure 2.1).

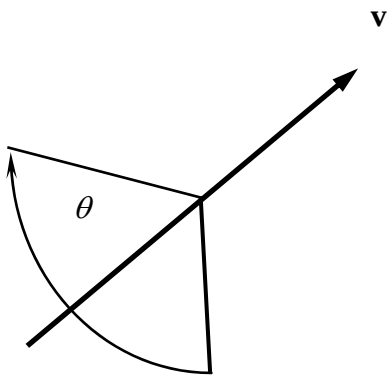

Figure 2.1 **The orientation of an object can be described by a rotation θ around a unit vector** v**.**

The rotation can be described in matrix form:

$$(\theta,\mathbf{v}) \qquad \mathbf{v} = \mathbf{i}x + \mathbf{j}y + \mathbf{k}z \tag{2.1}$$

where θ is the angle of rotation about the unit vector, **v**; x,y,z are the coordinates of a point on the vector, and **i**, **j**, **k** are unit vectors parallel to the x,y and z axes respectively. The sum of the squares of the x,y and z components of a unit vector is unity, hence the term unit vector. For computational convenience the following form of quarternions is often used:

$$\mathbf{Q} = \cos\frac{\theta}{2}, \mathbf{v}\sin\frac{\theta}{2} \tag{2.2}$$

When this scheme is used the quarternion **Q** (a vector quantity) always has a magnitude of unity when the four components are squared, i.e

$$\theta^2 + x^2 + y^2 + z^2 = 1 \tag{2.3}$$

(This follows from the fact that $\sin^2\theta + \cos^2\theta = 1$). The angle ($\theta$) of rotation about the vector is divided by two to avoid ambiguity as the the sine and cosine of angles between 90^o and 180^o are the same as between 90^o and 0^o (for example the sine and cosine of 80^o are the same as for 100^o).

Quarternions and Euler angles are generally converted to direction cosines prior to use in vector calculations. A minimum of six terms are required to describe the orientation of a orthogonal coordinate system using direction cosines. If the orientation of any two axes of a 3D cartesian coordinate system are known then the remaining axis can be found from the cross product of the two known axes.

Orientation quarternions are used to calculate the direction cosines as follows (Cooke et al. 1992). The sensor coordinate system is shown in figure 2.2.

2.2.2 Direction cosines from quarternions

(2.4)

$$
\begin{aligned}
los_x &= Q_0^{\,2} + Q_1^{\,2} - Q_2^{\,2} - Q_3^{\,2} \\
los_y &= 2(Q_3Q_0 + Q_1Q_2) \\
los_z &= 2(Q_1Q_3 - Q_0Q_2)
\end{aligned}
$$

$$
\begin{aligned}
loh_x &= 2(Q_1Q_2 - Q_0Q_3) \\
loh_y &= Q_0^{\,2} - Q_1^{\,2} + Q_2^{\,2} - Q_3^{\,2} \\
loh_z &= 2(Q_1Q_0 + Q_3Q_2)
\end{aligned}
$$

$$
\begin{aligned}
lop_x &= 2(Q_1Q_3 + Q_0Q_2) \\
lop_y &= 2(Q_2Q_3 - Q_0Q_1) \\
lop_z &= Q_0^{\,2} - Q_1^{\,2} - Q_2^{\,2} + Q_3^{\,2}
\end{aligned}
$$

where los_x refers to the x direction cosine of the sensor line-of-sight vector etc.

2.2.3 Connecting image space to world space

The Polhemus Fastrak localiser system used for this project (more details are provided in the next chapter) has the coordinate system as depicted in figure 2.2. A line-of-sight (LOS) vector projects from the front face of the receiver, a line-of-hear (LOH) vector is directed out of the right hand side at right angles to the LOS, and a line-of-plumb (LOP) vector is directed downwards at right angles to both the LOS and LOH vectors. The coordinate system is the same as that generally used for graphs with the +x axis extending to the right of the origin, the +y axis extending above the origin and the +z axis extending out of the page towards the viewer.

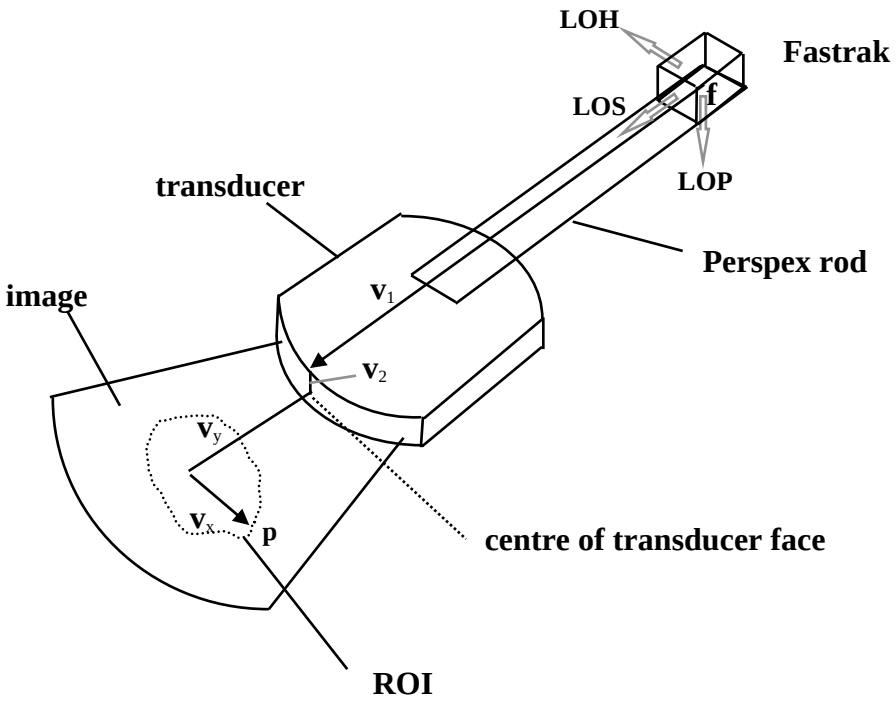

Figure 2.2 Schematic diagram of the Fastrak receiver attached to an ultrasound transducer.

The 3D coordinate of any point within an image is calculated by summing the vectors between the centre of the receiver and a point on the image, as shown in figure 2.2 where;

p = position vector of image point

f = position vector of Fastrak receiver

$\mathbf{v}_1$ = vector projecting from Fastrak receiver to a point above the transducer centre

$\mathbf{v}_2$ = vector projecting from the end of $\mathbf{v}_1$ to the transducer centre

$\mathbf{v}_x$,$\mathbf{v}_y$ = vectors pointing in the same direction as the image x and y axes

t_x,t_y = image coordinates of the centre of the transducer face

c_x,c_y = calibration factors in the x and y direction

Δx, Δy = x,y coordinates of image point relative to the centre of the transducer face

$\Delta x = t_x - x$, $\Delta y = t_y - y$, where x and y represent the image coordinates of a point.

If $\mathbf{v}_1$ is in the LOS direction, $\mathbf{v}_2$ in the LOP direction, $\mathbf{v}_x$ in the LOH direction and $\mathbf{v}_y$ in the LOS direction, the coordinates of an image point in Fastrak space are given by:

(2.5)

$$p_x = f_x + los_x|v_1| + lop_x|v_2| + los_x \Delta yc_y + loh_x \Delta xc_x$$

$$p_y = f_y + los_y|v_1| + lop_y|v_2| + los_y \Delta yc_y + loh_y \Delta xc_x$$

$$p_z = f_z + los_z|v_1| + lop_z|v_2| + los_z \Delta yc_y + loh_z \Delta xc_x$$

The above equations can be converted into the more convenient matrix form as follows.

Let;

$$
\begin{aligned}
\mathbf{m}_{00} &= loh_x c_x \\
\mathbf{m}_{10} &= los_x c_y \\
\mathbf{m}_{20} &= f_x + los_x \left|\mathbf{v}_1\right| + lop_x \left|\mathbf{v}_2\right| \\
\\
\mathbf{m}_{01} &= loh_y c_x \\
\mathbf{m}_{11} &= los_y c_y \\
\mathbf{m}_{21} &= f_y + los_y \left|\mathbf{v}_1\right| + lop_y \left|\mathbf{v}_2\right| \\
\\
\mathbf{m}02 &= loh_z c_x \\
\mathbf{m}_{12} &= los_z c_y \\
\mathbf{m}_{22} &= f_z + los_z \left|\mathbf{v}_1\right| + lop_z \left|\mathbf{v}_2\right|
\end{aligned}
\tag{2.6}
$$

and

$$\mathbf{p}_i = (\Delta x, \Delta y, 1) \tag{2.7}$$

Then

$$\mathbf{f}_i = \mathbf{p}_i \mathbf{m}_S \tag{2.8}$$

where;

$\mathbf{f}_i$ = Fastrak coordinate of ith image point

$\mathbf{p}_i$= coordinate of ith point relative to the centre of the transducer face

$\mathbf{m}_s$= transformation matrix for slice s

The position of the receiver relative to the ultrasound transducer face could be described by more than two vectors if necessary, but this would increase the error in the volume estimate. For example, if the positional error at the end of two vectors is ± 1 mm, the error at the end of the two vectors added together will be ± 2 mm.

The centre of the transducer face is marked on one of the images, and this point assumed to be at the end of vector $\mathbf{v}_2$ projecting to the centre of the transducer face. (If vector $\mathbf{v}_2$ is offset to one side of the centre of the transducer face, then the equivalent point must be marked on the image.) This point becomes the new origin of the image for transformation purposes and is essential for calculating the 3D coordinate of an image point. The x and y axis calibration factors are calculated using scale markers on the ultrasound image. The x,y,z coordinate of a point on the image is calculated by multiplying the x,y image coordinates (relative to the transducer origin) by the unit receiver vectors which happen to be aligned with the x and y axes of the image (in the case shown in figure 2.2, the LOH vector for the x axis and the LOS vector for the y axis). The resultant vector is then added to $\mathbf{v}_1$ and $\mathbf{v}_2$.

If the x axis of the image is anti-parallel to the positive direction of the corresponding receiver axis, the object will be reflected about a line parallel to the y axis that passes through the centre of the transducer face. However, as all points retain their relative position, the calculated volume will not be affected. If, for some reason, the absolute positions of the ROI points are required, the image x axis may have to be reversed (most ultrasound machines have a facility for doing this).

2.3 Triangulation algorithm

The main 3D volume calculation algorithms require the ROI points to be connected into a triangle mesh. A robust triangulation algorithm must be able to handle ROI data in a variety of forms. For instance outlines can be either clockwise or anticlockwise and open or closed. It is also important that triangles do not overlap. In the earlier stages of this project a fairly complicated algorithm was developed to handle these different situations. However, a different approach has now been adopted, which involves pre-processing the ROI data so that it is in the correct form for the meshing algorithm.

The basic approach chosen is that of the 'nearest neighbour'. An assumption is made that the ROIs will be fairly close together and similarly inclined. For this project, only a simple algorithm was used as the objects imaged tended to be single enclosed surfaces. (More complicated objects can be subdivided if necessary). The description of the algorithm has been divided into two sections, the first dealing with pre-processing of the ROI points, and the second the actual meshing algorithm.

2.3.1 Pre-processing

1. Is the ROI open or closed? If the x,y and z coordinates of the first and last points in the ROI are the same then the ROI is closed. If not, an additional point with the same coordinates as the first point is added to the ROI and the variable containing the number of points in the ROI incremented by one.

2. The sense of an ROI is found by creating a triangle from the first two points in the ROI and the ROI centroid. In this case, the ROI centroid need not be exact and so can be taken as the mean of the x, y and z coordinates. The triangle normal is calculated from the cross-product of any two of the triangle edges. Looking down on an ROI drawn on a sheet of paper, the normal of a clock-wise ROI will point into the paper and the normal of an anti-clock-wise ROI will point out of the paper. In this algorithm the ROIs are arbitrarily chosen to be clock-wise. Therefore if any of the ROIs are found to be anti-clockwise, the point order is reversed. Having ROI points in the same sense makes it much easier to avoid the problem of the triangulation algorithm running 'backwards' due to a point being selected 'behind' the current point.

3. In order to improve the uniformity of triangulation ROIs can be interpolated into a number of evenly spaced points (usually 30). This is done by first calculating the total length of the ROI by summing the distances between successive pairs of ROI points. The total perimeter length is then divided by the desired number of interpolated ROI points. The first interpolated ROI point is one interpolation distance from the first point of the original ROI, the second point two distances, and so on.

2.3.2 Meshing

1. The first pair of ROIs are selected. Take the first point of the first outline and find the closest point on the second outline. This becomes the first edge of the first triangle.

2. Re-order the points on the second outline so that the closest point found in step 1 becomes the first point.

3. Take the point on the second outline found in step 2 and find the closest point on the first outline. These two points then form the second edge of the first triangle. The third edge is formed by joining the first and third points (figure 2.3). This process is repeated until either of the penultimate points of the two outlines are found.

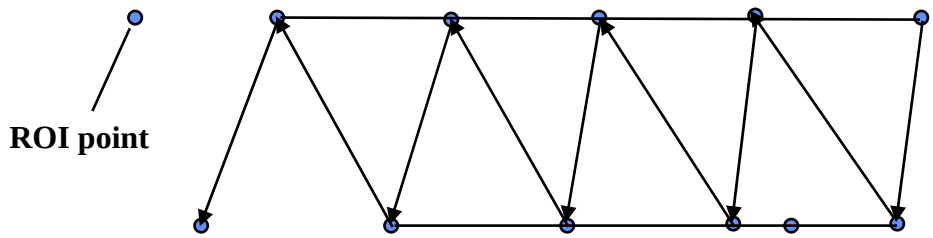

Figure 2.3 Closest neighbour triangulation.

4. The ends of the object are closed by calculating the centroid of the first and last outlines and joining the centroids with successive pairs of ROI points (figure 2.4).

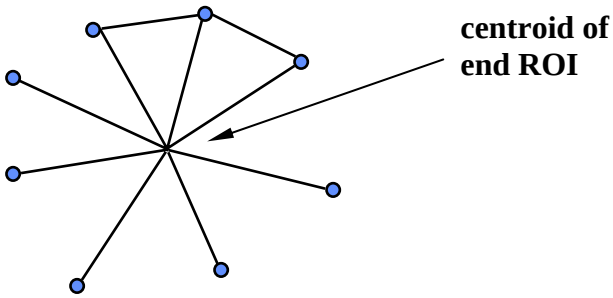

Figure 2.4 End ROIs are closed by connecting each ROI point with the ROI centroid.

2.4 Volume algorithms

Six volume algorithms were implemented for this project. Three of the algorithms (ellipsoid, planimetry and slice tetrahedral) appear in the literature in some form or other, although they were modified for the purposes of this project. The other three methods (centroid tetrahedral, Gauss and ray tracing) to the best of the authors knowledge have not been previously reported in the literature.

2.4.1 Ellipsoid

The ellipsoid volume is estimated by calculating the distance between the centroids of the first and last ROIs, and taking this distance as the long axis (c) of the object (figure 2.5). This technique is really only a simulation of the conventional method of specifically acquiring long axis and short axis views. However, the technique presented here should be a fair representation of the usual method.

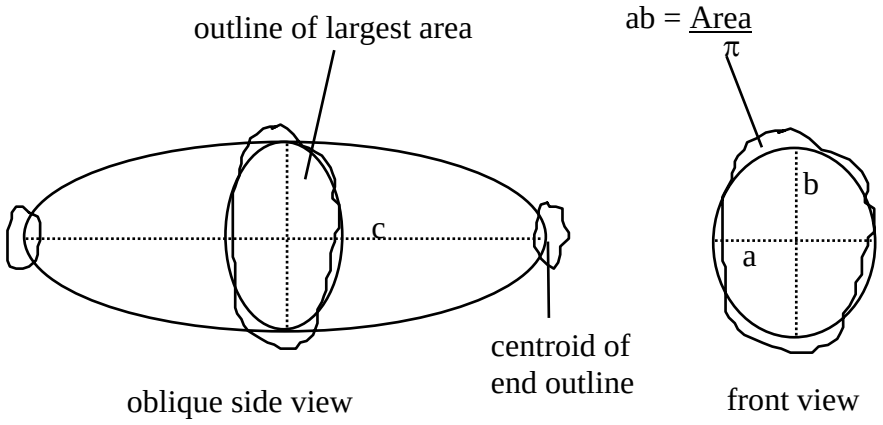

Figure 2.5 **Schematic diagram of ellipsoid method.**

The product of the two minor axes (ab) are calculated by finding the outline of maximum area and using the equation for the area (A) of an ellipse:

$$A = \pi ab \qquad (2.9)$$

where a and b are the semi-major and semi-minor axes respectively of the ellipse. Therefore, the product of the semi-axes (ab) can be calculated from

$$ab = \frac{A}{\pi} \tag{2.10}$$

The volume (V) of an ellipsoid is:

$$V = \frac{4}{3}\pi abc \tag{2.11}$$

where c is the semi-major axis of the ellipsoid.

2.4.2 Planimetry

This method involves multiplying the area of each slice by the local thickness. This technique is similar to the way in which the volume is calculated from parallel images, except a correction is applied to take into account non-orthogonality of the ROIs. For each pair of outlines, the local half-thickness of each slice is calculated by taking the vector product of the image normal and half the centroid-centroid vector (figure 2.6).

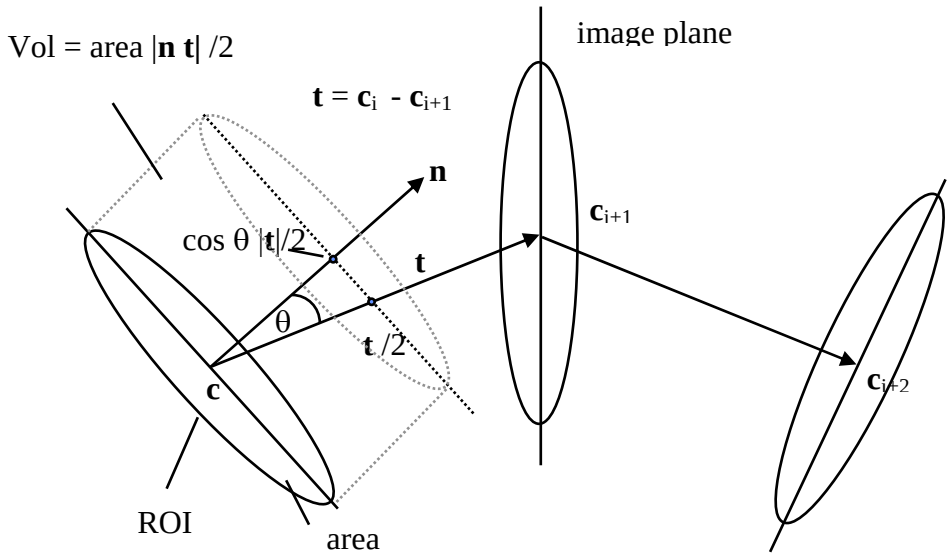

Figure 2.6 Schematic diagram of planimetry method.

$$V = \sum_{i=0}^{N-1} \left[a_i \mathbf{n}_i \frac{\mathbf{t}_{i,i+1}}{2} + a_{i+1} \mathbf{n}_{i+1} \frac{\mathbf{t}_{i,i+1}}{2} \right] \tag{2.12}$$

where,

a = slice area

n = image normal

t = centroid to centroid vector ($\mathbf{c}_i - \mathbf{c}_{i+1}$)

The scalar product of **n** and **t** in 2.12 is evaluated by multiplying the distance between adjacent centroids by the cosine of the angle between the two vectors.

$$\cos\theta = \frac{(\Delta x_1 \Delta x_2 + \Delta y_1 \Delta y_2 + \Delta z_1 \Delta z_2)}{|\mathbf{n}||\mathbf{t}|} \tag{2.13}$$

$$\Delta x_1 = c_{x,i} - c_{x,i+1} \tag{2.14}$$

$$\Delta x_2 = n_{x,i} - n_{x,i+1} \tag{2.15}$$

where $c_{x,i}$ is the x component of the ith centroid and $n_{x,i}$ the x direction cosine of the ith image normal, the expressions for y and z are similar to equations 2.14 and 2.15. $|\mathbf{n}|$ is the magnitude of the image normal (by definition unity) and $|\mathbf{t}|$ is the magnitude of the centroid to centroid vector, in other the words the distance between adjacent centroids. The product of local slice thickness and area becomes:

$$a_i \mathbf{n}_i \frac{\mathbf{t}_{i,i+1}}{2} = a_i(\Delta x_1 \Delta x_2 + \Delta y_1 \Delta y_2 + \Delta z_1 \Delta z_2)\frac{1}{2} \tag{2.16}$$

This algorithm was derived intuitively by the author, however, it is equivalent to that derived analytically by Watanabe (1982).

The area (a) and centroids (c_x, c_y) of each outline are calculated from

(2.17)

$$a = \left| \sum_{i=0}^{N-1} (x_i - x_{i+1})(y_i + y_{i+1})\frac{1}{2} \right|$$

(2.18)

$$c_x = \sum_{i=0}^{N-1} \left[\begin{array}{l} (x_i + x_{i+1})(x_i y_{i+1} - x_{i+1} y_i)\frac{1}{2} \\ +(y_i - y_{i+1})(x_i^2 + x_i x_{i+1} + x_{i+1}^2)\frac{1}{3} \end{array} \right] \frac{1}{a}$$

(2.19)

$$c_y = \sum_{i=0}^{N-1} \left[\begin{array}{l} (y_i + y_{i+1})(y_i x_{i+1} - y_{i+1} x_i)\frac{1}{2} \\ +(x_i - x_{i+1})(y_i^2 + y_i y_{i+1} + y_{i+1}^2)\frac{1}{3} \end{array} \right] \frac{1}{a}$$

The centroids are transformed to Fastrak coordinates using the transformation algorithm described in the image registration section (2.2.3).

The above algorithms work with ROIs in the xy plane. However, for multiplanar images the ROIs need to be rotated into the xy plane. This may be done by applying a rotation transformation (Ammeraal, 1986) so that the image normal projecting from the ROI centroid is aligned parallel to the z axis of the reference coordinate system.

2.4.3 Tetrahedral

This involves decomposing an object into tetrahedra. The volume of each tetrahedron is found by expressing three of the edge vectors that radiate from a single point (figure 2.7) as a three by three matrix. The volume of a parallelepiped with the edge vectors shown is given by the absolute value of the scalar triple product (2.20) (Kreyszig, 1993).

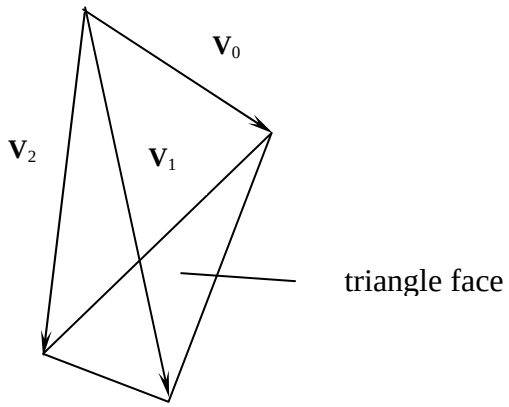

Figure 2.7 Tetrahedron.

$$Vol = (\mathbf{v}_0 \quad \mathbf{v}_1 \quad \mathbf{v}_2) = \left|\mathbf{v}_0 \bullet (\mathbf{v}_1 \times \mathbf{v}_2)\right| = \begin{vmatrix} v_{0,x} & v_{0,y} & v_{0,z} \\ v_{1,x} & v_{1,y} & v_{1,z} \\ v_{2,x} & v_{2,y} & v_{2,z} \end{vmatrix} \tag{2.20}$$

The volume of the parallelepiped is found by evaluating the determinant on the right hand side of equation 2.20. The volume of a tetrahedron is simply one sixth of the volume of the parallelepiped formed by the edge vectors. Two different methods of calculating volume using the tetrahedral method are described below.

2.4.3.1 Centroid-tetrahedral algorithm

1. Calculate the centroid of the organ (by dividing the sum of the x coordinates for the whole organ by the total number of vertices and the same for the y and z coordinates). The centroid does not have to be exact - just somewhere within the ROIs that ensures a clear line-of-sight between the centroid and each triangle vertex.

2. For each triangle, construct vectors between each vertex and organ centroid and calculate the volume of the resulting tetrahedron as described above.

If the shape of the object is such that tetrahedral edge vectors cut through the surface, the object can be subdivided into two or more sections.

2.4.3.2 Slice-tetrahedral algorithm

1. Designate each pair of outlines as a band, i.e. designate the first two outlines as, band one, the second and third outlines outlines as band two and so on.

2. Sort through the triangle list and assign triangles to a band. For instance, if a triangle has vertices belonging to outlines four and five, the triangle is assigned to band four.

3. Calculate the centroid of each outline.

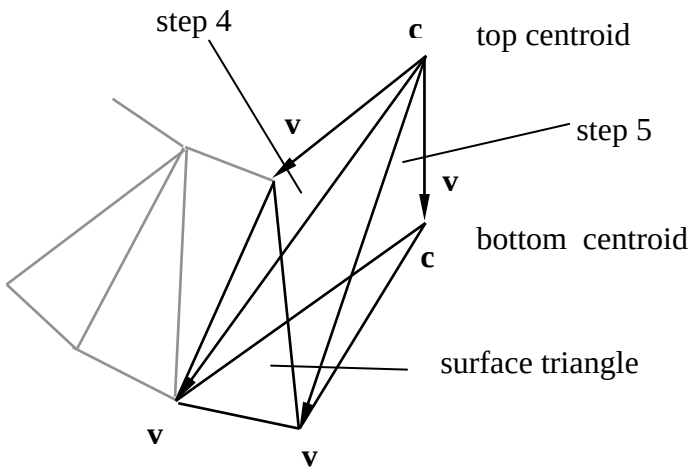

Figure 2.8 Schematic diagram of the slice tetrahedral method.

4. For each band, take the top centroid and project vectors (**v**) to each triangle vertex (figure 2.8). To calculate the volume of each tetrahedron, calculate the absolute value of the scalar triple product of the vectors and divide by six.

5. For each band, construct vectors between the top and bottom centroids (**c**), and between the bottom centroid and each pair of vertices around the bottom, and calculate the volume of each tetrahedron as in step 4.

2.4.4 Divergence theorem

In mathematical form, Gauss' theorem is stated as (Feynman, 1964):

$$\int_S \mathbf{C}.\mathbf{n} \quad da = \int_V \nabla.\mathbf{C} \quad dv \tag{2.21}$$

where **C** is a vector field, **n** the normal component of the differential surface area, *da*, and *dv* the differential volume. (In physics, the field might be a magnetic or electric field). The theorem can be adapted to estimate volume as follows.

Equation 2.21 expands to

$$\int_S \mathbf{C}.\mathbf{n} \quad da = \int \left(\frac{dC}{dx} \quad + \quad \frac{dC}{dy} \quad + \quad \frac{dC}{dz} \right) \Delta x \quad \Delta y \quad \Delta z \tag{2.22}$$

C, the vector field can be arbitrarily set to the sum of scaled spatial coordinates, i.e.:

$$\mathbf{C} = k_x.\mathbf{x} + k_y.\mathbf{y} + k_z.\mathbf{z} \tag{2.23}$$

where x,y, and z are the coordinates of a surface point multiplied by the unit vectors **i, j, k**, and k_x, k_y and k_z are scaling factors applied in the x,y, and z directions respectively. When equation 2.3 is differentiated, the divergence of **C** becomes:

$$\nabla.\mathbf{C} = k_x + k_y + k_z \tag{2.24}$$

therefore

$$\int_S \mathbf{C}.\mathbf{n}da = \left(k_x + k_y + k_z\right)V \tag{2.25}$$

If it is arranged that $k_x + k_y + k_z$ is = 1, and equation 2.23 is substituted into 2.25, then

$$\int_S \mathbf{C}.\mathbf{n}da = \int_S \left[\left(k_x n_x z\right) + \left(k_y n_y y\right) + \left(k_z n_z z\right)\right]da = V \tag{2.26}$$

In discrete form:

$$V = k_x \sum_i x_i n_x \Delta y \Delta z \quad + \quad k_y \sum_i y_i n_y \Delta x \Delta z \quad + \quad k_z \sum_i z_i n_z \Delta x \Delta y \tag{2.27}$$

where x_i is the x coordinate of the i^{th} voxel, n_x the x normal component at the position of the i^{th} voxel and $\Delta y \Delta z$ is the area of the voxel face in the yz plane. If the voxels are cubic then the products $\Delta y \Delta z$, $\Delta x \Delta z$ and $\Delta x \Delta y$ can be replaced by Δa, the constant area of each voxel face. Each of the three summations produces an estimate of the volume which can be weighted to reflect the orientation of the object with respect to the x,y and z axes. For instance (if the voxels are all the same size), k_x can be made equal to the number voxels with maximum unit normal components in the x direction expressed as a fraction of the total number of normals; k_y, k_z are calculated in a similar fashion for the y and z axes (Lancaster *et al* 1992).

The above algorithm, sometimes known as the divergence theorem algorithm (DTA) can be applied to surfaces described by a list of points with normals projecting from the centre of regular voxels (rectangular prisms) (Lancaster *et al* 1992 and Alyassin *et al* 1994). The DTA was can adapted by the author for use on a triangle mesh as follows:

$$V = k_x \sum_i c_{xi} a_i n_x \quad + \quad k_y \sum_i c_{yi} a_i n_y \quad + \quad k_z \sum_i c_{zi} a_i n_z \qquad (2.28)$$

where, in the case of the first summation, c_{xi} is the x coordinate of the centroid of the i^{th} triangle, n_{xi} the x normal component of the same triangle, and a_i the triangle area (figure 2.9(a)). The algorithm has been named (by the author) as the CAN (centroid-area-normal) algorithm to make it easy to remember. The algorithm was proved numerically by decomposing a triangular 'pillar' beneath a triangle into three tetrahedra (figure 2.9(b)).

(a)

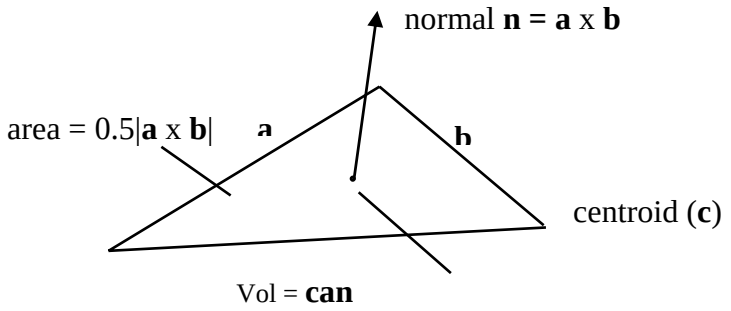

(b)

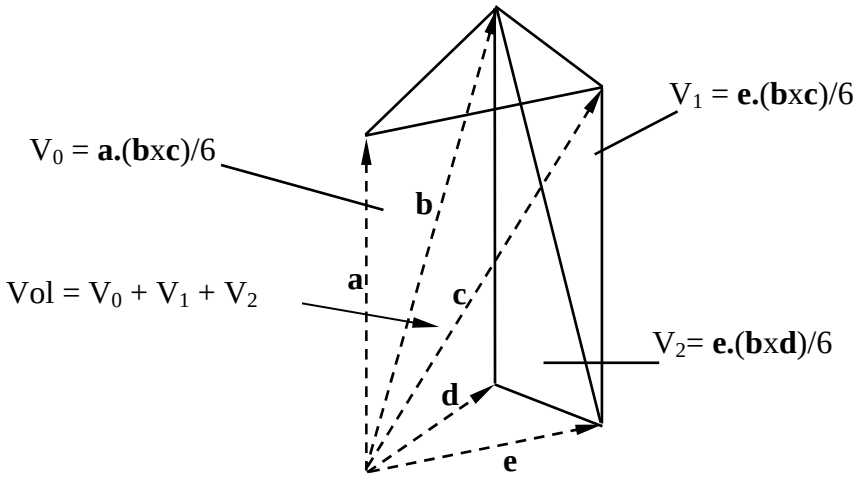

Figure 2.9 (a) Schematic diagram of the CAN algorithm. (b) Decomposition of a triangular prism into three tetrahedra.

The volume of the object could of course be calculated as shown in figure 2.9(b), but this would not be as computationally efficient as the CAN method. Another problem is that normals would have to be processed in some way to indicate whether a volume element was to be added or subtracted.

The centroid, area and normal of a triangle can be calculated fairly easily. The x coordinate of the centroid of a triangle is found by dividing the sum of the x coordinates by three. The y and z components are found in a similar fashion. The triangle normal (**n**) is found by calculating the cross-product of any two of the edge vectors (**a, b**), i.e. **n = a** x **b**. Surface extraction algorithms normally arrange the order of the vertices so that the cross-product (i.e. normal) points either out of or into the surface to ensure proper shading. The area of a 3D triangle is simply half the magnitude of the cross-product, i.e. a = 0.5 |**a** x **b**| (equivalent to half the base length times the height for a 2D triangle).

The calculation of the triangle normals and areas can be combined for improved computational efficiency. As before, the components of k can be used to weight the volume according to the orientation of the object with respect to the axes. The weights k_x, k_y, k_z can be obtained by calculating the area of the object projecting onto the yz, xz and xy planes respectively. This may be done by summing the products of the normal components and triangle areas for each axis (in effect equation 2.28 with the centroid coordinates removed).

The operation of the CAN algorithm can be understood intuitively as follows. Imagine an object suspended above the x,y ground plane (z = 0) with all triangle normals projecting outward from the surface. The volume between each upward facing triangle and the ground plane is the product of the z component of the normal, triangle area, and height (i.e. z coordinate) of the centroid. The triangle can be imagined to be on top of a triangularly shaped column. Summing for each triangle we obtain the total volume underneath the top surface of the object.

The triangles on the bottom surface will have normals pointing down to the x,y plane, therefore the z components of these normals will be negative, resulting in negative volume elements. When summed, these elements represent the total volume underneath

the object. Adding the total volume underneath the top surface to the total (negative) volume underneath the bottom surface gives the total volume of the object. The same argument applies for the xz and yz planes. It does not matter if the triangles are different in size as the area of any closed surface facing in the positive direction of an axis is always equal to that facing in the negative direction, no matter how complicated or contorted the shape of the object.

The accuracy of the algorithm will depend on how well the surface of the object has been tessellated with triangles. Triangles must not overlap and all normals must project from high to low density or *vice versa*. (If approximately half of the normals were to project from low to high density and half from high to low the volume would come out close to zero). If normals point from high to low density (i.e. outward looking) the total volume will be positive; if the normals are inward looking the total volume will be negative.

Holes on the surface, which might be gaps between the edges of adjacent triangles or missing triangles, will also lead to errors. The effect of surface holes can be minimised by translating the centroid of the object onto the origin of the coordinate system so that the normals and triangle areas remain exactly the same but the centroids are reduced in magnitude. The error in the result will be directly proportional to the distance of the object centroid from the origin. For example, when a test object (one of the kidneys used in the experiments described in chapter 6) was translated 500 mm in the x,y and z directions away from the origin, the CAN volume increased by 1.6%.

If the direction of the normals is consistent (i.e. either all high-to-low, or low-to-high,) the algorithm will correctly calculate the volume of a closed surface encompassing smaller closed surfaces (i.e. internal holes). Internal holes will produce a volume opposite in sign to the main outer surface, and so the total volume of the object can be found by adding the volume of the holes to the outer volume. However, high density regions within an enclosed surface will result in over-estimation of the total volume as the volume of the hole will be added to the total volume instead of subtracted. One way round this problem is to change the sign of the components of either the inner or outer set of normals.

2.4.5 Ray tracing algorithm

Ray tracing algorithms (RTAs) are commonly used in 3D graphics packages, for example in the production of photo-realistic renderings of objects.

The object or objects are assumed to be in the form of a triangle mesh, i.e. a list of vertices and an array of integer triplets indicating how the vertices are to be connected into triangles. The mesh or meshes need not be enclosed, for example, the volume or mean distance between two sheets might be required. Each ray is modelled as a 3D vector, i.e. a point in space (position vector) and a direction described by the x,y and z direction cosines of the vector

2.4.5.1 Generic algorithm

The RTA is divided up into the following basic steps.

1. Calculate the plane equation of each triangle: ax + by + cz = h, where h is a constant and a,b and c are the respective x,y and z components of the triangle normal. The plane equation of a triangle is found by taking the cross (vector) product of any two edge vectors (**a**,**b)** i.e. **n** = **a** x **b**, where **n** is the normal to the plane. The equation of a plane can be found by multiplying the normal (**n**) by the position vector (**p**) of any point on the plane, in this case any of the triangle vertices, i.e.:

$$\mathbf{np} = h \qquad (2.29)$$

where
n = [a b c], the plane normal
p = [x y z], a point on the plane
h = a constant

(N.B. the location of a point in space can be considered to be a position vector as the point is x,y,z unit vectors (**i**,**j**,**k**) from the origin).

2. Calculate the intercept between each ray and each triangle using the triangle plane and ray vector equations (figure 2.10). Any point (**p**) on the ray is given by the position vector

of a reference point on the ray (**r**) plus the direction cosines of the ray vector (**v**) multiplied by a factor (*t*), i.e **p** = **r** + *t***v**. *t* can be thought of as the number of unit vectors between the end of the ray and a designated point on the ray. The intercept between a line and a plane is found by substituting the equation of the ray into the plane equation (2.31):

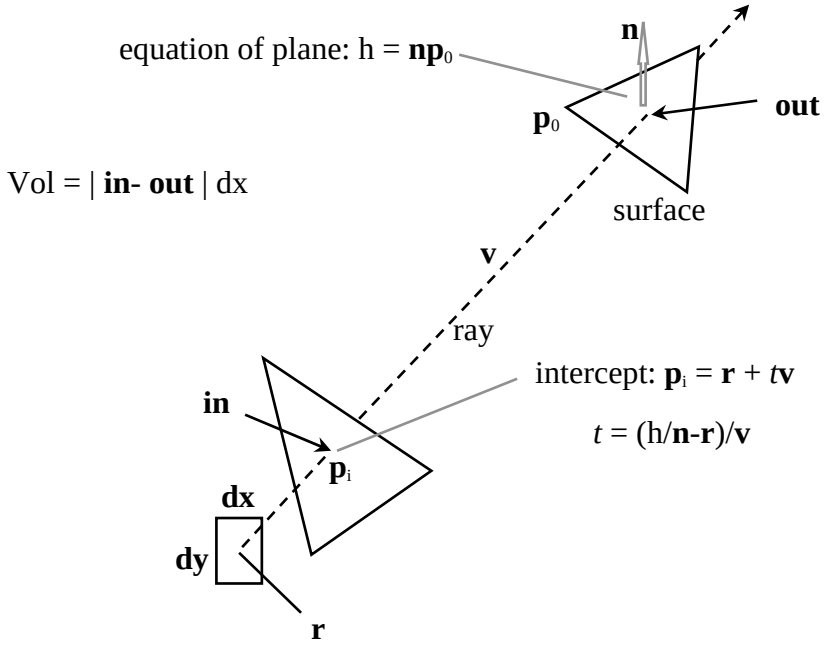

Figure 2.10 Schematic diagram of RTA.

$$\mathbf{n(r} + t\mathbf{v)} = \mathrm{h} \tag{2.30}$$

$$\therefore\ t = \left(\frac{\mathrm{h} - \mathbf{nr}}{\mathbf{nv}}\right) \tag{2.31}$$

$$\mathbf{p}_i = \mathbf{r} + t\mathbf{v} \tag{2.32}$$

where **nr** is the sum of the products of the normal components of the plane and the corresponding coordinates (i.e. ax + by + cz) of a reference point on the ray (e.g. one end of the ray), **nv** is the sum of products of the normal components of the plane and the direction cosines of the ray (i.e. $av_x + bv_x + cv_z$), *t* is substituted into the line equation to calculate the x,y and z coordinates of the intercept point (2.32).

3. Check to see if the intercept point lies within the bounds of the triangle. This is done by constructing vectors between the intercept and each vertex of the test triangle. Calculate the angle between successive pairs of triangle vectors, i.e. $\mathbf{v}_0,\mathbf{v}_1$; $\mathbf{v}_1,\mathbf{v}_2$; $\mathbf{v}_2,\mathbf{v}_0$ and add the three angles together (figure 2.11 (a), (b)). (The cosine of the angle between two vectors is equal to the sum of the direction cosine products, i.e. $\cos\theta = ll' + mm' + nn'$ where l,m and n and l',m' and n' are the direction cosines in the x, y and z directions for the two vectors respectively). If the intercept point lies within the triangle, or on any edge, the three angles will add up to exactly 360^0 (by definition as there are 360^0 in a circle). For any intercept point lying outside the triangle the sum of the angles will be less than180^0. For points coincident with any of the vertices, two of the angles will be 90^0 and the total angle less than 360^0. Triangles with planes parallel to the rays should be pre-excluded as there can be no intercept in this case.

(a)

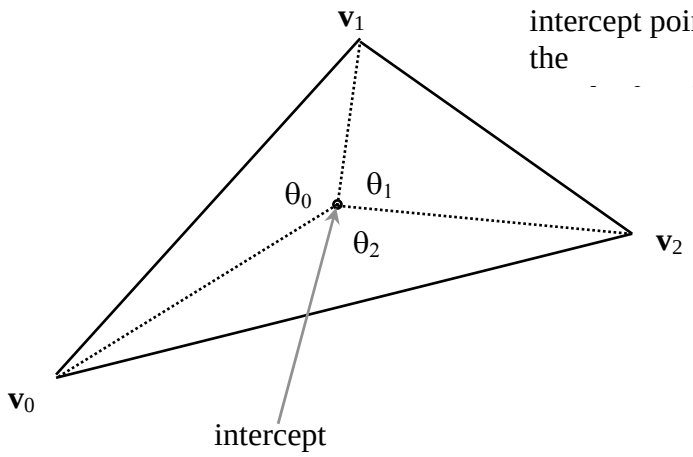

(b)

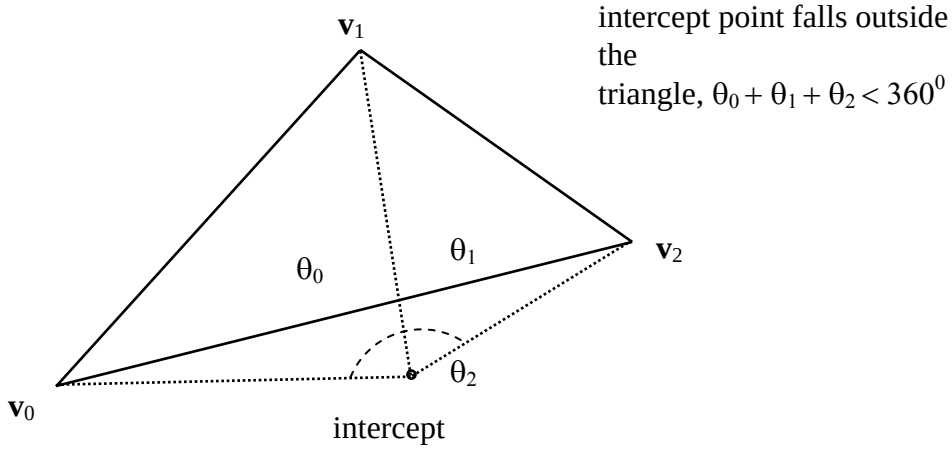

Figure 2.11 (a) Internal triangle intercept. (b) External.

4. All of the triangles in an enclosed mesh have edges and vertices in common with adjacent triangles. If a ray intercepts a shared edge or vertex, two or more intercept points will be produced. As only one intercept point is required at each interface all duplicates should be removed.

2.4.5.2 Optimisation

It is generally well known that ray tracing algorithms tend to be very slow because of the enormous number of calculations required. However, the RTA can be optimized resulting in a significant reduction in computing time by pre-assigning triangles to search vectors. For any particular ray only a very small fraction of the total number of triangles in the mesh need be checked for interception. This can be done by checking to see if the x,y coordinates of the vertices of a triangle fall within a certain range of the x,y coordinate of a ray (assuming that the rays are to be cast in the z direction). All the selected triangles fall within the walls of an imaginary shaft passing through the object. For each ray, only those triangles within the shaft need to be checked for interception. Each triangles is assigned to a shaft, or search vectors, using the following algorithm:

$$
\begin{aligned}
x_i &= (x - \text{min\_x})/dx \\
y_i &= (y - \text{min\_y})/dy \\
\text{vector}(x_i, y_i, \text{tri\_count}(x_i,y_i)) &= \text{current\_tri\_no} \\
\text{tri\_count}(x_i,y_i) &= \text{tri\_count}(x_i,y_i) + 1
\end{aligned}
\tag{2.32}
$$

where x_i and y_i are integers indicating the array indices of the search vector that a triangle has been assigned to, dx and dy are the x,y dimensions of the shaft, and x and y are the (floating point) coordinates of the vertex currently being assigned to a search vector, min_x and min_y are the minimum x and y coordinates of the object which define the origin of the grid. This algorithm uses the fact that in most computer languages floating point values are rounded down to the nearest integer when asigned to an integer variable. For example, if the grid extends 100 units in the x direction and has 10 divisions in the x direction, a vertex with an x value of 77 will be assigned to vector 7 (77/10 = 7.7, integer of 7.7 = 7).

One problem with this technique is that if the x,y dimensions of the shaft are smaller than the x,y dimensions of a triangle, the shaft may pass straight through the triangle without any of the vertices being assigned to the search vector. This problem can be overcome by ensuring that the grid resolution is such that no triangle can be missed. This is done by calculating the maximum x dimension of each triangle and finding the maximum value in the whole triangle list. This is repeated for the y and z dimensions. The maximum x dimension is divided into the x dimensions of the object (defined as the minimum x position subtracted from the maximum x position). This is repeated for the y and z directions.

Some extra modifications are required for this algorithm to work in all circumstances. In some cases triangles may be oriented diagonally across shaft boundaries such that their edges pass through one or two shafts without being assigned. This problem may be overcome by checking the indices of the shafts that a triangle has been assigned to. In figure 2.12 the dotted triangle has shaft 1,1 passing straight through it, therefore the grid resolution should be lower to ensure that triangles of this size can be assigned to a shaft. The solid triangle straddles four shafts although the triangle will only be assigned to the two shafts (0,0) and (1,1) that the vertices lie within. To avoid ‘misses’, the triangle must also be assigned to shafts (0,1) and (1,0).

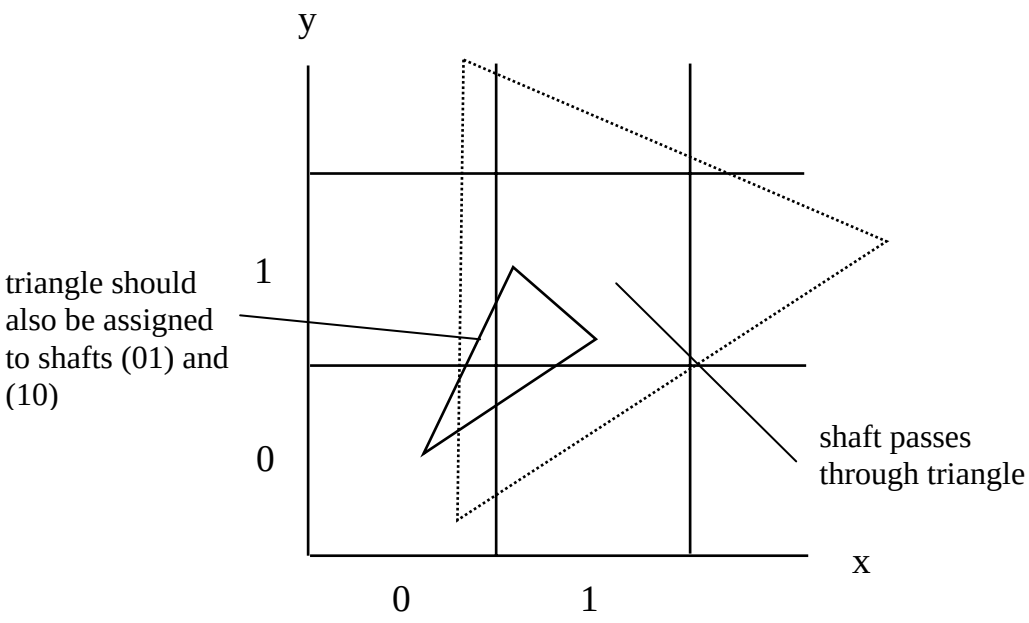

Figure 2.12 Triangles in relation to search vector shafts.

This can be effected by checking the x and y indices of the shafts. If either the x or y indices of the two shafts are different filler triangles are required to completely enclose the triangle. In the example depicted in figure 2.12, the x indices, (0 and 1), and y indices (0 and 1) are different. The extra shafts can be found by swapping the y coordinates i.e. 0,1 and 1,0.

As an example to demonstrate the improvement in speed, if an object has 30 rays along the x axis and 30 rays along the y axis (rays are cast in the z direction) and there are more or less the same number of triangles in each search vector, on average, there will be a factor of 900 (30 x 30) fewer triangles to be searched for each ray.

The assignment of triangles to search vectors only has a small overhead compared with the section of the algorithm dealing with finding intercepts as only one pass through the triangles is required. Further speed enhancements can be obtained by pre-excluding triangles parallel to the direction of the rays as no intercept is possible. The speed of the RTA can be further improved by checking to see if a ray passes through a triangle before calculating the intercept point. This can be done by passing the x,y coordinate of the ray and triangle vertices into the routine described in step 3 of the generic RTA.

2.4.5.3 Volume version of the RTA

The generic RTA can be tailored to calculate the volume enclosed by a triangle mesh. This involves casting a rectilinear grid of parallel rays through the object and calculating the intercepts (figure 2.13). In this case, the RTA works on the basis of what goes in must come out (assuming that the object is completely enclosed by a triangle mesh). The volume of each element is given by the product of the distance between intercept points and the x and y separation of the rays. It is easy to see that the greater the number of rays the greater the accuracy of the volume estimate. The RTA can also calculate the volume of multiple objects within the tracing field. Assuming an enclosed triangle mesh, the algorithm will always work whatever the shape of the object, and objects can also have any number of internal holes of any shape. This could be especially useful in cases where a dividing cubes algorithm has produced a single vertex and triangle list describing

multiple objects. The RTA can be used to calculate the total volume of a group of objects without having to segment individual objects which would have to be done before the tetrahedral or planimetry methods could be used. (N.B. algorithms based on Gauss' theorem are also able to calculate the volume of multiple objects). The volume of each ray is given as the product of the distance between intercepts and the cross sectional area of the ray.

For volume calculations, the RTA can be simplified by collapsing all of the object triangles onto the x,y plane at z=0 by making their z coordinates equal to zero. Each ray is then given as an x,y coordinate rather than a 3D vector. The number of triangles intercepted by each ray are counted.

1. Construct a grid in the x,y plane with dimensions equal to the maximum x and y extent of the object(s).

2. Choose the number of grid points in the x and y direction (this will affect the accuracy of the result). The separation of the grid in the x and y directions can be specified as a certain size, in which case the number of grid points in the x and y direction will depend on the x and y dimensions of the object. Complicated shapes may need more rays than simpler shapes for comparable accuracy.

3. Check to see if the x,y coordinate of each grid point falls within the boundary of a triangle as described above.

4. When the whole object has been ray traced, sort the z values of the ray-triangle intercepts into ascending order. The ray-volume is calculated by multiplying the ray area by the lengths of successive intercept pairs. In most cases there will only be one pair of intercept points, however, an odd number of intercepts will arise if there are gaps in the mesh. If an object contains internal chambers, then the volume of the ‘solid’ object may be found from the product of the grid area and the distance between the first and second, the third and fourth intercept points etc. The volume of the internal holes may be found from the second and third, the fourth and fifth intercepts etc. (figure 2.3).

In general, more accurate results are obtained using the same number of rays if the aspect of the object with the largest area is facing in the direction of the rays. If necessary, a transformation (Ammeraal, 1986) can be applied to the object to rotate it with respect to the direction of the rays. In some cases it will not matter if there are holes in the surface if they are parallel to the direction of the rays, for example at the top and bottom of an object. The volume of overlap of two or more objects can also be calculated by summing the volume of concomitant rays. By applying an appropriate rotation transformation to the object, rays can be cast parallel to the major axes of the object to calculate the mean height, width and depth. The volume of an object can be calculated in sections by integrating the ray volumes for each plane.

A problem can arise if the object has concave indentations. In this case rays can pass outside of the surface and be interpreted as internal holes. This problem can be overcome by projecting rays in the x,y and z direction from the mid-point of each internal ray. If an internal ray is bounded by intercepts in the x,y and directions then the ray is truly internal. However, if the ray is not surrounded by intercepts then it is in fact an external ray. (N.B. This problem did not arise with any of the ultrasound volumes as they were convex in shape with no concave regions. However, the algorithm that has been developed can handle such situations if necessary).

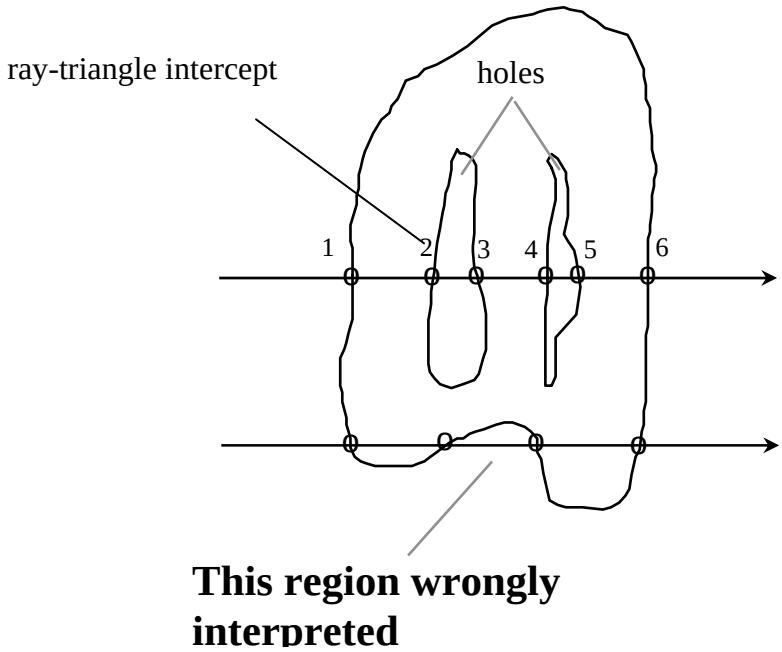

Figure 2.13 Rays cast through an object containing holes.

The ability of the RTA to determine whether or not a ray is internal or external can be used to segment internal triangles prior to use of the CAN algorithm. With an object containing a mixture of external and internal triangles there is no easy way of determining which is which. If all triangles are included in the CAN volume calculation an invalid volume will be produced. In this case rays are projected from each triangle centroid in the x,y and z directions. Internal triangles will be bounded by intercepts in the x,y and z directions.

2.6 Summary

This chapter has described an algorithm for transforming image points into 3D localiser space. Although specific to this project, the algorithm developed is generic and could be therefore be adapted for any other localiser system. A triangulation algorithm has also been developed, although it is limited in that it cannot handle bifurcations of ROIs. Six volume algorithms have also been developed that can be applied to multiplanar ROIs. Three have been described in the literature, and three were developed by the author. It is a good engineering principle to have a number of different volume algorithms. If markedly different values are produced by the algorithms, then this is likely to indicate a problem.

CHAPTER 3

Theoretical and experimental validation of the volume algorithms

3.1 Introduction

This chapter describes the theoretical and experimental work carried out to test the algorithms described in the last chapter. The chapter is divided broadly into two sections. The first section describes the use of computer generated geometric objects to validate the algorithms. The second section describes the use of X-ray CT to experimentally validate the algorithms specially developed for this project (centroid-tetrahedral, CAN and RTA). The reason for using CT was to validate the new algorithms with triangle meshes generated from real image data rather than computer generated data.

3.2 Theoretical validation of the volume algorithms

A computer program was written in C to generate spheres, cones, cylinders and prolate (cigar shaped) and oblate (saucer shaped) ellipsoids. Details of the objects are provided in table 3.1. The user can specify the magnitude of the major axes of the object, the number of cros-sectional slices, and number of points in each ROI. For testing the volume algorithms objects were created with 20 cross-sectional slices and 30 points in each ROI (600 points for each object). These values were chosen for similarity to the ultrasound reconstructions. The ROI points were connected into a triangle mesh using the nearest-neighbour algorithm described in chapter 2. Figure 3.1 shows a sphere generated using the object generator program. The sphere has been rendered with alternating light and dark triangles so that the edges of the triangles are easier to see. In this case normals have been shown projecting from the triangle centroids.

The RTA was tested on the objects detailed in table 3.1, with a grid resolution varying between 5 and 50; (i.e. in the case of the sphere the grid separation varied between 1/5 and 1/50 of the sphere diameter). Figure 3.2 shows the variation in the percentage error with grid resolution. In all cases the error is below 1% for grid resolutions of 15 x 15 or greater. Note that the error is smaller at a lower grid resolution for the cylinder and cone

suggesting that higher resolutions are required for more complex objects to achieve the same error. The prolate and oblate ellipsoid plots are very similar to that of the sphere and so have been excluded from figure 3.2 in the interests of clarity.

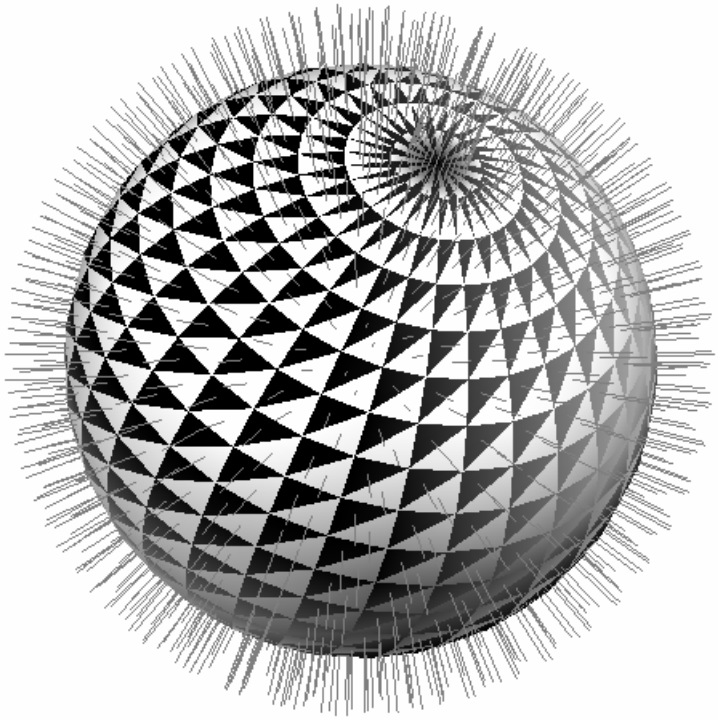

Figure 3.1 A computer generated sphere showing normals projecting from triangle centroids.

The model generation code was also used to investigate the relation between the accuracy of calculating volume and the number of slices acquired through an object number of ROI points. This work is described in chapter 7 which deals with errors.

Table 3.1 Theoretical comparison between the CAN, slice-tetrahedral and planimetry methods of calculating volume for computer generated objects. (r = radius or semi-axes, h = height, in arbitrary units). Each object had 20 ROIs and 30 ROI points, except for the high resolution ellipsoid which had 50 ROIs and 90 ROI points.

generated object	axes (r,h)	actual volume	CAN	tetrahedral	planimetry
sphere	5	523.59	516.50	516.50	517.53
cylinder	2.5, 10	196.35	185.17	185.17	185.17
prolate ellipsoid	5,2,1	41.89	41.22	41.30	41.40
oblate ellipsoid	5,4,1	83.77	81.20	82.38	82.80
cone	2.5,10	65.45	64.96	64.96	65.04
high res. ellipsoid	5,2,1	41.89	41.79	41.81	41.83

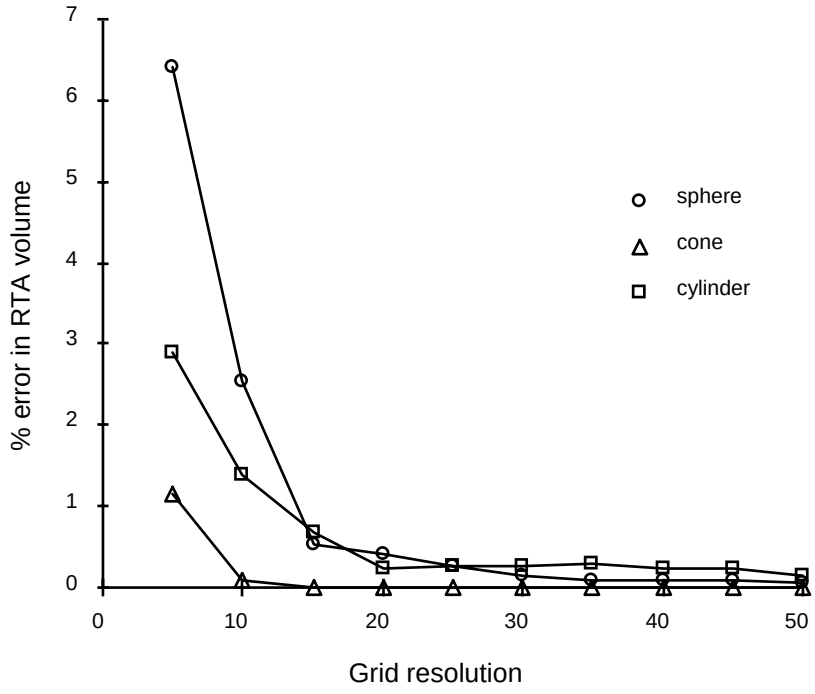

Figure 3.2 Relation between the number of grid points and percentage error in calculating volume.

3.3 Experimental validation of the volume algorithms

3.3.1 Introduction

The last section showed that the algorithms work very well on computer generated test objects, but what about real life data? The CAN and RTA algorithms were validated experimentally by applying them to surfaces extracted from CT scans of irregularly shaped objects. CT is currently the most accurate imaging modality. The manufacturer of the CT scanner used for these experiments (Siemens) claim a table position accuracy of ±1 mm in 300mm (0.3%). A test carried out by the author using a Perspex phantom, ascertained that pixel dimensions were accurate < 1%. CT scanning also enabled the CAN and RTA to be compared with volumes generated by voxel counting - a technique commonly used in CT and MR. The CAN and RTA algorithms were also compared with the centroid-tetrahedral method.

This section of the chapter has been divided into two parts to separately address the CAN and RTA algorithms. Firstly the CAN algorithm is validated against the conventional method of voxel counting and the centroid-tetrahedral algorithm, and secondly the RTA is compared with the CAN algorithm and the other methods. The ability of the CAN and RTA algorithms to cope with internal enclosed surfaces (i.e. holes) is explored. Although this is not strictly of relevance to this particular project, it could be important in the future if and when automatic surface extraction algorithms are developed capable of reliable segmentation of ultrasound image data.

In this chapter (and in the rest of the thesis), scatter plots and Bland-Altman plots have been used to assess the agreement between measuring volume by the various methods and a ‘gold standard’ (e.g. water displacement). Many workers have assessed the accuracy of their volume estimation techniques by calculating the correlation coefficient. However, Bland-Altman (1986) have shown that the correlation coefficient is inappropriate for assessing the agreement between two independent methods of measuring a quantity. Bland and Altman cite the measurement of skin-fold thickness using calipers as an example. Caliper measurements are twice the skin-fold thickness, although a correlation coefficient very close to unity is obtained. In this case the measurements are very highly correlated but are not in good agreement.

A Bland-Altman plot is generated by plotting the difference between the experimental measurement and the 'gold standard' against the mean of the two measurements. The mean of all the differences is then plotted with 'error bars' at ± 2 standard deviations 95% of the differences will be expected to fall within ± 2 SDs of the mean.

3.3.2 Experimenetal validation of the CAN algorithm

3.3.2.1 Method

Ten rocks (4 - 105 ml) hand moulded from air-hardening modelling clay (of similar X-ray density to bone) were scanned on a CT scanner (Siemens Somaton DRH, Erlangen, Germany). The rocks were left to harden for at least 24 hours before scanning. Images had a matrix size of 512 x 512, a pixel size of 0.5 mm^2 and a slice thickness and separation of 2 mm. To minimise partial volume effects, the rocks were placed on blocks of polystyrene foam. The image data was stored on half-inch magnetic tape and transferred on a Titan graphics super-computer supercomputer (Kubota Pacific Inc, Santa Clara, CA, USA). A dividing cubes algorithm (Cline et al 1985) was used to render the surface as a triangle mesh (Figure 3.3).

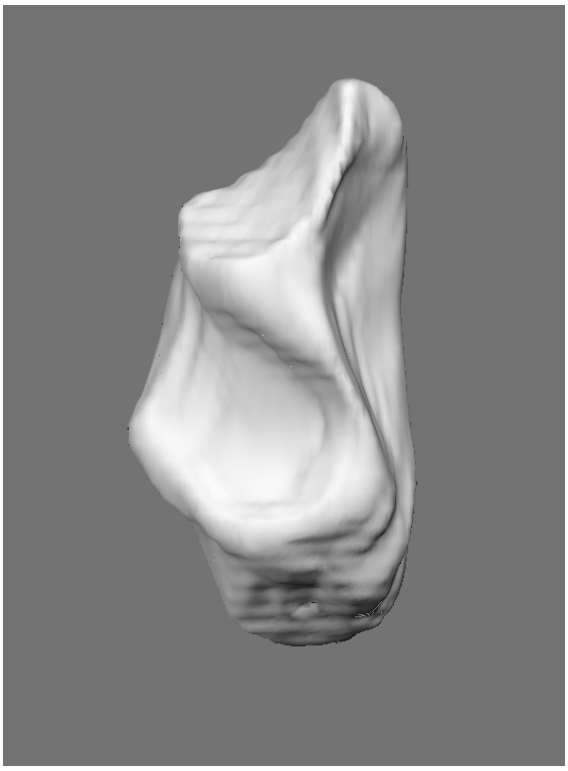

Figure 3.3 Surface rendering of a rock made from modelling clay.

The C computer code for this algorithm was acquired by the author from a member of Kubota (although at the time it was called Ardent Computer). A threshold value midway between the mean background value and mean object value was chosen as suggested by Kennedy et al. (1989). The actual volume of the rocks was measured by water displacement. The volume of each rock was also estimated by multiplying the number of voxels above the threshold value by the volume of each voxel, in this case 2 x 0.5 x 0.5 = 0.5 mm^3.

On scanning, it was discovered that the rocks contained small inner holes of irregular shape. This presented a good opportunity to test the CAN algorithm on complicated shapes containing irregularly shaped internal holes.

The total volume of the rocks would be difficult to calculate using planimetry or tetrahedral decomposition as the internal holes would have to be treated as separate objects. A problem with the CAN algorithm is that triangles belonging to internal surfaces must be filtered out in some way if only the volume enclosed by the outer surface is required. In this case, the holes were removed by drawing ROIs around the holes on the relevant images and filling the ROIs with pixels of greater value than the chosen threshold so that only the outer surface was extracted. The voxel count (VOX) and CAN volumes were calculated for the rocks with and without the holes. The volumes of the holes were calculated by subtracting the CAN and VOX hole and no-hole volumes respectively. The volumes of the rocks were also calculated using the centroid-tetrahedral algorithm.

3.3.2.2 Results

Figure 3.4 (a) shows a scatter plot of CAN volume versus VOX volume, with and without the inclusion of holes, and figure 3.4 (b) shows a Bland-Altman plot of the same data. The difference between the CAN and VOX no-hole volumes increases with volume with a correlation coefficient (r) of 0.979, although the maximum difference is less that 0.6 ml. When holes are included in the CAN and VOX volume calculations, there is only a slight increase in the CAN - VOX difference with volume (r = 0.693). Figure 3.5 (a) shows a scatter plot of CAN hole volume versus VOX hole volume and figure 3.5 (b) shows a Bland-Altman plot of the same data.

(a)

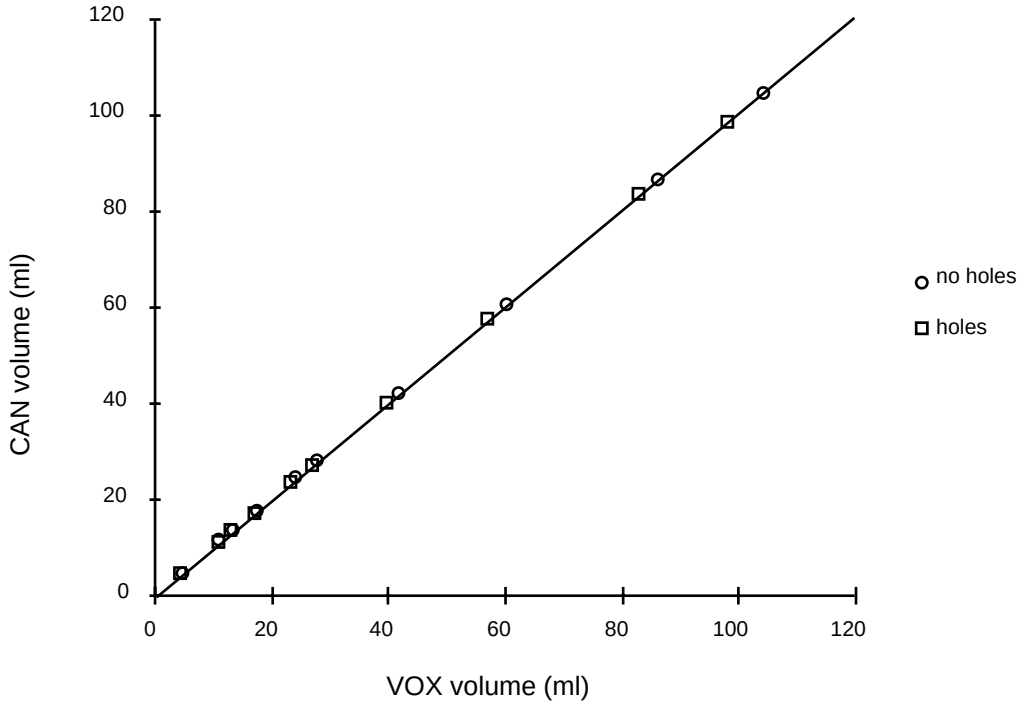

(b)

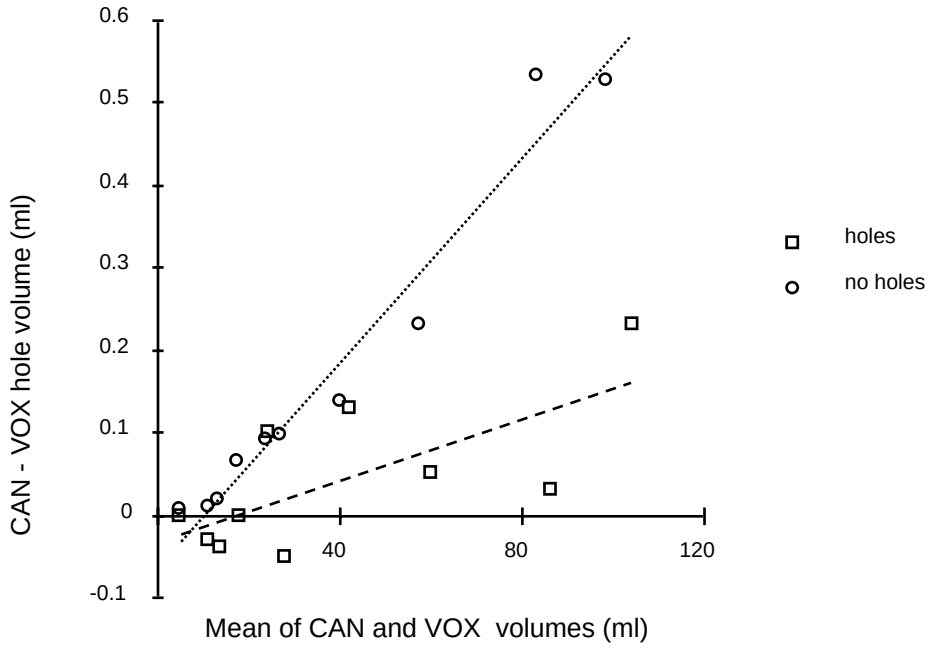

Figure 3.4 (a) A plot of CAN versus VOX volumes for rocks with and without the inclusion of internal holes. The line of identity is shown. (b) Bland-Altman plot of the same data.

(a)

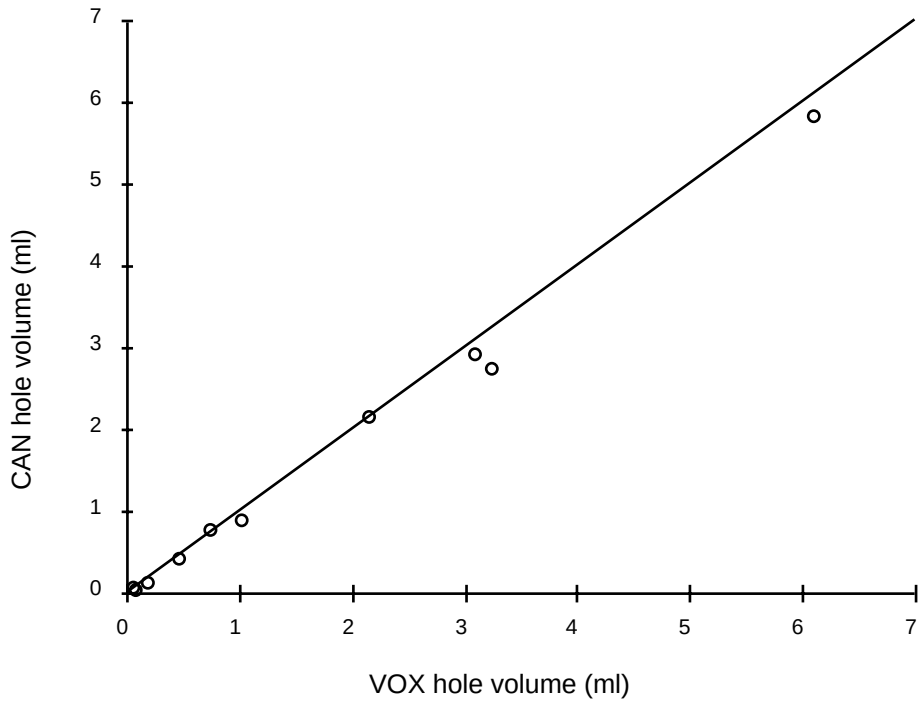

(b)

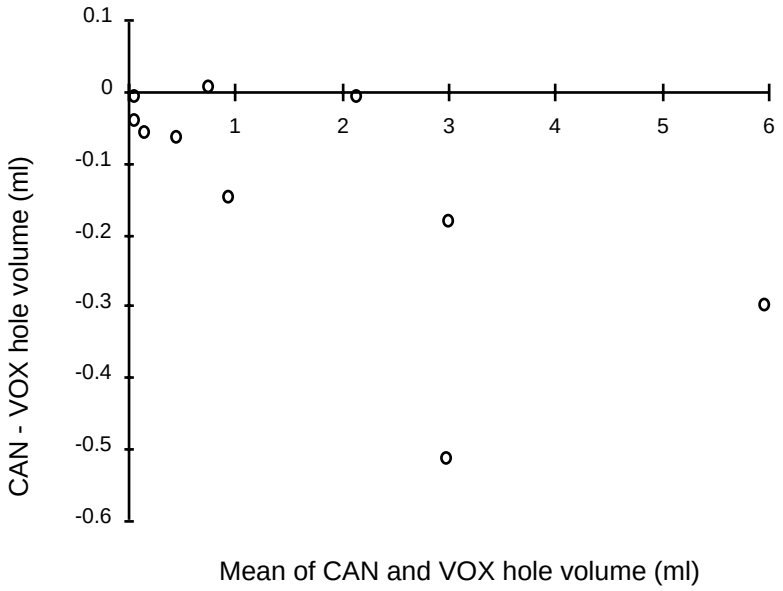

Figure 3.5 (a) CAN versus VOX hole volume showing the line of identity. (b) Bland-Altman plot of the same data.

Table 3.2 Comparison of volume algorithms expressed as the mean ± one standard deviation of the absolute and percentage error.

Algorithm	Voxel counting	Tetrahedral	CAN	RTA
absolute error	0.03 ± 0.85	0.3 ± 1.0	0.07 ± 0.89	0.00 ± 0.85
% error	-1.2 ± 3.1	-0.7 ± 3.2	-1.2 ± 3.2	-1.4 ± 3.2

3.3.2.3 Discussion

The results show that there is very close agreement between the CAN and VOX volumes, and the CAN algorithm is comparable in accuracy to the tetrahedral algorithm. The maximum discrepancy between the two methods is about 0.5 ml at 100 ml which corresponds to an error of just 0.5%. Bland and Altman (1995) demonstrate how an increase in the difference with volume can be due to either a difference in the variance or difference in the accuracy of the two methods being compared. In this case the variances are almost identical, therefore the difference must be due to differing accuracy.

On reflection, this is probably due to the partial volume effect causing under-estimation of the VOX volume. This arises because the true surface of an object normally falls inside a voxel, resulting in the value of the edge voxel being 'diluted' by material of lower density next to the edge (in this case air). Consequently edge voxels tend to fall below the threshold value and so are not included in the volume.

However, the partial volume effect has the opposite effect on holes, causing them to appear larger. In this experiment, the CAN volumes would be expected to be more accurate as the surface triangles are generated by a marching cubes algorithm. The marching cubes algorithm calculates the position of surface triangles by linearly interpolating between adjacent voxels, therefore triangles generated by this method will be closer to the true surface than the rectangular voxel faces.

The tendency of the partial volume effect to over-estimate hole volume probably explains why there is much less of an increase in the difference between the CAN and VOX algorithms with the volume enclosed by the outer surface (figure 3.4(b)). In this case, the under-estimation in the volume enclosed by the outer surface is partially cancelled by the over-estimation of the hole volumes. A slight over-estimation of VOX hole volume compared to the CAN volume is seen in figure 3.5, although for practical purposes the difference is unlikely to be important.

The CAN algorithm is easy to implement, executes relatively quickly, and requires only a small amount of computer code. The main advantage of the CAN algorithm is that it can be used on objects of any shape and takes into account internal holes, assuming the normals point in the right direction. It should be stressed that the planimetry and tetrahedral algorithms are capable of the same accuracy as the CAN method, but may not be as convenient to use. For instance, objects with internal holes and surface protuberances may need to be cut into smaller sections before the planimetry or tetrahedral algorithms can be used.

The CAN algorithm is general purpose and is appropriate for use with automatically generated surfaces as well as those constructed from manually drawn ROIs. The overall accuracy of the algorithm will of course also depend on other issues such as the number of slices through the object and the number of points in each ROI (chapter 7). The CAN algorithm could of course be applied to objects as diverse as molecular models, architectural models, atmospheric clouds, subterranean oil reservoirs, etc.

3.3.3 Experimenetal validation of the RTA

3.3.3.1 Method

The same rocks were used to verify the RTA. A grid resolution of 20 in the x direction and 60 in the y direction was chosen to approximately reflect the aspect ratio of the rocks. The rocks were rotated so that their long axes were aligned with the y axis using standard transformations (Ammeraal, 1989).

3.3.3.2 Results

Figure 3.6(a) shows a scatter plot of rock RTA volume versus CAN volume, and figure 3.6(b) shows a Bland-Altman plot of the same data. Figure 3.6(b) is particularly interesting as it shows that there is a slight increase in the difference between the RTA and CAN volumes with increasing volume.

(a)

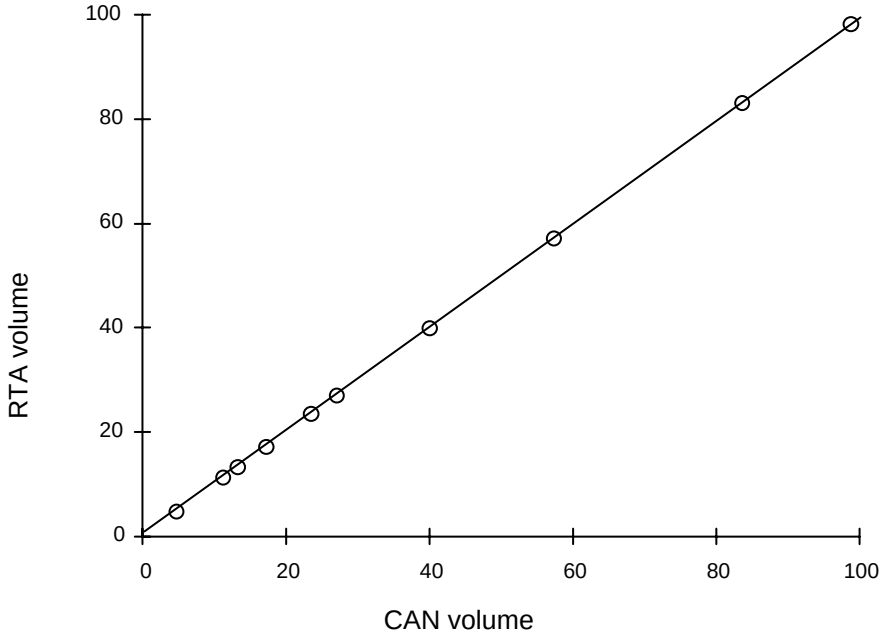

(b)

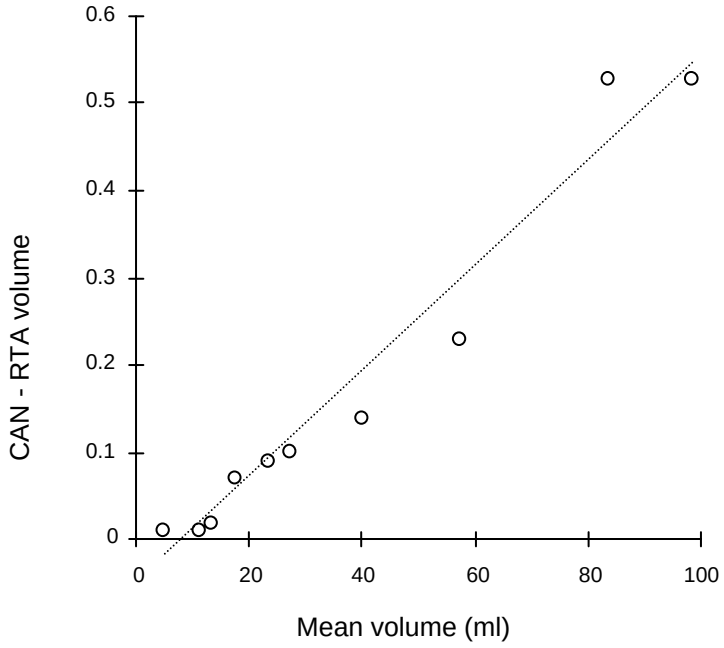

Figure 3.6 (a) Rock RTA versus CAN volume. (b) Bland-Altman plot of the same data.

(a)

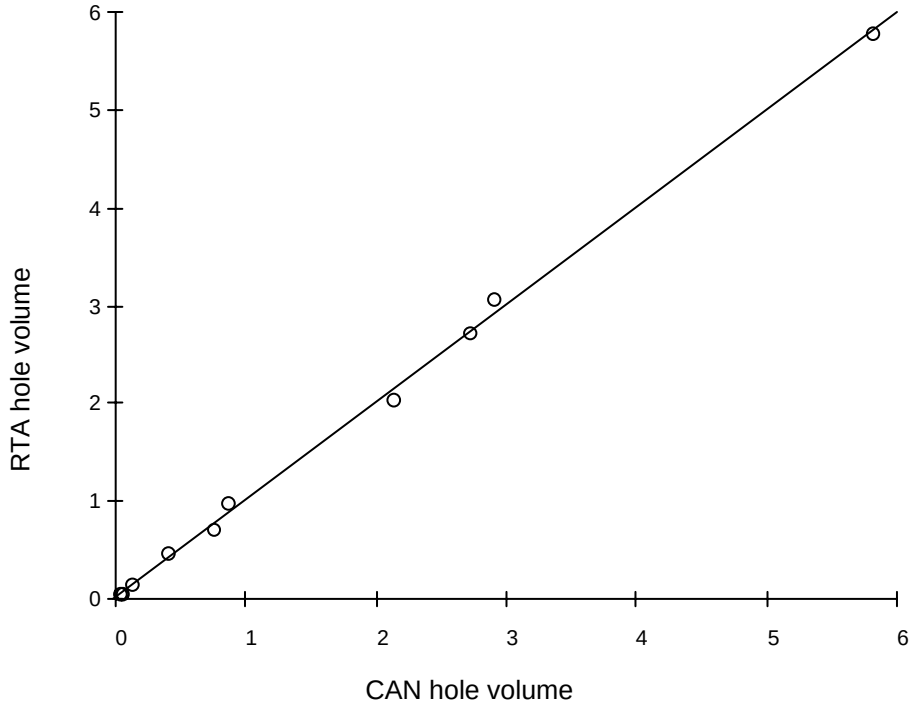

(b)

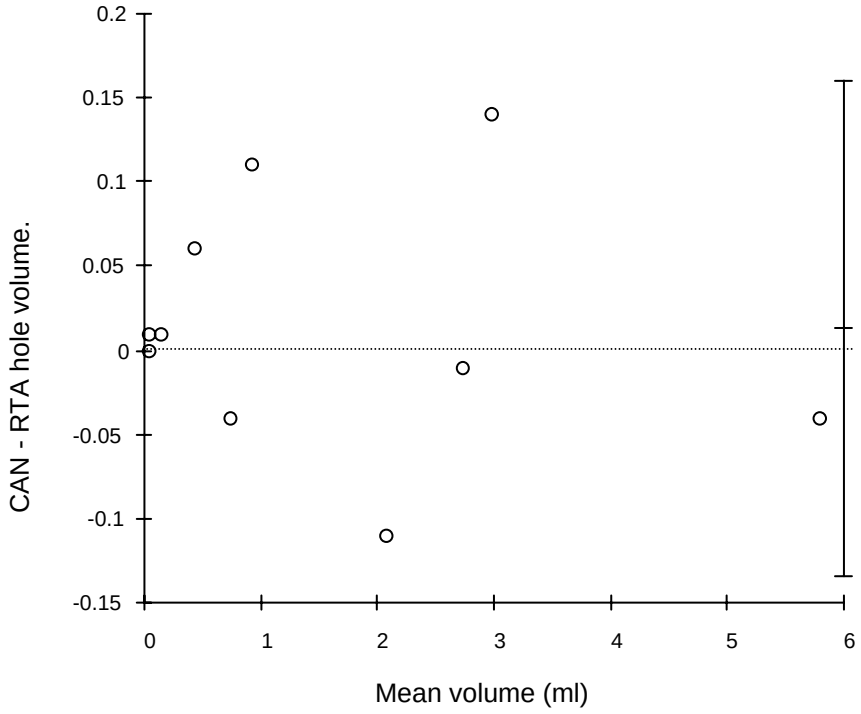

Figure 3.7 (a) RTA rock hole volume versus CAN hole volume. (b) Bland-Altman plot of the same data.

This plot is very similar to that obtained for CAN and voxel count volume shown above. This is probably because the mesh is effectively being ‘voxelized’ by the RTA. Figure 3.7(a) shows a scatter plot of RTA hole volume versus CAN hole volume, and a Bland-Altman plot in figure 3.7(b)

3.3.3.3 Discussion

The results show that the accuracy and precision of the RTA is comparable to other methods used for calculating volume. The RTA is particularly useful for calculating the volume of both solid and cavity volumes. This could be done with any of the other volume algorithms discussed in this thesis but with a lot more difficulty. The RTA could also be useful for calculating the volume of a structure in sections. This could of course be done by other methods, for example, by cutting a mesh into parallel sections and using the CAN algorithm on each section. However this would involve a substantial amount of extra computer code.

The main attraction of the RTA is that no pre-processing of the data is required. Unlike the CAN and tetrahedral methods, the RTA can be used with meshes with overlapping triangles. This could be useful in cases where an organ has been US scanned from multiple directions resulting in multiple sets of ROIs. The meshes could be combined and only the outer RTA intercepts used in the volume calculation. Another method could be to generate a grid appropriate to all the meshes and use the RTA on each individual mesh. A kind of exclusive OR would be applied to the combined set of rays so that only one section of ray can exist at any one point along the path. Calculating the total volume of overlapping meshes would probably be difficult to do by other means. This technique could possibly be useful for assessing the degree of movement of an organ or structure.

CHAPTER 4

Hardware and Software

4.1 Introduction

This chapter describes the hardware and software components of the system.

4.2 Hardware

4.2.1 Video capture

The main components of the system are shown in the photograph in figure 4.1 and schematically in figure 4.2. The system comprises an IBM compatible personal computer (PC) (ProData 486, Data Products and Services, Inc. Loveland, CO, USA, distributed in the UK by ODT Europe Ltd, London). The PC has 8 Mbytes of random access memory (RAM) and a 200 Mbyte hard disc. Images are captured using a Win/TV video capture card (Hauppauge Computer Works, Inc., Hauppauge, NY, USA, distributed in the UK by ODT Europe Ltd, London) placed in one of the expansion slots of the PC.

The video capture board intercepts video signals en route to the (VGA) monitor, enabling video images to be displayed in an operating system window (Windows 3.11, Microsoft Corporation, Redmond, WA). The Win/TV card can be configured to accept all of the main television broadcast standards (e.g. NTSC and PAL). In this case the card was configured in PAL mode which is the video standard for TV transmission in the UK, including the video output of ultrasound scanners.

Video images are captured into a 1 Mbyte on-board frame buffer in various sizes and can be stored on the hard disc in a variety of standard image formats. For this system the Microsoft Windows Device Independent Bitmap (BMP) format was chosen as this enables captured images to be viewed with any standard graphics software package (for example Microsoft Paint which comes bundled with Windows 3.11).

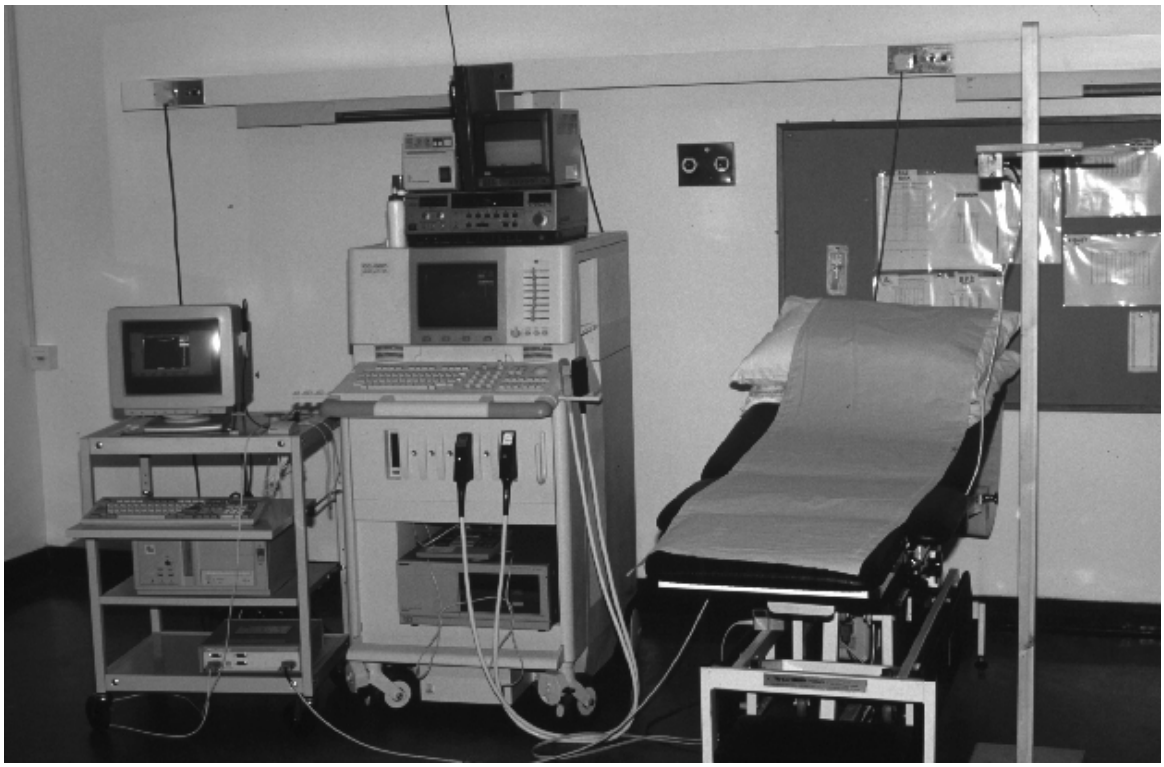

Figure 4.1 Equipment on the fetal medicine unit at Guy's Hospital. The Fastrak systems electronic unit is seen on the bottom shelf of the computer trolley to the left of the Acuson 128XP/10 scanner . The Fastrak transmitter is attached to the wooden stand to the right of the couch.

Video images are captured with a precision of 7 bits, resulting in 128 grey levels. However, these grey levels are within the range 0-255 in steps of 2 simulating an 8 bit image. Speed of acquisition, format conversion and storage onto hard disc are dependent on the image matrix size. For this system a 328 x 228 image matrix size was chosen as this approximates the 256 x 256 matrix size commonly used in medical imaging. This configuration resulted in an image capture and storage rate of two images per second.

Video images are initially captured in colour using the YUV colour broadcast standard (Foley et al, 1990), and are then converted into grey scale before saving onto disc in BMP format.

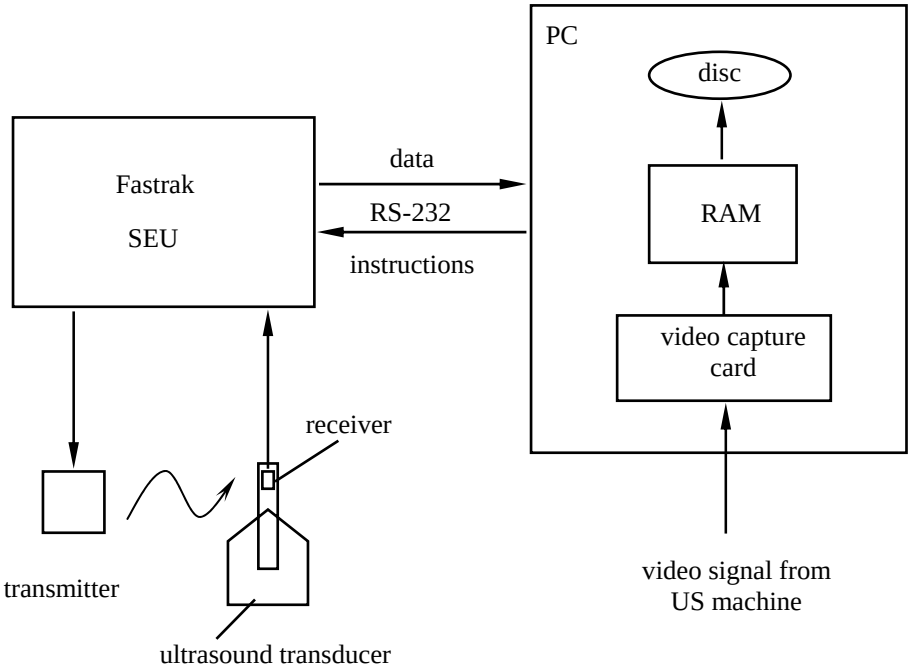

Figure 4.2 Schematic diagram of the equipment shown in figure 4.1.

4.2.2 3D tracking device

The position and orientation of the ultrasound transducer is measured using a Polhemus 3Space Fastrak system (Polhemus, Inc., Colchester, VT, USA, distributed in the UK by Virtual Presence Ltd, London). Figure 4.3 shows the Fastrak receiver attached to an Acuson 128XP/10 transducer. A schematic diagram is shown in figure 2.2. In this case $\mathbf{v}_1$ = 17.9 cm and $\mathbf{v}_2$ = 2.8 cm. (see the previous chapter for a schematic representation). The attachment comprises a plastic shell which clips onto the transducer. This shell was custom made from a mould cast from the transducer.

A Perspex bar was attached to the shell by means of a polythene screw. The shell was accurately machined (± 0.1 mm) to ensure that the line-of-sight axis of the receiver was parallel to the image plane and aligned with centre of the transducer face. The location of the electrical centre of the receiver and alignment of the axes was assumed to be as given in the manual – an assumption borne out by tests carried out on the Fastrak (described in the next chapter). A Perspex bar was used with the Acuson 128XP/10 as initial

experiments with an Acuson 128XP/3 ascertained that the transducer interfered with the position and orientation values (resulting in skewed ROIs).

The Fastrak system comprises a transmitter and receiver, both of which connect to a System Electronics Unit (SEU). The transmitter emits a 8013 Hz electromagnetic signal which is detected by the receiver. The SEU uses the detected signal to calculate the x,y, and z displacement and orientation of the receiver with respect to the coordinate system of the transmitter.

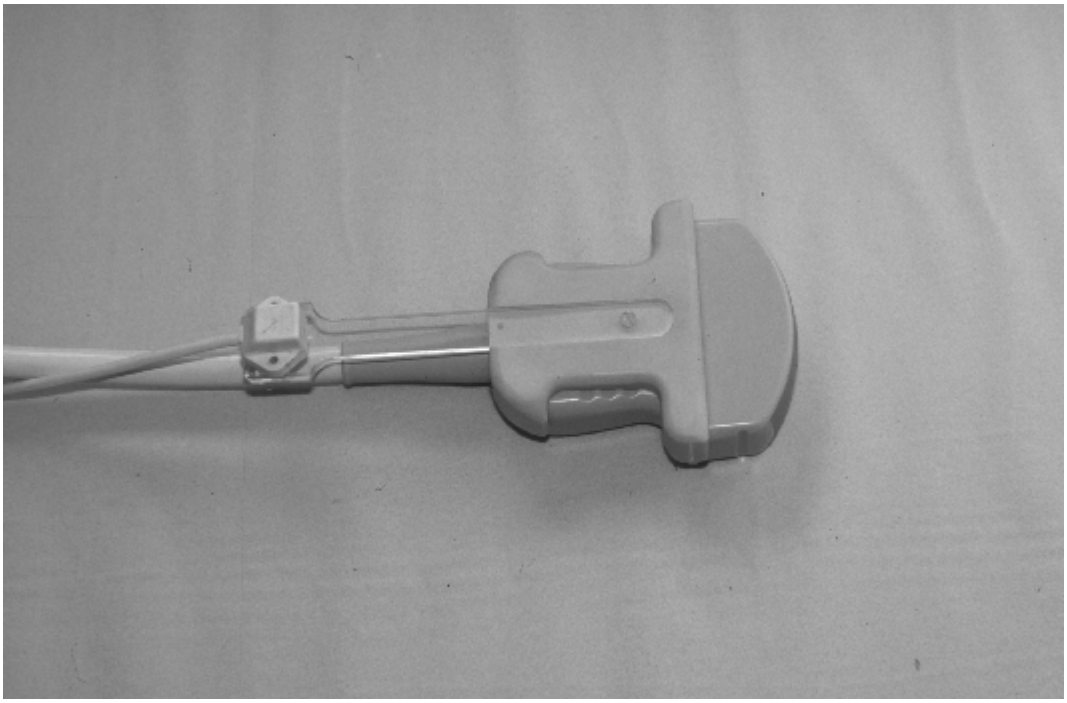

Figure 4.3 Polhemus sensor attached to the ultrasound transducer.

The system is commonly used in Virtual Reality (VR) applications where sensors are placed on a helmet to indicate the wearer's line-of-sight and on gloves to indicate the position of the hand. A 3D stylus is also available, which has been used, for example, in the field of archaeology to model jars etc. The Fastrak receiver is small (2.8 x 2.3 x 1.5 cm) and light (17 g) with a light weight cable enabling it to be fixed to an ultrasound transducer without disturbing normal scanning.

The SEU is connected to a PC either via the RS-232 serial interface or IEEE-488 parallel interface. Communication is quicker using the IEEE-488, but generally an extra PC

board is required. As virtually every PC comes with an RS-232 interface this interface was chosen. The maximum data transfer rate is 100 Kbytes/sec for the IEEE-488 and 14.9 Kbytes/sec (or 115200 baud (bits per second)) for the RS-232. The update rate is 120 readings per second with one receiver which reduces to 60, 40 and 20 per second for two, three and four receivers respectively. Due to PC BIOS restrictions (the Basic Input Output System of the PC) communication was limited to 9600 baud in this system.

Each of the transmitter coils are excited in turn with the same frequency and phase and the induced voltage measured in the three receiver coils. Hence nine voltage readings are obtained. The receiver coils are sufficiently small with respect to the transmitter coils to be considered point dipoles. The excitation of each loop antennae in the transmitter produces a far field component with 1/r dependence and a near, or induced field component with a $1/r^3$ dependence. The Fastrak makes use of the near field component. The voltage induced in each receiver coil is governed by equation 4.1.

$$\mathbf{V} = \frac{1}{r^3}\mathbf{SKM} \tag{4.1}$$

$$\mathbf{M} = \begin{bmatrix} \mathbf{m}_1 & \mathbf{m}_2 & \mathbf{m}_3 \end{bmatrix}$$

$$\mathbf{S} = \begin{bmatrix} \mathbf{s}_1 & \mathbf{s}_2 & \mathbf{s}_3 \end{bmatrix}$$

where **V** is a three by three matrix containing nine voltages. **M** contains the magnetic moments produced by each transmitter coil, and **S** contains the sensitivities of each receiver coil (i.e. the efficiency of converting the magnetic field into a voltage). K is a magnetic linkage factor (presumably some kind of calibration factor). This is the extent of the information given in the manual. Presumably the position and orientation of each receiver coil with respect to the transmitter coils is calculated from the relative strengths of the receiver voltages.

The Fastrak has two regions of operation separated by the yz plane at x = 0. The coordinate system is shown in figure 4.4. Note in particular that there are two positive x axes. Care needs to be taken to ensure that the receiver does not cross over from one hemisphere to another during a scan. (This situation could be corrected in software, but it creates an unnecessary difficulty).

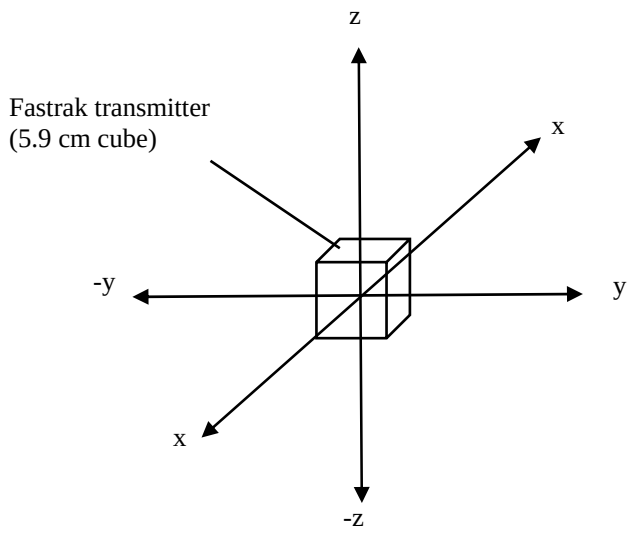

Figure 4.4 The transmitter coordinate system of the Fastrak localiser system.

4.3 Software

The software comprises two main programs, one PC based to capture image and position data, and the other UNIX based to draw ROIs and calculate volume. The PC capture program was developed in the 'C' programing language using the Microsoft Visual C++ programming environment.

Communication with the Fastrak SEU was programed using BIOS calls to the RS-232 serial port. The SEU is controlled by ASCII character sequences sent from the PC down the serial link. For example, an initiation sequence of characters ("cfuO1,52,61\r") is sent to the SEU instructing it to send back position and orientation data. In the string above, the 'c' instructs the unit to go into single shot mode – i.e. information is only sent back to the PC when requested. The 'f' indicates that binary mode is to be used as opposed to ASCII. (Transmitting data in binary format is more efficient than using ASCII as only 4 bytes are required to encode each floating point number). The 'u' instructs the SEU to use metric rather than imperial measure and the 'O1' indicates that the receiver is connected to input channel one. The '52' instructs the SEU to transmit the x,y, and z coordinates of

the receiver in extended precision mode and the ‘61’ similarly for the orientation quarternions. This results in seven binary numbers being transmitted every time an initiation character ‘P’ is sent from the PC to the SEU.

The latency period of the SEU is 4 ms, i.e. measurements are available 4 ms after reception of the ‘P’. The position and orientation data are sent back at 9600 baud, therefore 41 ms are required to transmit each sample. The position and orientation data are acquired immediately after each image acquisition.

The Win/TV card was programmed using a software development kit (SDK) provided by Hauppauge. This comprises a library of functions callable from a user-developed program. The capture program was developed to acquire images either in single shot mode or as a rapid sequence (e.g. 20 images in 10 seconds). In single shot mode, the user is prompted for the next frame, capture being initiated by a mouse click on an “OK” dialogue box. The user has the option of cancelling the sequence at any time in which case fewer images will be stored on disc. Single shot mode was used for capturing the kidney and liver images (described in the chapter on the *in vitro* organ experiments).

In fast capture mode, a set number (default 20) of images are captured and stored on disc. Fast capture mode was used to acquire the balloon images as described in section 6.2. After capture, the position coordinates and the orientation quarternions are displayed on the screen for checking by the user. Any problems are usually apparent, the coordinates should be less than 100 cm and the orientation quarternions always between 1.0 and –1.0. (If the serial link fails either zeros or nonsense values are produced).

Ultrasound images were transferred from the PC to a Titan UNIX graphics supercomputer (Kubota Pacific Inc, Santa Clara, CA, USA) via a local area network (LAN). A program was written in C and X11 (a windows extension to the UNIX operating system) to load and display the BMP ultrasound images and draw ROIs. Image calibration factors are obtained by measuring the pixel length of calibration scales on the images using a mouse. The centre of the transducer face is also marked using the mouse. The calibration data and information concerning the direction and magnitude of the receiver vectors are acquired beforehand and stored in a separate Position Information File (PIF) which is

recalled by the transformation function. The transformation function generates a 3 x 3 transformation matrix for each image plane (as described in chapter 2).

A 3D graphics library provided with the Titan computer called *Dore* (*D*ynamic *O*bject *R*endering *E*nvironment) was used to display a 3D representation of the mesh. This library contains functions that let the user specify the x,y,z coordinates of each ROI point and a list of integer triplets specifying how the points are to be connected to form a triangle mesh. For example, the triplet (3,4,7) indicates that vertices 3,4 and 7 are to be connected to form a triangle. Normals can be provided by the programmer, or calculated by the function from the cross-product of two triangle edges. The resulting surface is displayed with triangle normals projecting alternately into and out of the surface resulting in alternating light and dark triangular facets. This makes it easier to check that the meshing algorithm has performed correctly. The surface can be rotated, translated and scaled in the x,y and z directions.

CHAPTER 5

Fastrak accuracy in a clinical setting

5.1 Introduction

The Fastrak localiser is central to the system described in this thesis, therefore it is important to know how it performs in a clinical setting, as the accuracy will have an important bearing on the accuracy of measuring volume. The accuracy and resolution figures quoted by the manufacturer are for operation in a metal free environment, a situation which will only be approximated in the clinic. A number of tests were carried out to assess the effect of a metal framed scanning couch and ultrasound transducer etc. which are likely to be closest metallic items to the Fastrak transmitter and receiver.

In a metal free environment, the static accuracy is stated as being 0.8mm RMS (equivalent to standard deviation) for the receiver position and 0.15 ^{o} (2.618×10^{-3} radians) for orientation. The resolution (i.e. smallest detectable change) is given as 0.005 mm per mm of range and 0.025 ^{o} (2.181×10^{-4} radians) across the range. These values are obtainable when the receiver is within 76 cm of the transmitter in a metal free environment. The maximum range is given as 3.05 m.

All of the experiments described below were performed with an Acuson 128XP/10 scanner with a 5 MHz curvilinear probe, except for experiments 5.3 and 5.4 which were carried out with a Tosbee Ecocee.

5.2 Wheel test

5.2.1 Introduction

It would be very tedious to fully assess the accuracy of a device with six degrees of freedom such as the Fastrak. However, testing can be simplified by combining position and orientation measurements using a wheel.

5.2.2 Method

The Fastrak receiver was fixed onto a test wheel (figure 5.1) using polythene screws so that the electrical centre of the receiver (as specified in the Fastrak manual) was 10 cm (± 0.01 cm) from the centre of the wheel. The receiver was oriented so that the line-of-sight vector projected towards the centre of the wheel. The wheel was fixed to a plastic base that allowed 360^o rotation about the vertical axis. The whole assembly was fixed securely to a board using reusable plastic adhesive and placed on a metal framed treatment couch (as in figure 4.1).

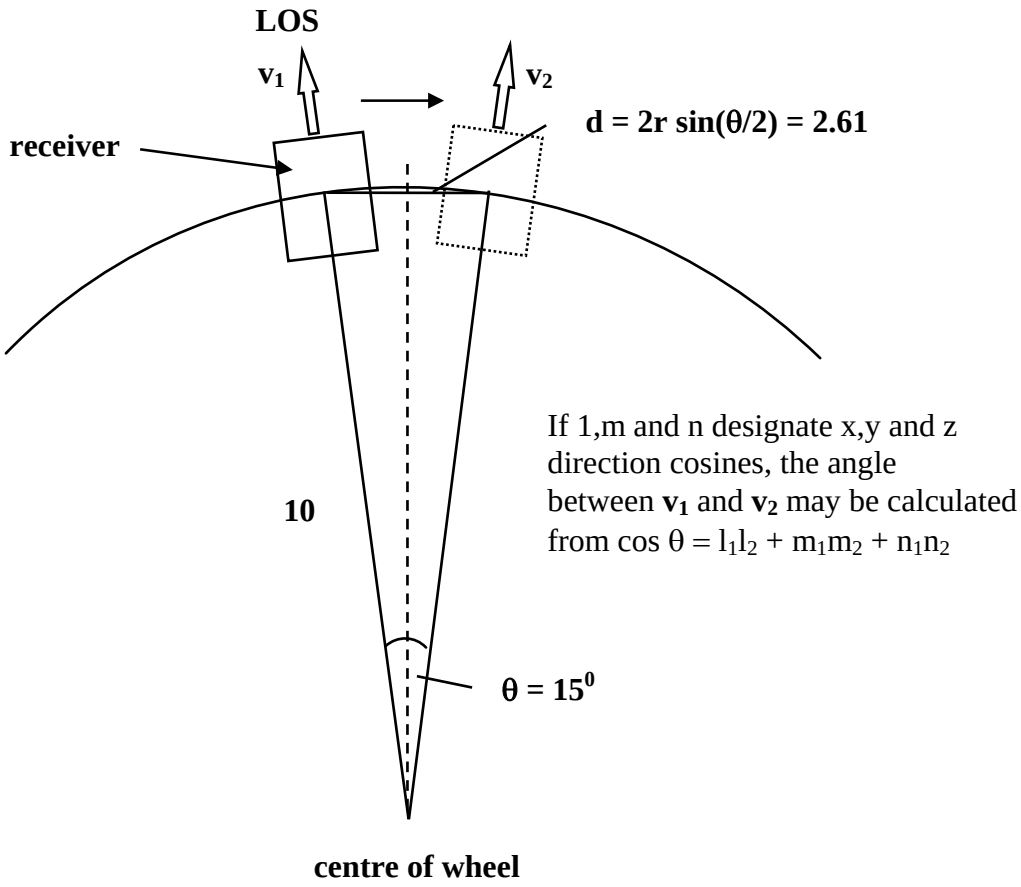

Figure 5.1 Schematic diagram of Perspex wheel used to test the Fastrak.

The centre of the wheel was 18 ± 0.5 cm above the top surface of the couch. Therefore the receiver ranged from 8 to 28 cm above the couch. In clinical use, for example in scanning a pregnant mother, the receiver would generally be greater than 30 cm above the

couch, although with some slim mothers in the early stages of pregnancy it might go lower. Therefore the range of movement represents a worst case scenario.

The wheel assembly was placed at two positions on the couch, one with the centre of the wheel at a mean distance of 43.8 cm (range 36.7 - 51.2 cm) from the transmitter and the other at a mean distance of 31.8 cm (range 22. - 40.8 cm). The wheel was oriented at about 45^{o} to the long axis of the couch with the receiver facing the transmitter. This was done to effect a more realistic orientation of the receiver in relation to the transmitter and to ensure that all the coils were 'exercised'. The transmitter was held above the wheel and beside the couch by a wooden post (as seen in figure 4.1).

The wheel was carefully rotated in 15^{o} increments and the position and orientation of the receiver recorded using a notebook PC connected to the Fastrak SEU via the serial link. To measure the amount of electrical noise in the Fastrak system, 100 samples were acquired over 10 seconds with the receiver stationary on the wheel. The measurements were repeated with the wheel at a mean distance of 43.8 cm from the centre of the Fastrak receiver. A further repeat was carried out with the ultrasound machine switched on.

The position and orientation data were stored in ASCII and transferred to a spreadsheet program (Microsoft Excel). Quarternions were used to calculate the direction cosines of the LOS, LOH and LOP vectors as described in chapter 2. Sector angles were calculated by taking the arcosine of the sum of the product of the x,y and z direction cosines (Stroud 1984). As the wheel is rotated in 15^{o} increments, the LOS and LOH vectors should change by 15^{o} and the LOP vector by 0^{o}. The distance between the position of the centre of the receiver should be 2.61 cm (figure 5.1). This represents the length of the chord across the ends of a 15^{o} sector of a circle with a radius of 10 cm. The angle could be set within half of the 0.25 mm thick 15^{o} marks around the perimeter of the wheel corresponding to an error of $\pm 0.11^{o}$

5.2.3 Results

Figure 5.2(a) shows a plot of chord length versus wheel rotational angle with the receiver at a mean distance of 31.8 and 43.8 cm respectively. The dotted lines represent the expected chord length (2.61 cm) $\pm$ 1 mm respectively. Figure 5.2(b) shows a similar plot

for sector angle, the dotted lines represent the expected sector angle (15^o) ± 0.5^o respectively. Note that with the receiver at the closest mean distance from the transmitter, the chord length is within ~1 mm of the actual value and the sector angle within 0.5^o, even when the receiver is only about 8 cm above the couch. Table 5.1 compares the mean chord lengths and angles for the two distances. Over a complete rotation, the mean LOH sector angle was virtually identical to the LOS (15.038 ± 0.699^o for the LOS and 15.044 ± 0.728^o for the LOH). The mean LOP sector angle was 1.0 ± 0.7^o. Note that the errors are smaller when the transmitter and receiver are closer together. This arises as the signal received by the receiver is stronger closer to the transmitter resulting in a higher signal to noise ratio.

Figure 5.3(a) shows a plot of two successive chord length measurements at a mean distance of 43.8 cm. The measurements were repeated a third time with the ultrasound machine switched on. As there was no significant difference between the two plots with the machine off and on, the machine-on plot has been omitted in the interests of clarity. Figure 5.3(b) shows a Bland-Altman plot of the same data. Figure 5.4(a) and (b) are similar to figure 5.3 but for sector angle. Table 5.2 shows the mean error for the repeat measurements made in the middle and on the left and right sides of the couch.

Table 5.1 Variation in chord length and LOS sector angle as the wheel is rotated in 15^o increments given as the mean ± standard deviation. Tx and Rx are abreviations for the transmitter and receiver respectively.

Tx - Rx distance (cm)	chord length (cm)	sector angle (degrees)
43.8 (36.7 - 51.2)	2.71 ± 0.22	15.04 ± 0.7
31.7 (22.2 - 40.8)	2.60 ± 0.1	14.99 ± 0.34

(a)

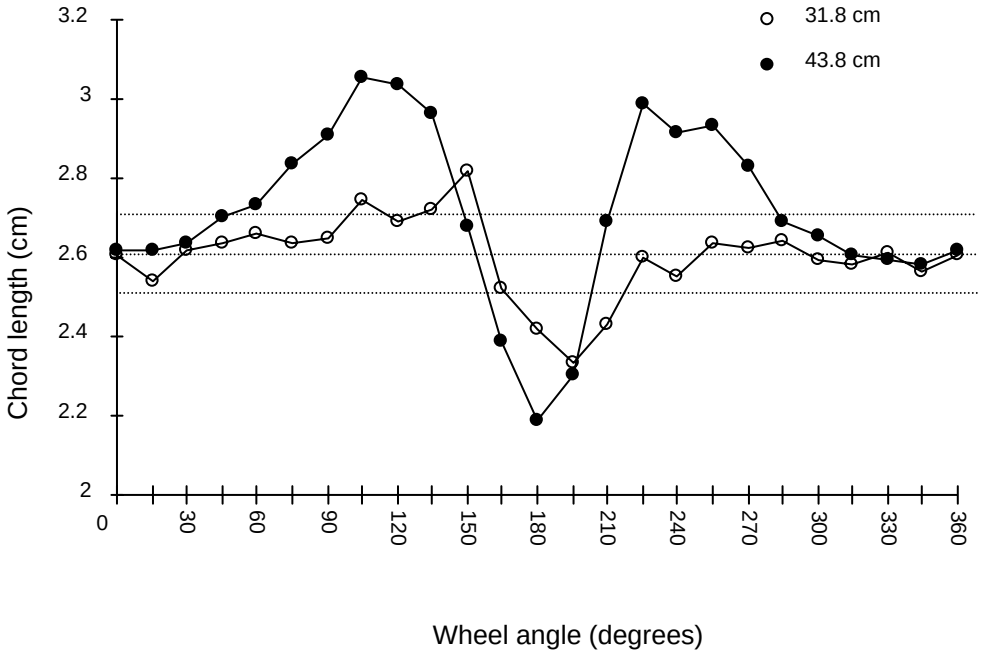

(b)

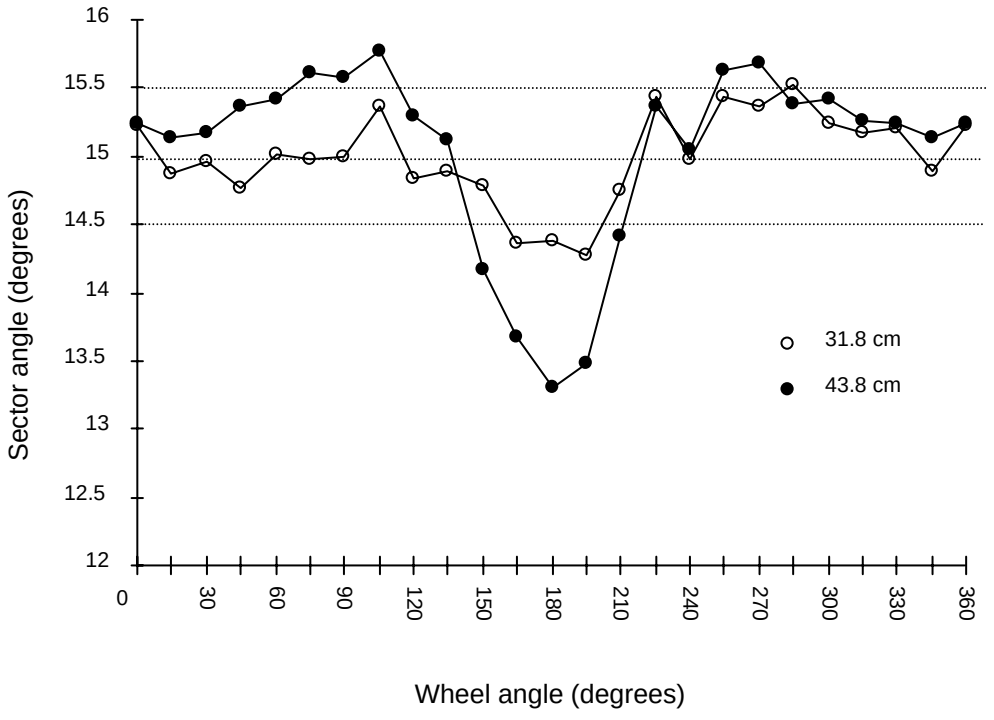

Figure 5.2 (a) Chord length and (b) sector angle versus wheel angle with the receiver at a mean distance of 31.8 and 43.8 cm from the transmitter respectively.

(a)

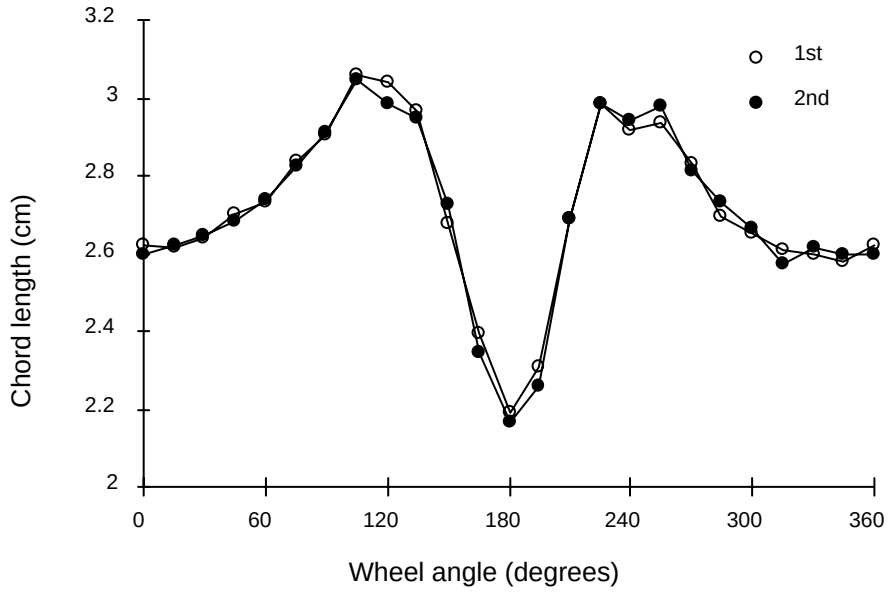

(b)

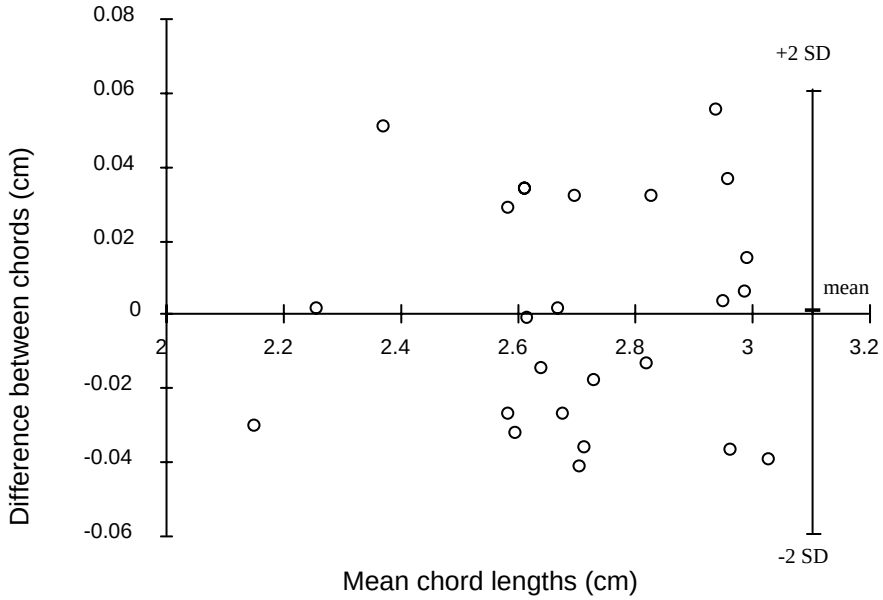

Figure 5.3 (a) Repeat chord length measurements with a mean distance between the receiver and transmitter of 43.8 cm. (b) Bland-Altman plot of the same data.

(a)

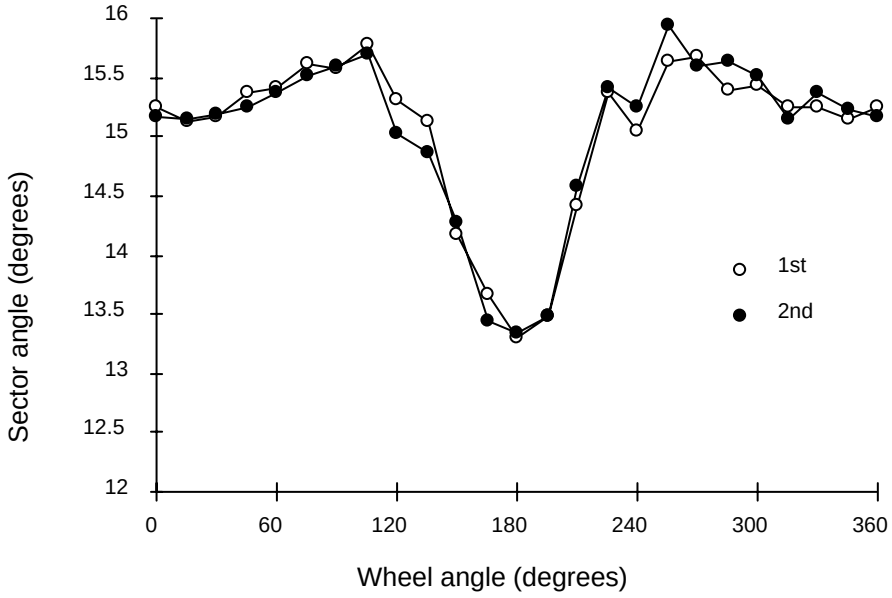

(b)

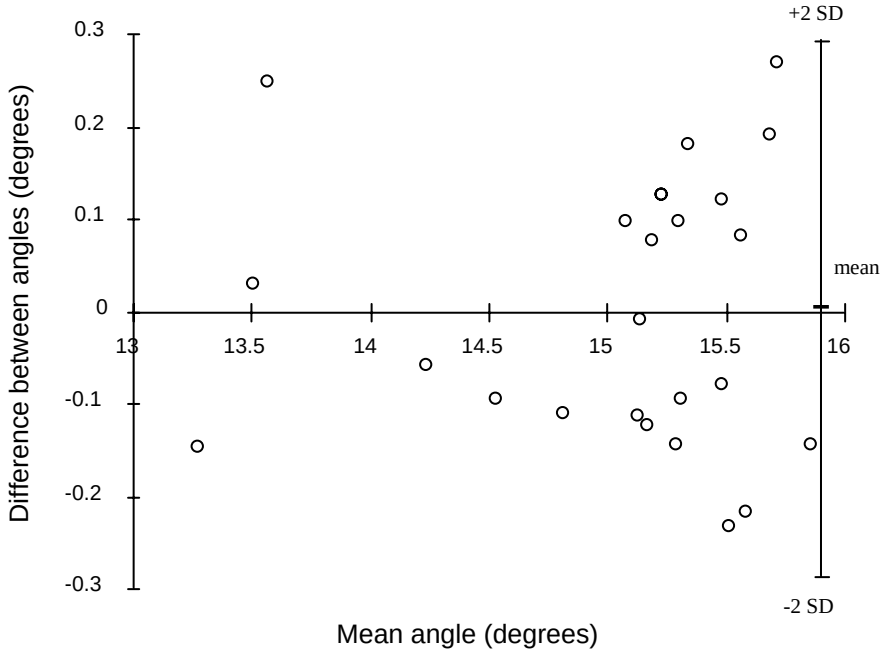

Figure 5.4 (a) Repeat sector angle measurements with a mean distance between the receiver and transmitter of 43.8 cm. (b) Bland-Altman plot of the same data.

Table 5.2 Agreement between repeat receiver - transmitter (Rx-Tx) distance and Rx LOSx angle measurements expressed as the mean ± SD of the difference between corresponding repeat measurements.

position	Rx-Tx distance (cm)	Rx LOSx angle (deg)
left	0.002 ± 0.0007	0.11 ± 0.12
middle	0.006 ± 0.0023	0.50 ± 0.09
right	0.003 ± 0.0024	0.01 ± 0.05

The general noise in the system was assessed with the receiver at 22.3 and 39.3 cm respectively. The mean values are shown in table 5.3, and figure 5.5(a) shows a plot of transmitter - receiver distance versus time. 100 samples were acquired over 10 s (Rx–Tx distance of 39.3 cm) . Figure 5.5(b) is a plot of LOS angle with respect to the x axis of the transmitter versus time. Regression lines have been plotted on these two graphs along with the correlation coefficients. Each graph has been smoothed to give the semblance of an analogue signal (although the statistics were calculated on the un-smoothed data).

Table 5.3 Estimates of the noise in measuring position and LOS x orientation with the receiver stationary at two distances from the transmitter.

Tx - Rx distance (cm)	position (cm)	angle (degrees)
39.3 (noise)	39.3429 ± 0.0012	56.5706 ± 0.0069
22.3 (noise)	22.2823 ± 0.0013	83.2168 ± 0.0033

Notice that the chord length and sector angle are very close to the actual values of 2.61 cm and 15^{o} respectively when the receiver is near the top - i.e. more than 20 cm above the couch. (N.B. the receiver is at the top of the wheel when the wheel is in the zero position). Figure 5.6(a) shows a scatter plot indicating the degree of correlation between chord length and sector angle as the wheel is rotated, and figure 5.6(b) shows a scatter plot between Rx-Tx distance and LOSx angle noise signals.

(a)

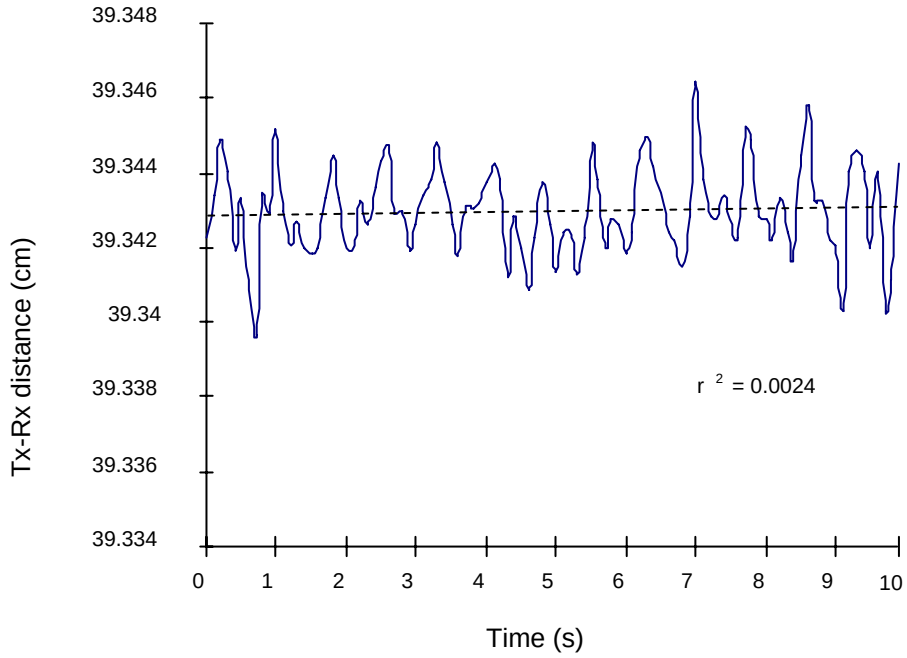

(b)

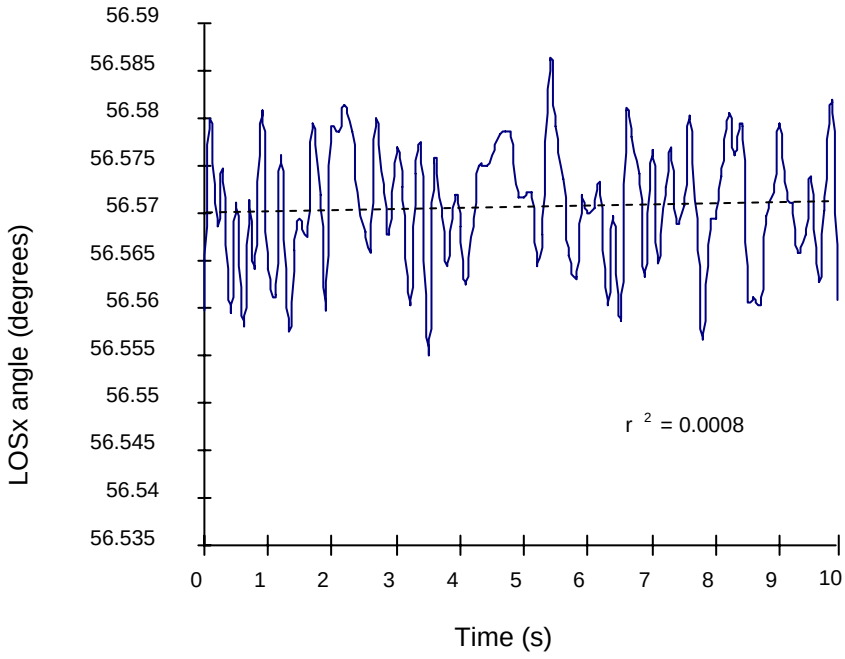

Figure 5.5 (a) Variation in Rx-Tx distance with time. (b) variation of Rx LOSx angle with time.

(a)

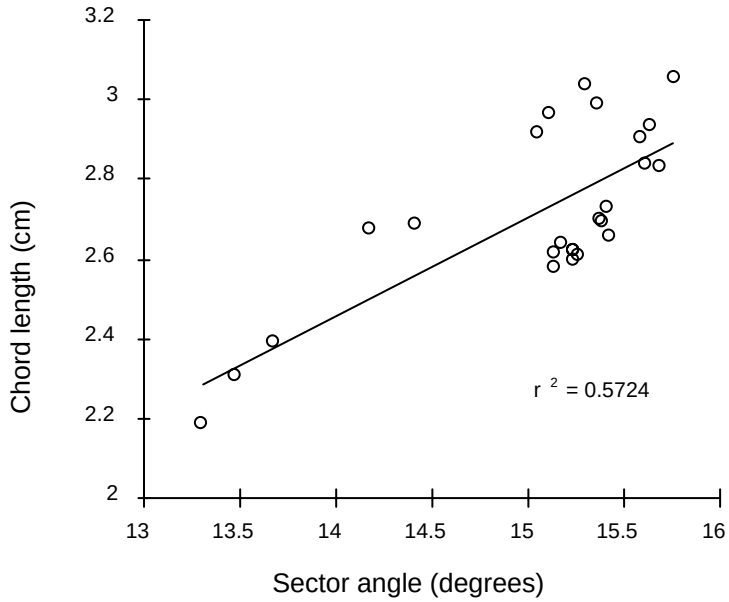

(b)

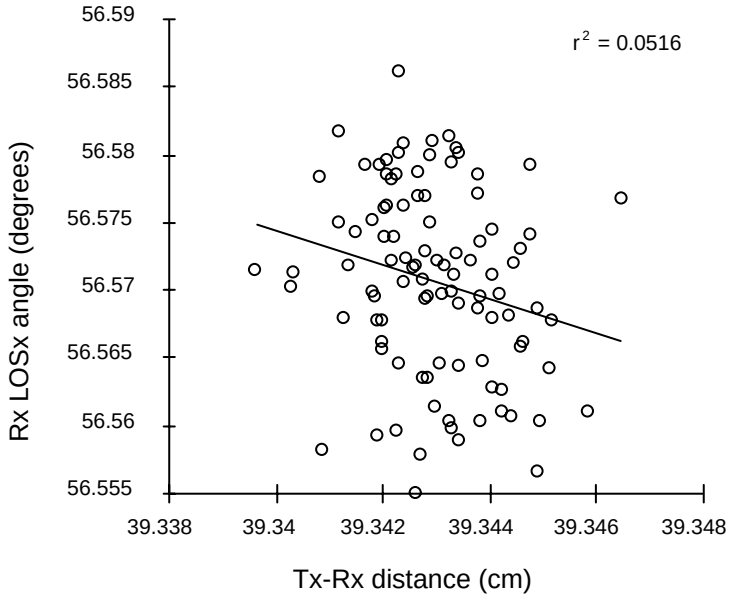

Figure 5.6 (a) Correlation between chord length and sector angle for a complete rotation of the wheel. (b) Correlation between the Rx-Tx distqance and Rx LOSx angle noise signals.

The values appear to be purely random with mean difference values very close to zero. The noise is probably internal electronic noise as there is almost no correlation (r^2 = 0.05) between position and orientation. External influences would be expected to affect both position and orientation, as it does, for example, when the wheel is rotated on the couch (r^2 = 0.57). Below about 20 cm, the metal frame of the couch has an influence on the transmitted signal, which affects both position and orientation.

5.2.4 Discussion

In normal use the receiver would not be rotated through 360^o therefore the error is likely to be considerably less that the mean values for a complete rotation of the wheel. In the clinical situation, the transducer would probably not be moved more than $\pm 30^o$ from the vertical. With the receiver at a mean distance of 37 cm from the transmitter, a 60^o (-30 to $+30^o$) excursion at the top of the wheel, corresponding to a distance of 10 cm, the mean sector angle was measured as 15.18 ± 0.06^o ($1.2 \pm 0.4\%$) and the mean chord length 2.609 ± 0.019 cm ($0.05 \pm 0.73\%$). Over a distance of 10 cm, a 0.18^o error in measuring angle would result is a position error of 0.3 mm.

It may also be inferred from these results that the centre of the receiver is very close to the position indicated by the manufacturer and the x,y,z transmitter and receiver coils are accurately aligned. Overall, the results obtained in this experiment are consistent with the accuracy values quoted by the manufacturer. However, the separation of the receiver and transmitter should be no greater than 32 cm.

5.3 Material interposed between transmitter and receiver

5.3.1 Introduction

An experiment was conducted to assess the effect of interposing various materials between the Fastrak transmitter and receiver. In the experiments described in this thesis, a clear line of sight was generally maintained between the transmitter and receiver. However in some cases (more so in clinical use) a hand, arm or cable can get in the way. Do these items have a significant effect on the Fastrak measurements?

5.3.2 Method

The transmitter and receiver were placed 50 cm apart on a plank of ply wood (1.8 x 5.2 x 94 cm) placed on a wooden table ~1.5 m in height. 50 cm was chosen as this is the likely to be a typical distance between the transmitter and receiver during normal operation. In some cases interposed materials were placed on a 1 cm high plinth (a roll of micropore tape) in order to ensure that a line drawn between the centres of the receiver and transmitter passed through the test material. Objects were placed half way between the receiver and transmitter with an estimated accuracy of ± 1 cm.

The table was placed in the middle of the scanning room well away from the ultrasound machine, computer and scanning couch. The table itself contained only a very small amount of metal - e.g. wheels, screws and clasps. The receiver and transmitter were actually suspended in space either side of the table top.

The Fastrak was connected to a PC and a terminal program used to log the position and orientation quarternions. Each object was put in place and 10 samples taken in about 5 s (this was effected by simply pressing the ‘P’ key in quick succession). Each object was then immediately removed and a further 10 samples taken to serve as a control. The two sets of 10 samples were acquired within 10 s of each other. The distance between the transmitter and receiver and the angle of the receiver LOSx vector relative to the x axis of the coordinate system of the transmitter were calculated using a spreadsheet (Microsoft Excel). Each set of 10 values were averaged.

5.3.3 Results

The differences between the before and after values are shown in table 3.3.

Table 5.4 Estimate of the error in measuring position (Δd) and orientation ($\Delta\theta$) with different materials interposed between the Fastrak receiver and transmitter 50 cm apart.

material	Δd (mm)	$\Delta\theta$ (^{o})
steel sheet	8.91	-0.54
aluminium sheet	3.63	-0.12
brass sheet	2.85	-0.25
steel rod	0.18	0.06
perspex sheet	-0.05	0.07
aluminium rod	0.60	0.03
wood	-0.06	0.07
brass rod	0.44	0.06
glasses	0.03	0.02
brass cylinder	1.31	-0.13
dead mains cable	0.00	0.01
live mains cable	0.70	0.23
hand	-0.06	0.05
us probe	0.11	-0.06
us cable	-0.06	-0.01
small perspex sheet	-0.04	0.01
Tx cable	0.00	0.00
Rx cable	-0.13	0.06

Metal sheets cause the largest perturbations, followed by metal rods. The only other cause for concern is a live mains cables – however, in the normal course of events this should never come between the receiver and transmitter.

5.3.4 Discussion

It should be borne in mind that the errors quoted in table 3.3 cannot be used to calculate absolute positional and angular error as a complete transformation matrix is required. However, as all of the quarternions are used to calculate all nine direction cosines

(equation 2.4), any perturbation will affect each direction cosine in some way. However, the values enable the materials to be compared in terms of their overall perturbing effect.
To characterise environmental effects completely, the translation and rotation of the receiver coordinate system relative to the transmitter is required. These values can be put into matrix form. Multiplication of the Fastrak values by the inverse of the matrix corrects the values. This technique could be used to compensate for metal.

In conclusion it can be stated that ideally a clear path should be maintained between the transmitter and receiver. This can generally be achieved by judicious placement of the transmitter.

5.4 Effect of a cathode ray tube

5.4.1 Introduction

Cathode ray tubes (CRTs) are a source of electromagnetic radiation and therefore could pose a problem if close to the Fastrak. CRTs are integral to ultrasound scanners and part of the computer system connected to the Fastrak and so are likely to be somewhere in the vicinity of the transmitter and receiver.

5.4.2 Method

The receiver and transmitter were placed 50 cm apart on a piece of ply wood (as in the previous section) and placed on a wheeled wooden trolley. The probe was placed directly on top of the monitor of an ultrasound machine (Tosbee Ecocee) and then at 20,30,40,50 and 60 cm away. The probe was oriented so that the receiver was always closest to the CRT. Between CRT measurements the probe was moved to the centre of the room to acquire control values. 10 samples were acquired within 5 s. Collection and analysis of the data was carried out as previously described.

5.4.3 Results

Figure 5.7(a) shows a plot of Rx - Tx distance versus Rx distance from the CRT, figure 5.7(b) shows a similar plot for receiver LOS x angle. Note that the perturbing effect appears to be insignificant beyond about 60 cm.

(a)

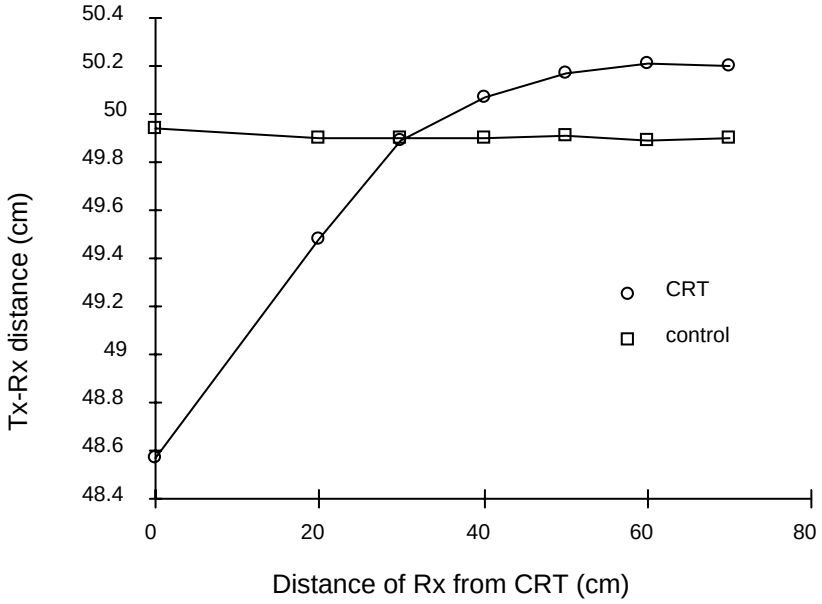

(b)

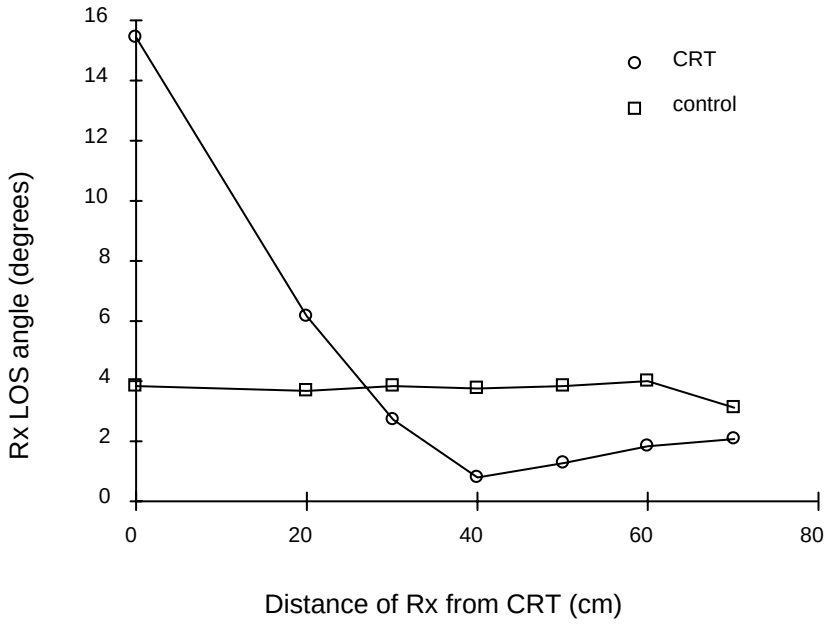

Figure 5.7 (a) Variation in Rx-Tx separation with Rx distance from the CRT. (a) Similar plot for Rx LOSx angle.

5.4.4 Discussion

These results suggest that CRTs and ultrasound machines do not pose a significant problem if care is exercised to ensure that the receiver is further away than 60 cm.

5.5 Effect of a metal framed scanning couch

5.5.1 Introduction

Most scanning couches are built around a metal frame (usually steel). This is likely to be the closest metal to the Fastrak system and so is a cause for concern. This experiment was designed to answer the question: at what height above a metal couch can the Fastrak system safely be used?

5.5.2 Method

A probe was constructed by firmly attaching the receiver and transmitter to a wooden board. The receiver and transmitter were separated by about 20 cm with the receiver line-of-sight axis approximately anti-parallel to the x axis of the transmitter (figure 5.8).

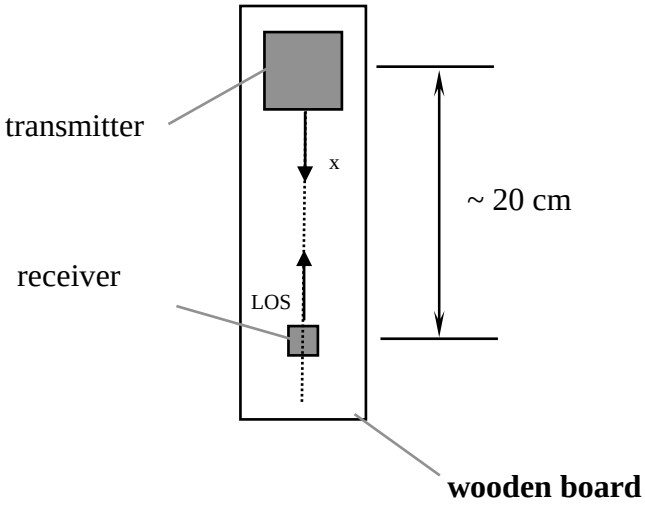

Figure 5.8 Schematic diagram of probe.

(This orientation was chosen to ensure that the cables did not come between the receiver and transmitter). Although the exact distance and orientation do not matter, it is very important that the receiver and transmitter are firmly fixed so they do not move with

respect to each other. 20 cm is a compromise between having the receiver and transmitter close enough to probe a reasonably small region and far enough apart to be representative of the actual distance in normal use (~ 50 cm). As the receiver and transmitter are securely attached, the physical distance and orientation will remain constant as the probe is moved around. However, environmental factors may perturb the transmitted field and therefore cause the measured position and orientation of the receiver to vary from the unperturbed value.

A tape measure was attached to one side of a wooden pillar (as in figure 4.1), and the probe elevated by hand against the scale in increments of 1 cm (with an estimated error of ± 1 mm). The transmitter-receiver axis was oriented vertically with the transmitter above the receiver. The receiver and transmitter faced towards the midline of the couch. The probe could have been oriented in other ways, but this particular orientation was chosen as it more accurately reflects the typical clinical situation with the transmitter above the ultrasound probe. This operation was carried out in the middle of the couch and to the left and right with the probe suspended above the metal side struts. The ultrasound machine was at the top end of the couch on the left hand side (as in figure 4.1). To assess the level of electronic/background noise, 100 readings were taken in 10 s with the probe placed directly on the couch with the Rx-Tx axis parallel to the long axis of the couch. This process was repeated with the Rx-Tx axis normal to the long axis of the couch.

5.5.3 Results

Figure 5.9(a) shows a plot of the Rx-Tx distance versus Rx height above the couch in the middle and to the left and right of the couch. Figure 5.9(b) is a similar plot for Rx LOS x angle. Note that the Rx-Tx distance measurements are perturbed more in the centre of the couch compared to at the sides. Perhaps this is because, on average, more metal is proximate to the probe when it is above the middle of the couch than at the sides. Over the entire range of the experiment (8 - 38 cm), the perturbation at the sides of the couch was less than 0.4 mm, and in the middle less than 0.8 mm.

However, the situation appears to be reversed for angle. There is very little perturbation in the middle of the couch, whereas at the sides it is of the order of 1.5^{o} between 8 and 20 cm above the couch. In the middle of the couch there are roughly equal amounts of metal

(a)

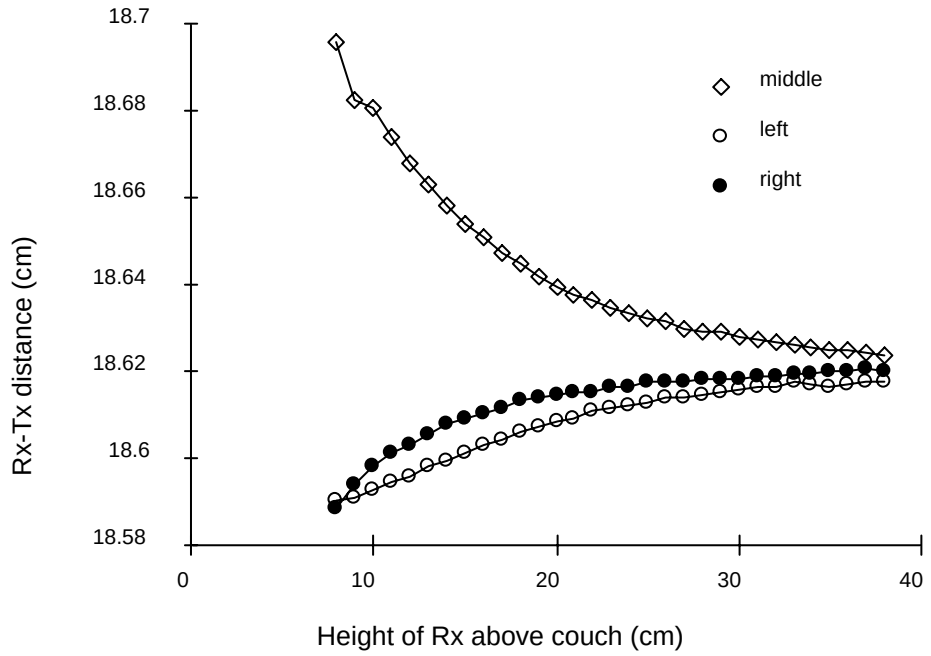

(b)

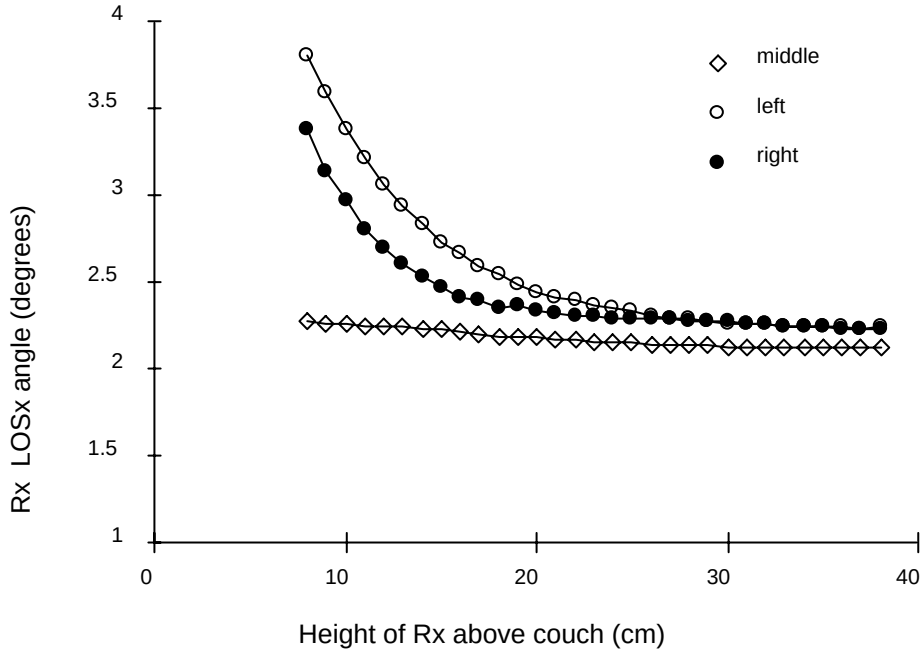

Figure 5.9 (a) Plot of probe Rx-Tx separation versus height above couch for three positions. (b) Similar plot for angle.

(a)

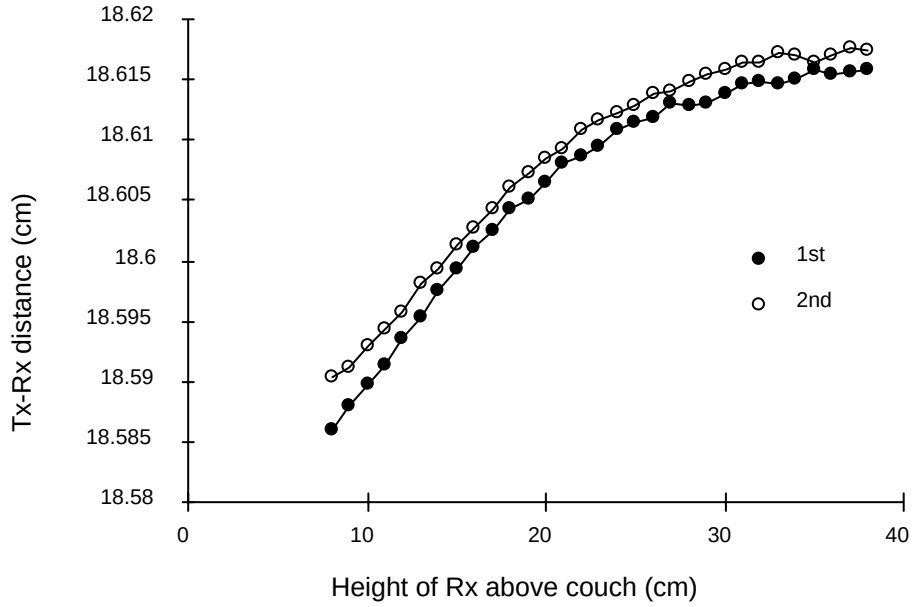

(b)

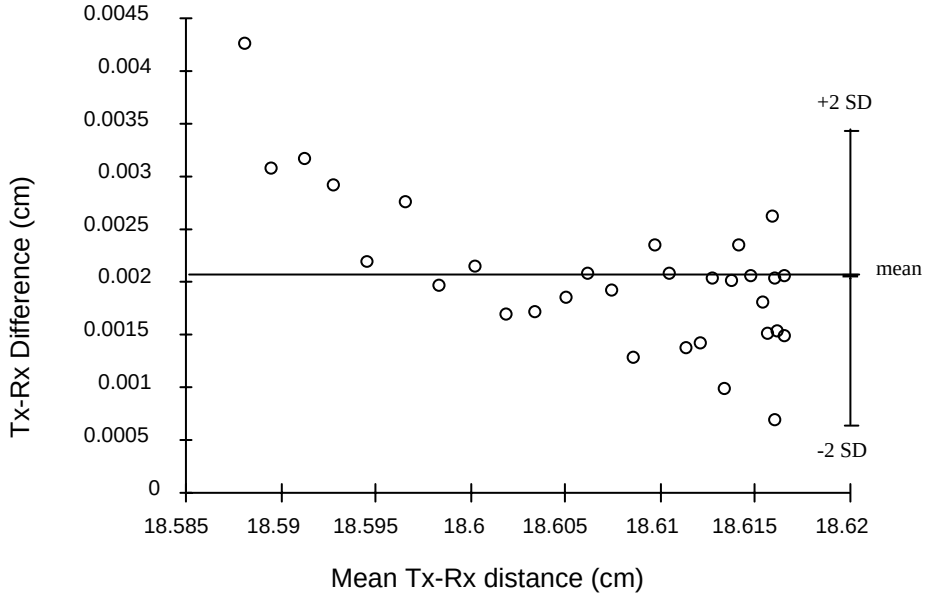

Figure 5.10 (a) Repeat measurements of Rx-Tx distance versus probe height above couch. (b) Bland-Altman plot of the same data.

(a)

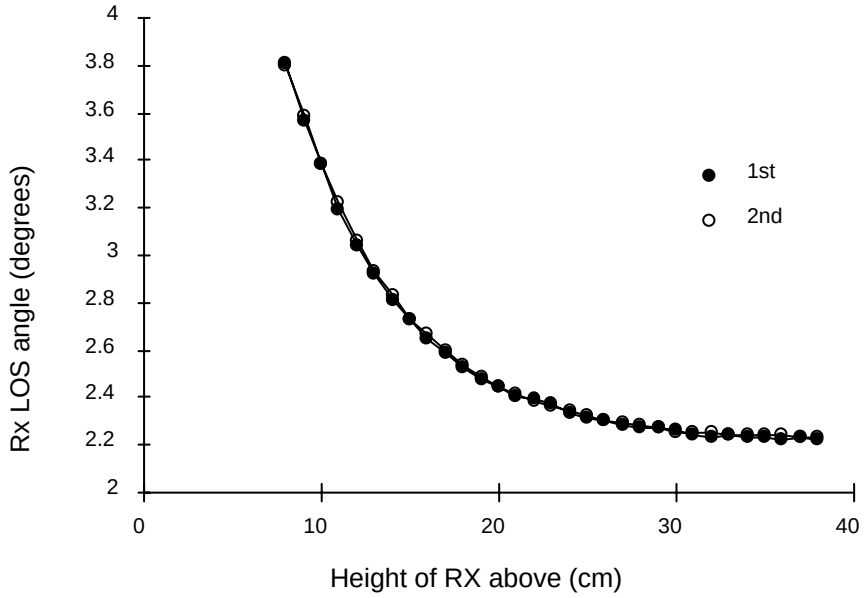

(b)

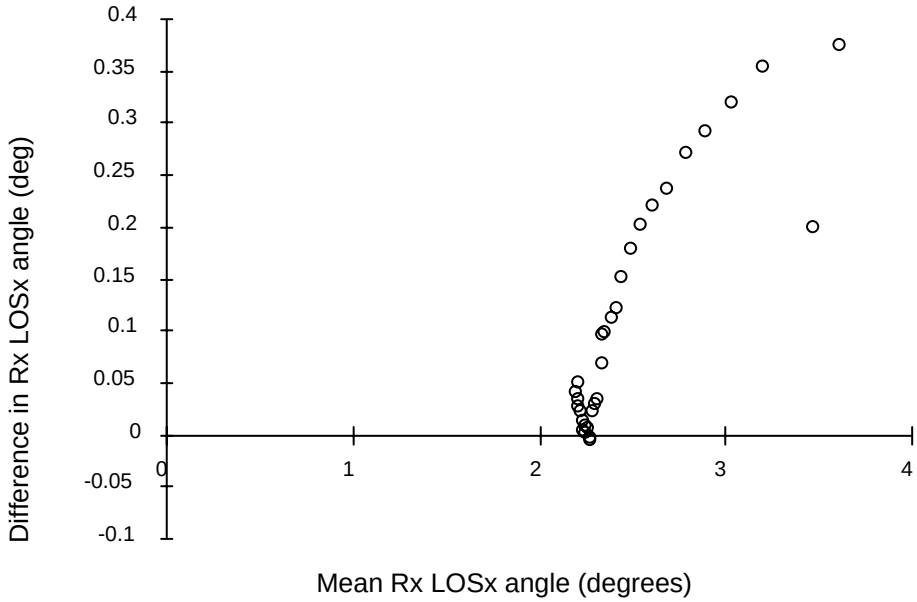

Figure 5.11 (a) Repeat measurements of Rx LOSx angle versus probe height above couch. (b) Bland-Altman plot of the same data.

either side of the probe which is probably having a balancing effect on the signal. At the sides of the couch the distribution of metal is asymmetric resulting in greater perturbation in angle. The angle values appear to converge asymptotically to different base values. This is probably due to subtle differences in the local metallic/electromagnetic environment (a background effect).

Figure 5.10 (a) shows repeat measurements of Rx-Tx distance versus height. Figure 5.10(b) shows a Bland-Altman plot of the same data. Note that the differences between the two Rx-Tx distance readings tends towards zero as height increases. This is also seen in the figure 5.11. This indicates that the metal in the couch increases the error in measurements. The noise was an order of magnitude lower than the values shown in table 5.3. There was no significant difference between the orientation of the probe on the couch, or whether the machine was on or off.

5.5.4 Discussion

The results show that there is little perturbing effect more than 20 cm above the couch. Therefore, if care is exercised, there is no problem in using a metal framed couch. However, it should be pointed out that the situation might be different for different couch designs. The electrical/background noise is an order of magnitude smaller than in 5.2 probably because the Rx and Tx are closer together and the signal strength is proportional to the third power of the radius (section 4.2.2).

5.6 Effect of an ultrasound transducer

5.6.1 Introduction

The Fastrak receiver should be attached to an ultrasound transducer in such a way that it does not interfere with scanning, and is not too close to for metal within the transducer to perturb the signal.

5.6.2 Method

The 20 cm probe was placed with the Rx-Tx axis at right angles to the long axis of the ultrasound transducer and parallel to the image plane. The probe was oriented with the receiver closest to the transducer.

(a)

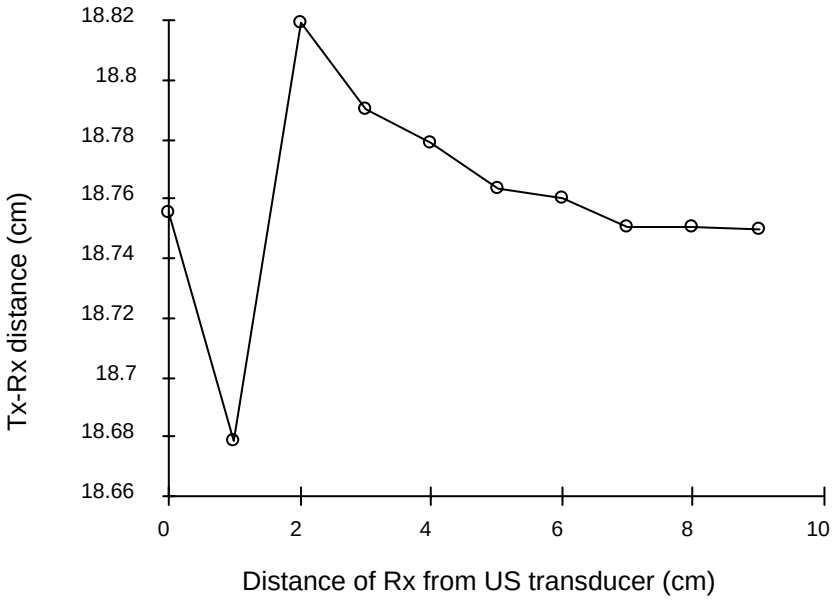

(b)

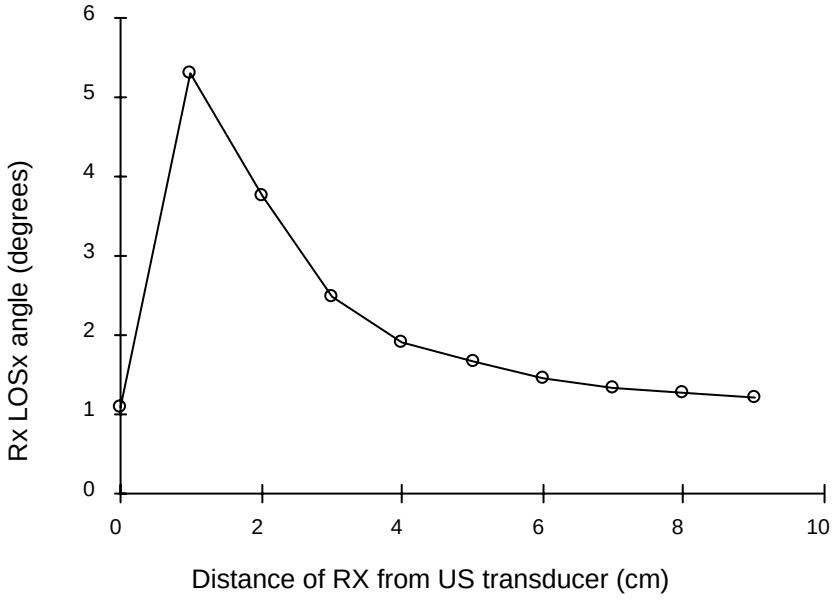

Figure 5.12 (a) Probe Rx-Tx separation versus distance from an ultrasound transducer. (b) Similar plot for Rx LOSx angle.

Duplicate readings were taken at 0 - 9 cm in 1 cm increments (with an estimated error of ~ ± 2 mm). The ultrasound machine was switched on, but the transducer was not scanning.

5.6.3 Results

Figure 5.12(a) shows a plot of Rx-Tx distance versus Rx distance from the transducer. Figure 5.12(b) is a similar plot for Rx LOSx angle. In each case the mean of the duplicate readings have been plotted. In figure 5.12(a) the perturbation between 2 and 6 cm from the transducer is less than 0.8. The greatest disturbance is between 0 and 2 cm. Curiously, there appears to be very little perturbation with the receiver touching the transducer.

The situation is similar for angle although the pattern is slightly different. There is a much more marked perturbation of angle, although beyond 4cm the perturbation is less than 0.5^{o}. When the receiver is touching the ultrasound transducer the perturbation is very small (~ 0.12^{o}), which is less than the stated RMS error of 0.15^{o}.

5.6.4 Discussion

These results show that the Fastrak receiver can be placed within 7 cm of the transducer case with little perturbation of the measurements. The receiver shown in figure 4.3 is 8 cm from the closest point of the transducer case. The fact that there is little effect when the receiver is placed directly onto the transducer case suggests that it may be possible to strategically place the receiver directly onto a transducer case without any significant degradation of the results. The receiver was in fact placed directly onto the transducer case for some of the *in vitro* experiments described in the next chapter. However, a test scan with the receiver attached directly to an Acuson 128XP/3 transducer resulted in skewed ROIs. Therefore an attachment was made for the XP/10 probe.

5.7 Effect of an ultrasound transducer cable

5.7.1 Introduction

In many cases the Fastrak receiver is likely to be close to the transducer cable and therefore may have a perturbing effect.

(a)

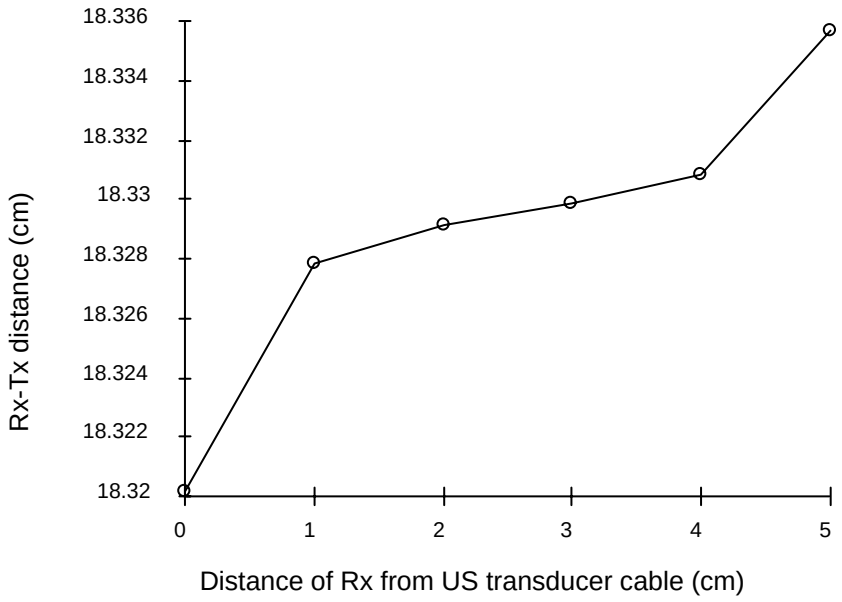

(b)

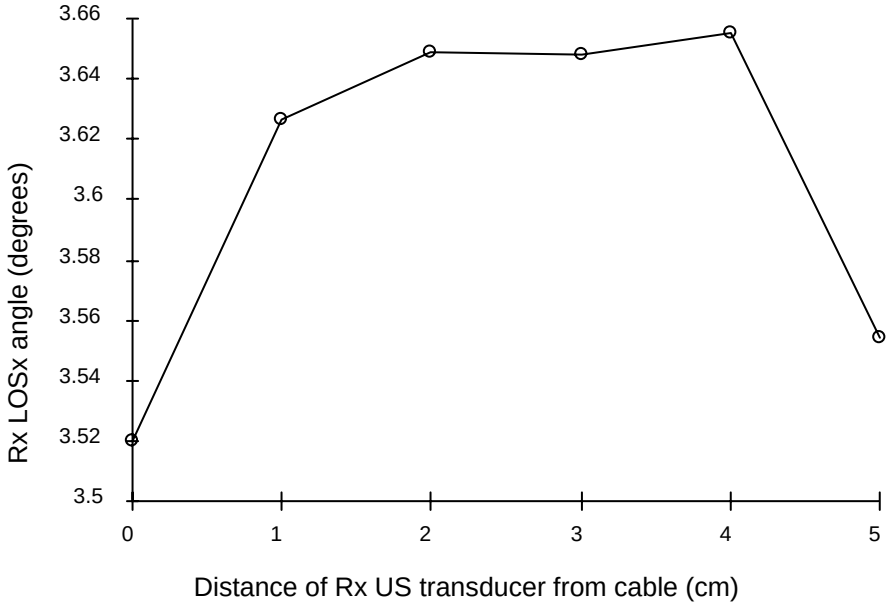

Figure 5.13 (a) Probe Rx-Tx separation versus distance from ultrasound transducer cable. (b) Similar plot for Rx LOSx angle.

5.7.2 Method

A similar experiment was carried out to the one described in section 5.7. The probe was placed at between 0 - 5 cm from a transducer cable oriented normally to the Rx-Tx axis. The ultrasound machine was on. Duplicate measurements were made as in experiment 5.7.

5.7.3 Results

Figure 5.13(a) shows a plot of Rx-Tx distance versus Rx distance from an ultrasound cable. Figure 5.13(b) is a similar plot for Rx LOSx angle. The maximum perturbation in Rx-Tx distance and angle were < 0.16 mm and $< 0.14^{o}$ respectively which are very much smaller than the quoted RMS values (0.8 mm and 0.15^{o}).

5.7.4 Discussion

The results show that the cable is of little concern, even if the receiver is touching the cable.

5.8 Effect of a steel sheet

5.8.1 Introduction

Most metal within the vicinity of the Fastrak will be small. In some cases metallic sheets may be present within the environment.

5.8.2 Method

The probe was used to investigate the effect of a steel sheet (about 50 x 50 cm) placed at varying distances behind the receiver. Data collection and analysis was carried out as previously described.

5.8.3 Results

Figure 5.14 (a) and (b) show the variation in position and LOS x angle respectively with distance. Going from 100 cm to 0 cm, the maximum perturbation is about 1.4 mm and 0.4^{o} for position and angle respectively.

(a)

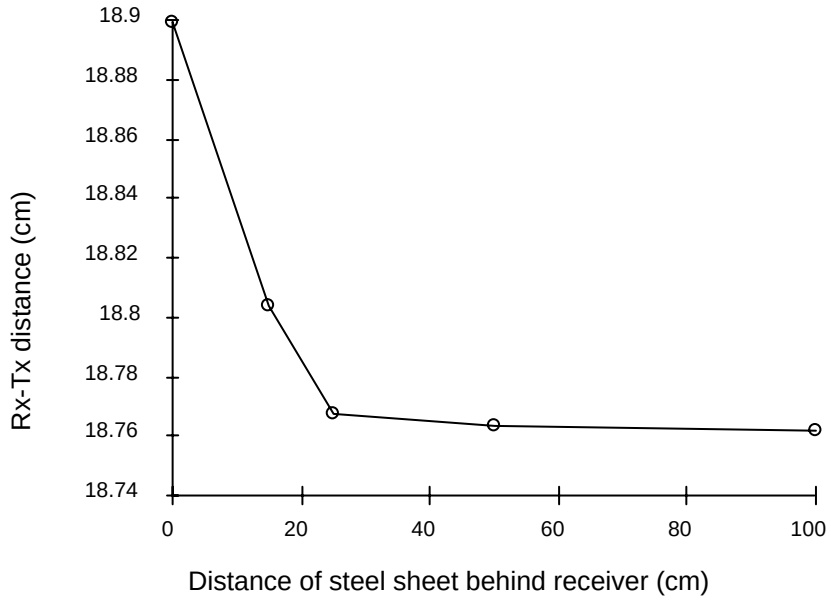

(b)

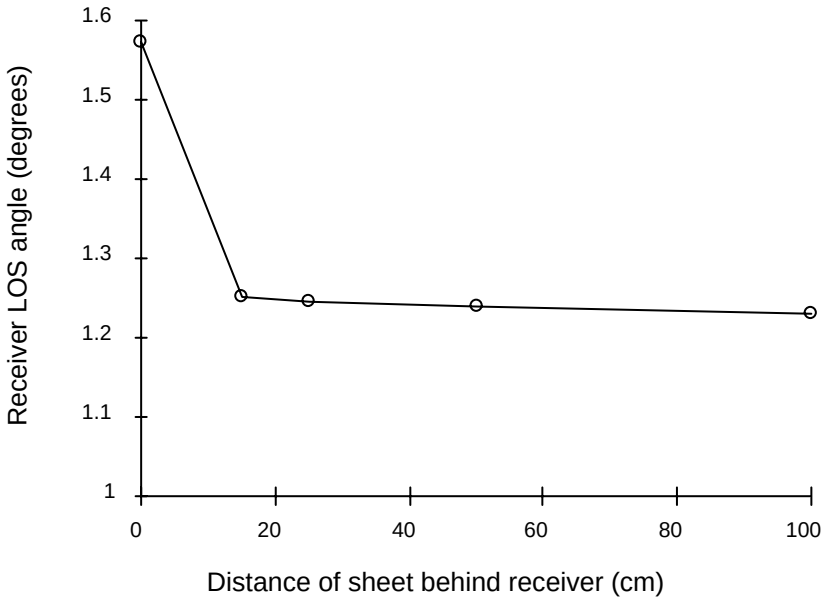

Figure 5.14 (a) Variation in Rx –Rx separation with a metal sheet at various distance behind the Rx. (b) Similar plot for Rx LOSx angle.

5.8.4 Discussion

The metal sheet does have a significant perturbing effect, but this is perhaps smaller than expected. The situation may well be different if the receiver and/or transmitter were inside a metal box, however the Fastrak would not normally be used in such a situation.

5.9 Summary

These tests are quite encouraging and show that the Fastrak is useable in a clinical setting. The results presented here are consistent with those reported by Gardner et al (Kelly et al. 1994) i.e. that there is very little perturbing effect on the Fastrak receiver when it is placed more than 7 cm away from an ultrasound transducer and is greater than 20 cm above a metal framed couch. The wheel results show that the error reduces with the separation between the receiver and transmitter.

However, care obviously needs to be taken to ensure that conductive materials are not interposed between the transmitter and receiver, and that the receiver and transmitter are more than 60 cm away from an ultrasound scanner or a cathode ray tube. Heavy duty power cables could also be a problem - which could arise if the system was being used close to cables feeding an X-ray machine or near a lift shaft. MR scanners are another potential source of interference.

CHAPTER 6

In vitro experiments

6.1 Introduction

This chapter describes the three main experiments carried out to evaluate the overall accuracy of the system in scanning cadaveric organs and balloons. These are:

1. Hand scanning of water filled balloons on a metal framed scanning couch.
2. Scanning of cadaveric porcine kidneys on four different ultrasound machines.
3. Ultrasound, CT and MR scanning of cadaveric fetal livers.

These three experiments were designed to answer the following questions:

1. How do the volume techniques compare - i.e. the ellipsoid, planimetry, centroid tetrahedral, slice tetrahedral, CAN, and ray trace algorithms?
2. How do the radial, parallel and slanted scan techniques compare?
3. Are there significant differences between ultrasound machines?
4. How does the accuracy of estimating volume by US compare with X-ray CT and MRI?

6.2 Free hand scanning of balloons

6.2.1 Introduction

Water filled balloons were chosen for this experiment for two main reasons, (1) the borders are clearly delineated in ultrasound images and (2) the actual balloon volume can be very accurately determined by weighing (assuming a density of water of 1 g/ml). Therefore the accuracy in scanning balloons is likely to reflect the minimum error possible with a particular scanner.

6.2.2 Method

Ten balloons (ranging in size from 13.6 - 141.6 ml) were filled with water and the necks tied off with surgical suture. The balloons were attached to a Perspex base by rubber band and placed in a plastic container of tap water at 26 ^{o}C.

The container was placed on an examination couch (as in figure 4.1) in approximately the same position as a patient undergoing an ultrasound scan, although the height of the Fastrak receiver was slightly lower than it would have been for a patient. The balloons were scanned with an Acuson 128XP/10 with a 3.5-MHz curvilinear probe. The transducer was moved continuously across the balloons by hand. The Fastrak receiver was attached to the ultrasound probe as shown in figure 4.3. The operator was an experienced ultrasonographer who used the system in a clinical trial designed to assess the benefits of 3D-US volume measurements in fetal medicine.

One of the balloons was scanned three times and ROIs drawn by one observer to assess scan repeatability. To estimate intra and inter-observer error, the edge balloon was outlined three times by three observers (the author plus two others). The t-test was used to compare means and the F-test to compare variances.

The Fastrak transmitter was attached to a purpose built wooden stand (figure 4.1) and suspended above and to the side of the couch. During scanning the ultrasound transducer was oriented so that there was a clear line of sight between the transmitter and receiver, which were separated by between 0.5 and 1m. Twenty images with a 328 x 228 matrix were acquired for each balloon over a period of 10 s (two images per second). Figure 6.1 shows an example of an image through one of the balloons. The pixel size was 0.353 and 0.376 mm in the x and y directions respectively.

After scanning, the balloons were weighed before and after emptying using an electronic balance (Sartorius MC1, Sartorius AG, Gottingen, Germany) to an accuracy of $\pm$ 0.01 g. The volume of the water in each balloon was assumed to be the total weight of the balloon minus the weight of the rubber and suture divided by the density of water. The image and position data files were transferred via a local area network (LAN) to the Titan graphics computer. The inner edges of the balloons were outlined using a mouse and the

algorithms described in the previous chapter used to transform points from image space into 3D coordinates.

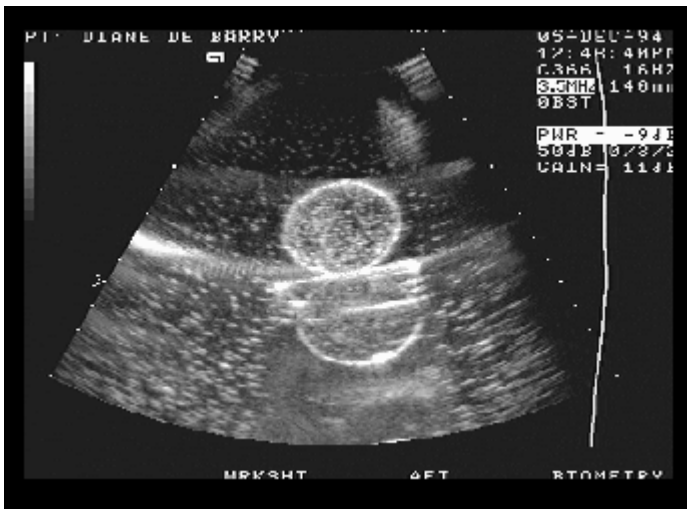

Figure 6.1 Cross-sectional image through a water filled balloon.

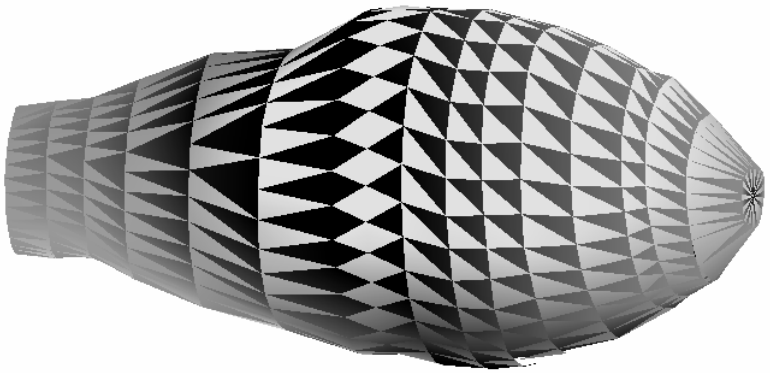

Figure 6.2 Triangle mesh representation of a hand-scanned balloon.

The transformed points were then connected into a triangle mesh as shown in figure 6.2. The surface is displayed as a sequence of alternating dark and light triangular facets and can be scaled, translated and rotated about the x,y,and z axes. This enables the operator to view the object from all directions and check that the meshing algorithm has performed

correctly. Sometimes it is necessary to retrace a ROI. The volumes were calculated using the algorithms described in chapter 2.

The volumes were corrected to take into account the difference in the velocity of sound in tissue at 37 ^{o}C (1540 ms^{-1}) and water at 26 ^{o}C (1495 ms^{-1}) (Bamber and Hill 1979). This discrepancy results in an overestimation of distance in the direction of sound propagation of 2.92%; therefore the calculated volumes were reduced by a factor of 0.9708. (Note that this is a one dimensional correction of volume. Also, sector angle refraction errors have been ignored). The mean percentage error was calculated by dividing the measured volume by the (signed) difference between the measured and calculated volumes. The F-test was used to assess the significance of the differences between the variances and in cases where the variances were not significantly different, one-way analysis of variance was used to assess the significance of differences between the means.

6.2.3 Results

Figure 6.3 (a) shows a plot of measured versus calculated volume for four of the six volume algorithms. (To simplify the graph the centroid tetrahedral and CAN volumes have been excluded). Figure 6.3 (b) shows a Bland-Altman plot of the same data. The actual values plotted are listed in table 6.1.

Table 6.1 Balloon volumes, vol = volume by weight, el = ellipsoid, pla = planimetry, c.tet = centroid tetrahedral, s.tet = slice tetrahedral, rta = ray tracing algorithm.

balloon	vol	el	pla	c.tet	s.tet	rta	can
1	23.9	21.3	24.2	24.0	24.1	24.0	24.1
2	44.4	55.8	46.8	46.5	46.6	46.5	46.5
3	36.9	36.3	38.3	38.7	38.7	38.7	38.7
4	40.2	47.0	40.9	40.9	41.0	40.9	40.9
5	72.6	114.7	73.1	72.7	72.5	71.6	72.7
6	141.6	157.7	141.4	139.1	143.1	139.8	139.4
7	37.3	47.8	36.6	36.6	36.6	36.5	36.6
8	94.1	99.9	93.4	94.1	94.2	93.5	94.1
9	13.5	12.7	13.8	13.8	13.8	13.7	13.8
10	49.8	48.2	50.3	50.4	50.5	50.4	50.4

(a)

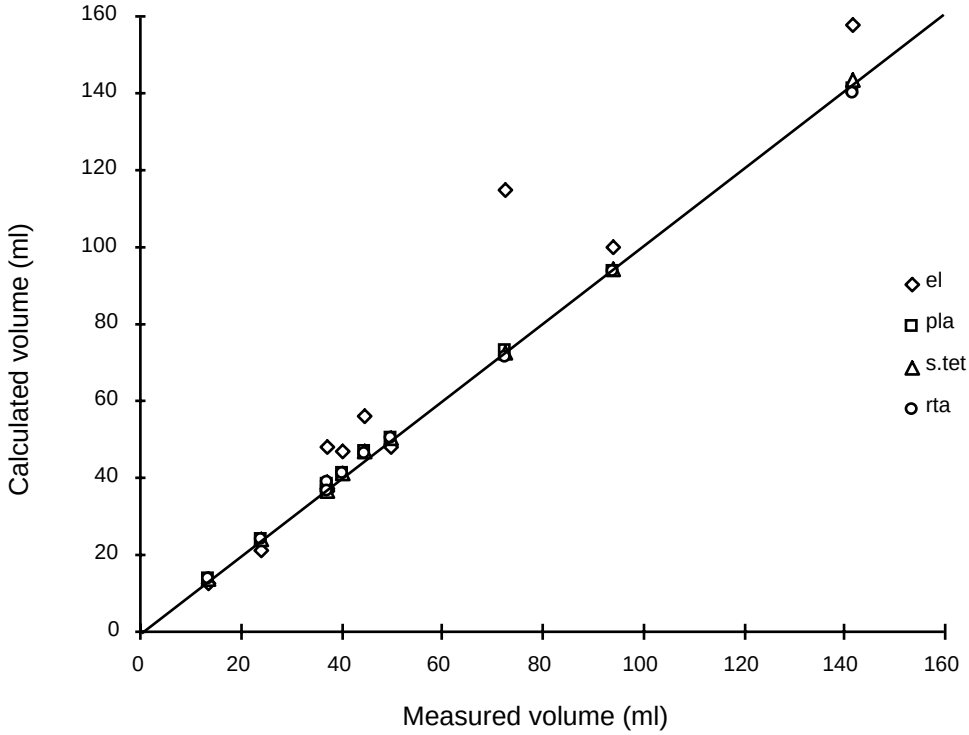

(b)

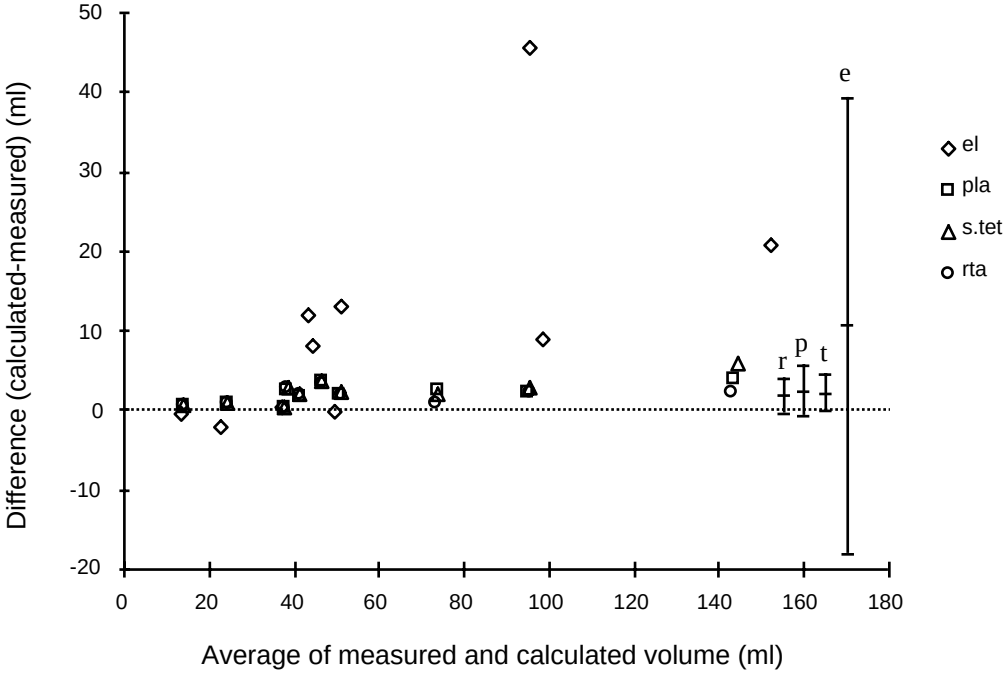

Figure 6.3 (a) Plot of measured balloon volume verses the volume calculated by the ellipsoid (el), planimetry (pla), slice tetrahedral (s.tet) and ray tracing (rta) methods. The line of identity is shown. (b) Bland-Altman plot of the same data.

Table 6.2 Summary of absolute and percentage errors for the calculated volumes compared to the actual volume as determined by weighing.

Algorithm	absolute error (ml)	% error
el	8.7 ± 13.4	12.4 ± 20.8
pla	0.4 ± 0.9	1.3 ± 2.1
c.tet	0.3 ± 1.3	1.2 ± 2.3
s.tet	0.8 ± 0.9	1.5 ± 2.1
rta	0.1 ± 1.2	0.9 ± 2.4
can	0.3 ± 1.2	1.2 ± 2.3

The intra and inter-observer error results are shown in table 6.3. There was no significant difference in intra and inter observer error (as determined by the t-test and F-test).

Table 6.3 Intra and inter-observer error expressed as the mean and standard deviation of the percentage difference in volume. Each observer outlined a single balloon three times. The same balloon was scanned three times and outlined by one observer. Symbols are as previously defined.

observer	1	2	3	rescan
el	7.5 ± 1.3	8.1 ± 3.8	7 .6 ± 1.4	-7.5 ± 12.7
pla	1.9 ± 1.6	2.2 ± 1.2	-0.9 ± 1.5	-1.5 ± 1.5
s.tet	1.7 ± 1.3	2.1 ± 0.9	-1.4 ± 1.5	-1.4 ± 1.5
rta	1.4 ± 1.4	1.7 ± 1.6	-2.0 ± 1.6	-2.8 ± 2.0

6.2.4 Discussion

The results show that the accuracy is of the order of 1 – 2% and probably represent the best achievable in the clinical situation. *In vivo* there will be a number of complicating factors that will increase the errors as will be discussed later on. The Fastrak receiver was slightly lower than for the average patient (by ~10 cm). However, in some cases the receiver can drop lower at the sides of the patient, therefore the results of this experiment

correspond more closely to this situation. Any errors introduced by being closer to the couch must be very small otherwise the volume measurements would have been larger (unless of course larger errors are cancelling out).

The results also suggest that acoustic propagation errors (and concomitant refraction errors) are significant. In this case if they had not been taken into account the volumes would have been over-estimated by between 4 and 4.5%.

6.3 Scanning of kidneys on four ultrasound machines

6.3.1 Introduction

This experiment was carried out to determine the accuracy of the 3D system with a variety of ultrasound machines of varying image quality. Cadavaric porcine kidneys were chosen as these were readily obtainable and are closer to the *in vivo* situation than water filled balloons.

6.3.2 Method

Cadaveric porcine kidneys were scanned using a Toshiba Tosbee RM3/SSA-240A (3.75 MHz), Hitachi EUB-415 (5 MHz), Acuson 128XP/3 (5MHz), and an Hitachi EUB-240 (3.5MHz). All of the probes used were of curvilinear design except for the Hitachi EUB-240 which had a linear array. Of the four machines used, the Acuson was the most modern and the Hitachi EUB-240 the oldest (over 10 years).

The Fastrak receiver could be placed directly onto the transducer casings of the Hitachi EUB-415 and Tosbee RM3 scanners without any noticeable interference in the results (i.e. the ROI planes were in the expected orientation). However, the receiver could not be placed directly onto the transducer case of the Acuson so a polyethylene offset rod was used (figure 6.4). (N.B. when the receiver was placed directly on the Acuson transducer case the parallel image planes were tilted by about 10^{o} away from the vertical). The receiver could be placed directly onto the transducer case of the Hitachi EUB-240, but in order to be able to fit it into the rig (figure 6.5) the displacement rod had to be used. In each case, the vectors were oriented as in figure 6.4 and were aligned by eye and the lengths of $\mathbf{v_1}$ and $\mathbf{v_2}$ measured using a ruler.

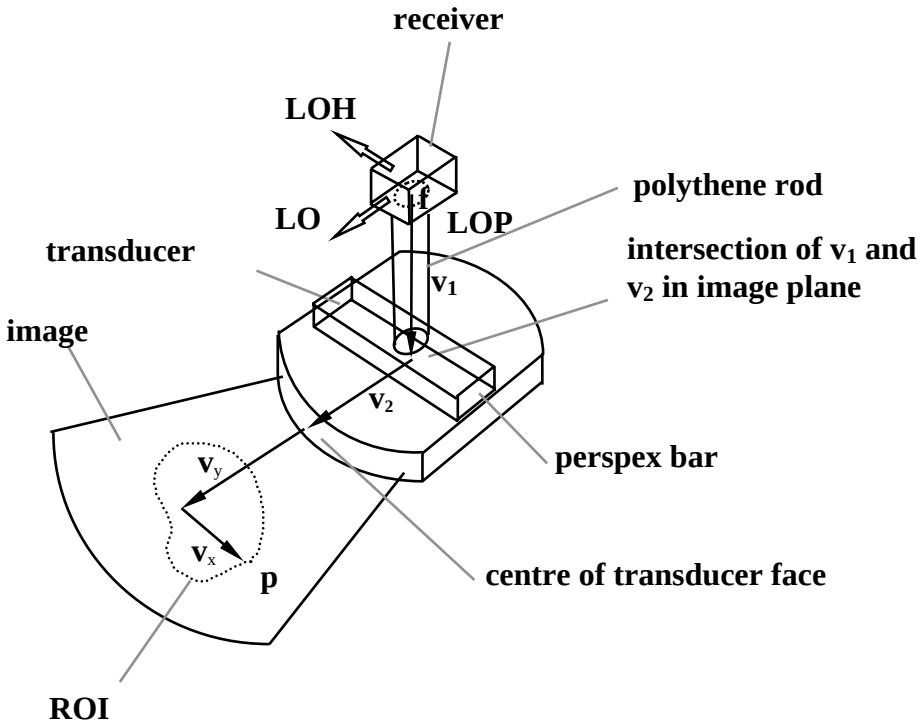

Figure 6.4 Schematic diagram of the attachment of the Polhemus receiver to the ultrasound probes.

The porcine kidneys (obtained from a local supermarket) were placed on a Perspex column in a Perspex tank (figure 6.5) filled with 26 litres of normal saline (0.9% NaCl solution). Normal saline was used in an attempt to reduce osmotic volume changes. The ultrasound transducer was placed in a gantry running across the top of the tank and moved by hand in order to acquire images oriented radially, parallel and slanted at 30^0 to the vertical (figure 6.6). The ultrasound transducer was stationary during image acquisition. About 5 minutes were required to scan each kidney using the three techniques.

The same set of 10 kidneys were scanned on the Acuson and Hitachi EUB-240; two different sets of 10 were scanned on the other two machines. (N.B. the kidneys had to be thrown away at the end of the day, therefore scan time was limited).

Immediately after scanning, each kidney was placed in a 2000 ml graduated cylinder to measure the volume of water displaced. The velocity of sound in the kidneys was assumed to be 1540 m/s within the kidneys, and errors in the path lengths of the A scan

lines caused by differences between the velocity of sound in water and tissue were ignored.

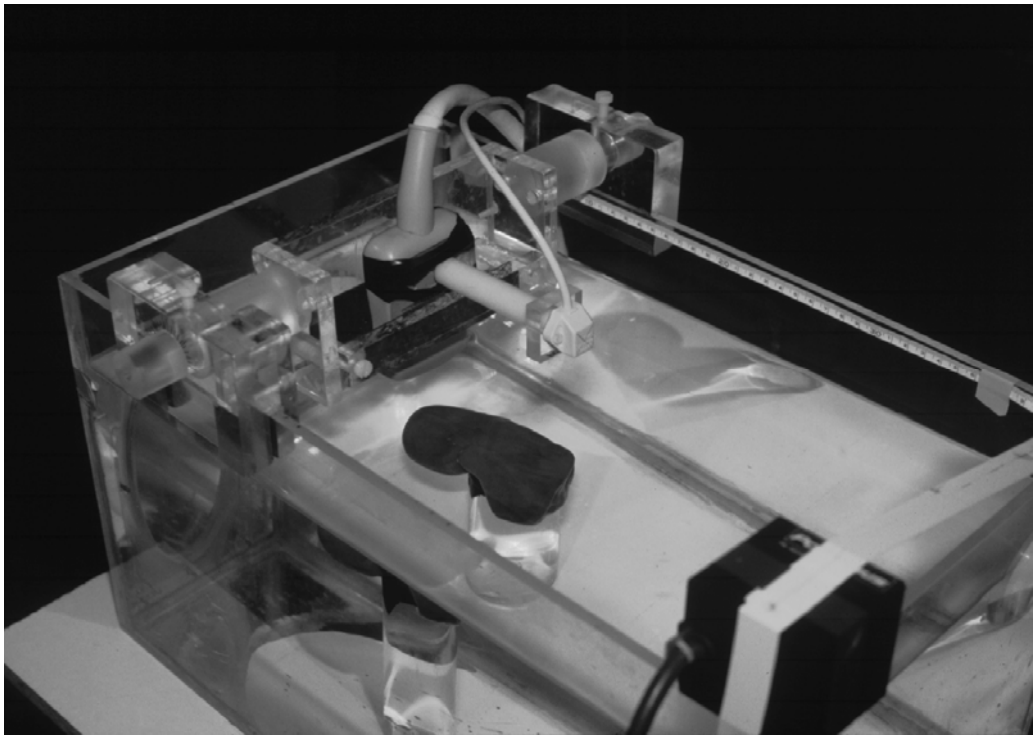

Figure 6.5 Kidney on a Perspex plinth within the scanning tank. The Polhemus receiver can be seen attached to the ultrasound probe by a plastic rod. The transmitter is on the bottom right of the picture.

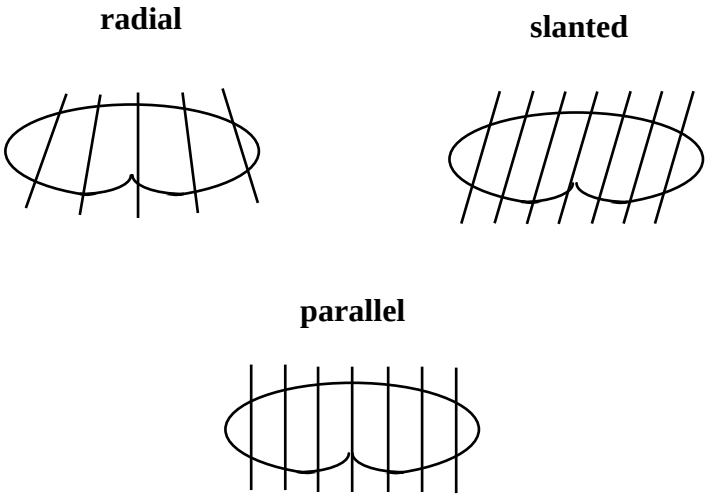

Figure 6.6 Three scanning techniques, radial, parallel and slanted were chosen to simulate how an organ might be scanned *in vivo*.

The accuracy of the water displacement (level) technique for measuring volume using the 20000 ml graduated cylinder was assessed by measuring the volume of five accurately machined (± 0.01 cm) Perspex blocks (30 - 260 ml). The accuracy (mean ± SD) was -1.3 ± 2.0 ml (-0.9 ± 1.8%).

The Fastrak transmitter was placed on a corner of the tank. The receiver was always within 0.5 m of the transmitter. Between 15 and 20 (328 x 228 matrix, 7 bit resolution) images were acquired on each run. The image files were temporarily stored on the hard disc of the PC in the Microsoft Windows device independent bitmap (BMP) format.

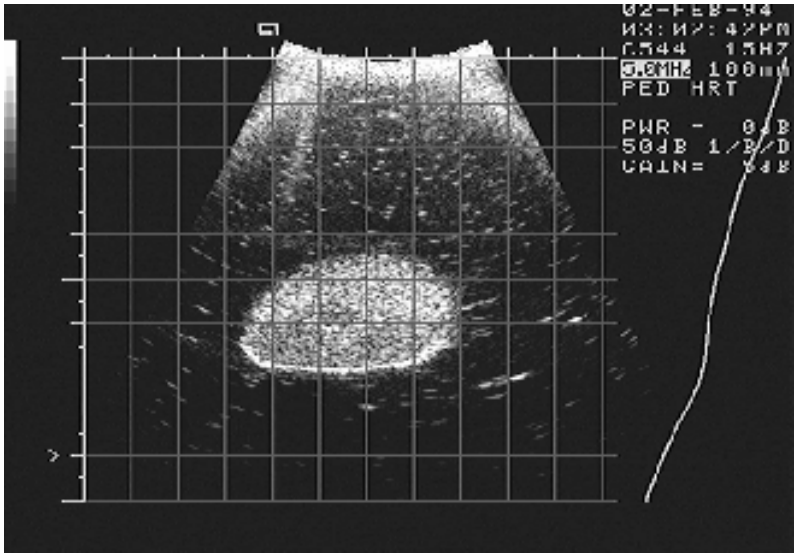

Figure 6.7 Acuson kidney image.

After each scanning session, the image (figure 6.7) and position files were transferred via a local network to a Titan graphics supercomputer (Kubota Pacific Inc, Santa Clara, CA, USA) for analysis. The edges of each kidney were outlined using a mouse, and the ROI points transformed into the Fastrak coordinates (figure 6.8) as described in chapter 2. Each sequence of images took about 10 minutes to outline. The ROIs were processed as for the balloons.

(a)

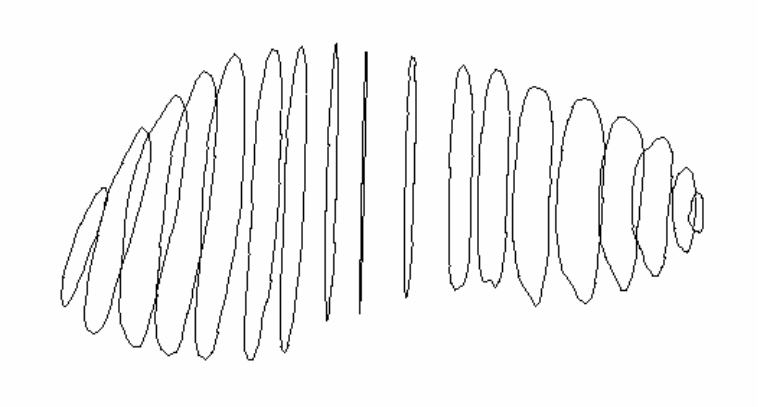

(b)

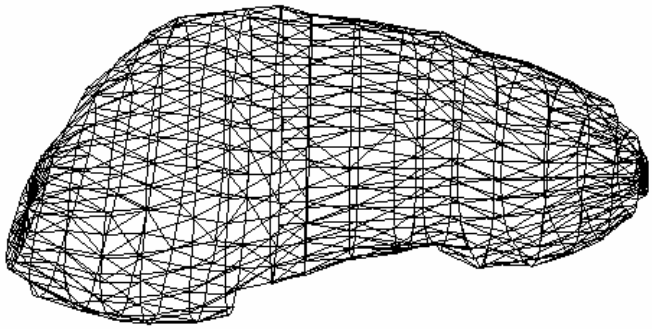

(c)

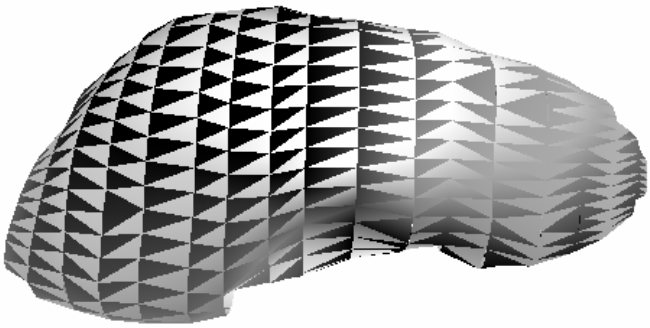

Figure 6.8 (a) Transformed kidney ROIs, (b) triangle mesh, and (c) surface rendering.

6.3.3 Results

As there are so many permutations of the results only a few combinations are presented here to exemplify the overall results. The Tosbee (commonly used in obstetrics) was chosen to compare the four methods of calculating volume using radial scans, and the tetrahedral method were used to compare the three scan techniques. The radial tetrahedral volumes were used to compare machines.

Figure 6.9 shows the results for the Tosbee machine for the four methods of calculating volume with radial scans. In figure 6.9(a) the planimetry, tetrahedral and ray volumes all lie fairly close to the line of identity. The ellipsoid method has the greatest variance and appears to underestimate volume. This is borne out by figure 6.9(b) which shows the actual differences between the measured and calculated volumes. There appears to be little difference between the limits of agreement for the planimetry, tetrahedral and ray volumes.

As there is little difference between the planimetry, tetrahedral and ray volumes, the tetrahedral method can be taken as representative of the other two methods. Figure 6.10(a) shows the variation in tetrahedral volume with scan technique for the Tosbee. Figure 6.10(b) shows that the mean differences are fairly close together and the limits of agreement are similar in extent. All of the scan techniques result in slight overestimation of volume on average.

Figure 6.11 shows the radial tetrahedral results for all the machines. As there appears to be little difference between the scan techniques, the radial technique can be taken as representative of the other two and so used to compare machines. Figure 6.11(a) shows that there is little to choose between the machines. The Bland-Altman plot in figure 6.11(b) shows that the limits of agreement are fairly similar although the limits of agreement for the Acuson and Tosbee are slightly narrower than for the two Hitachi machines. The Acuson has the largest mean difference.

(a)

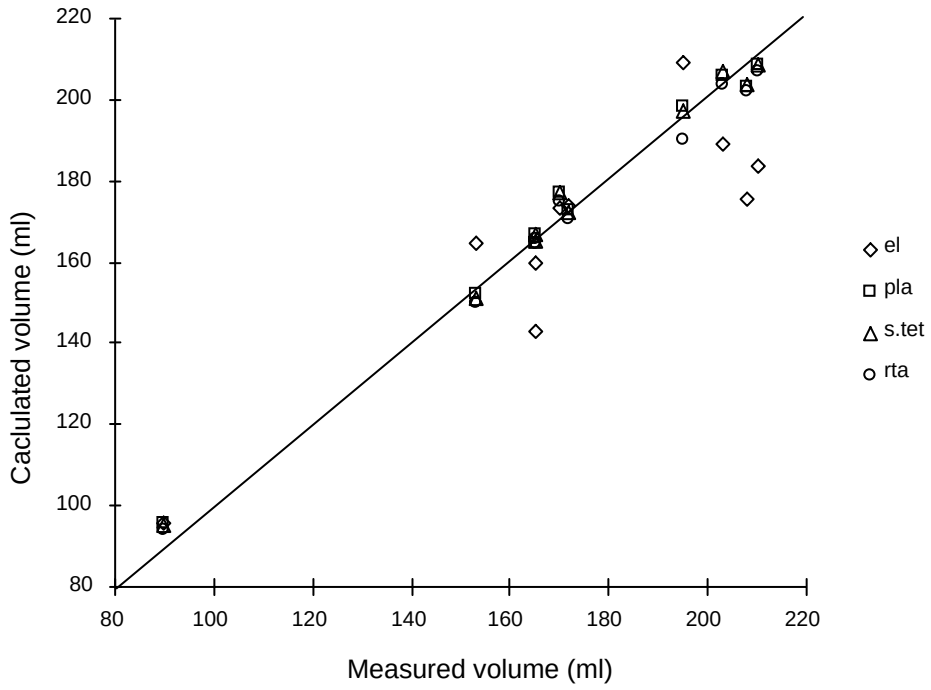

(b)

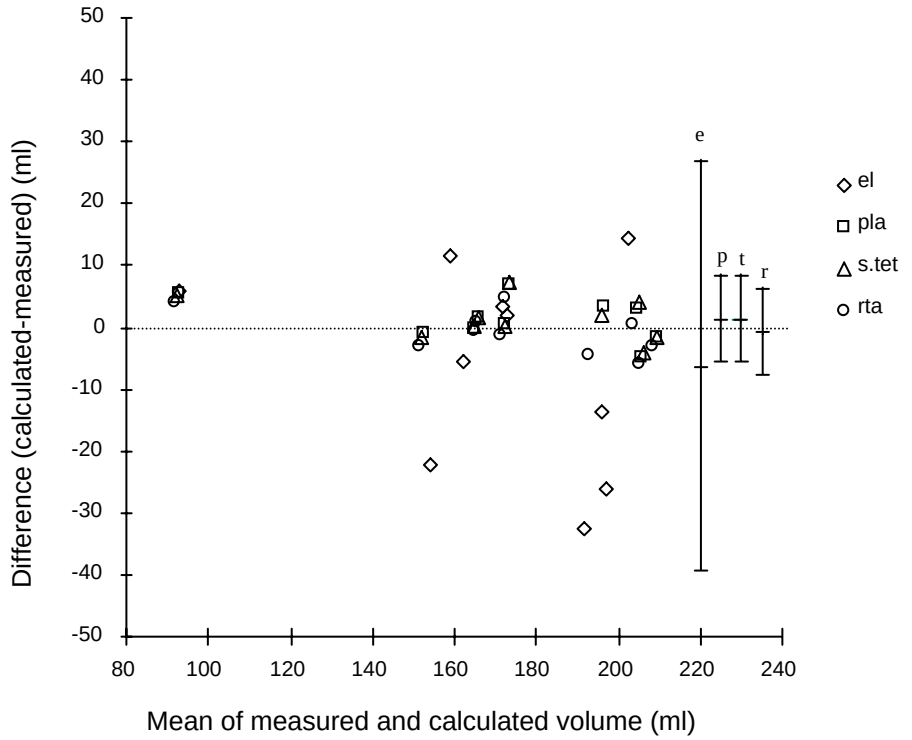

Figure 6.9 (a) Radially scanned Tosbee kidney volumes calculated using the ellipsoid (el), planimetry (pla), tetrahedral (tet) and ray tracing (ray) methods, (a) measured versus calculated volumes. The line of identity is shown. (b) Bland-Altman plot of the same data as in (a).

(a)

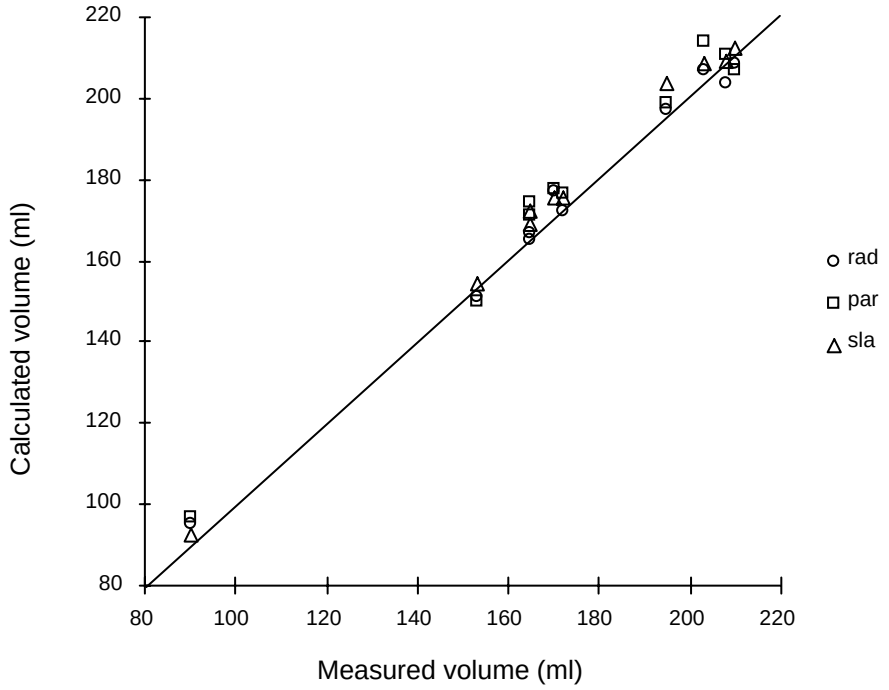

(b)

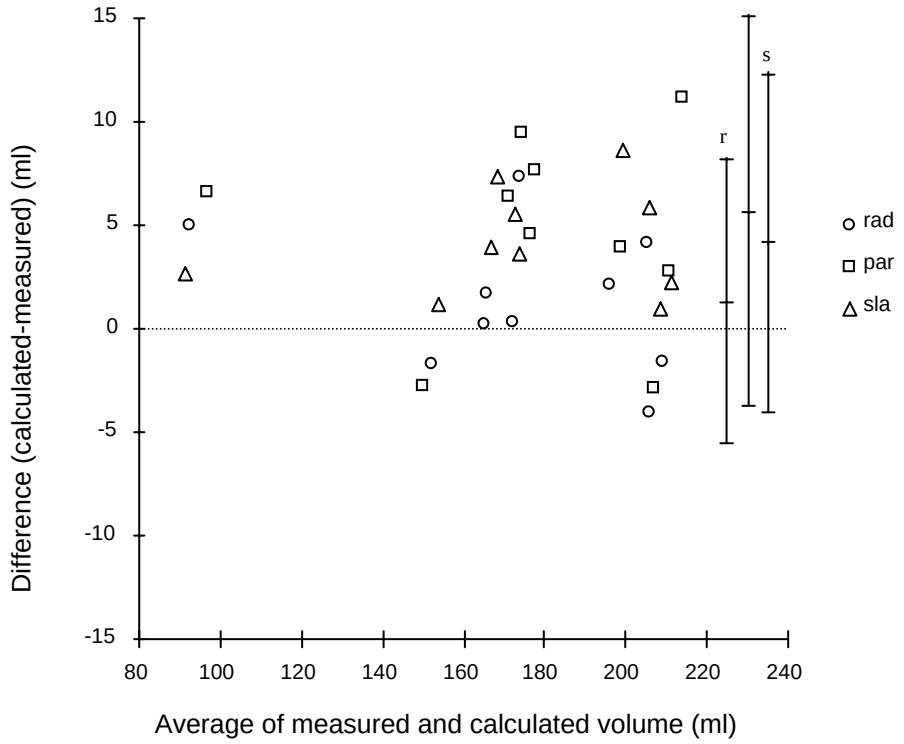

Figure 6.10 Comparison of the Tosbee kidney tetrahedral volumes for radial (rad), parallel (par) and slanted (sla) scans, (a) and (b) as for figure 6.9.

(a)

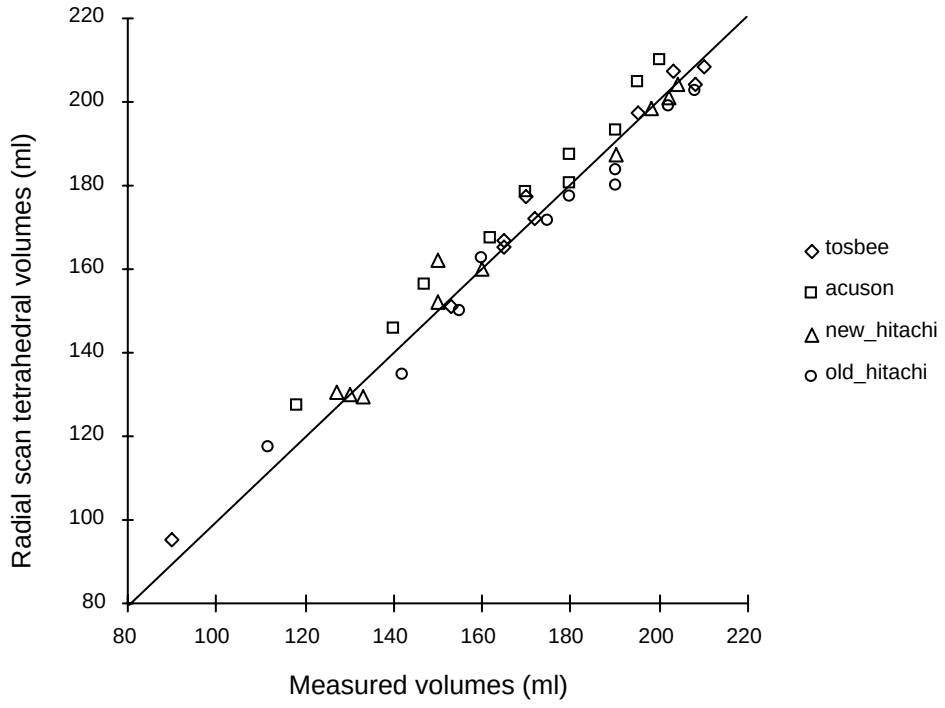

(b)

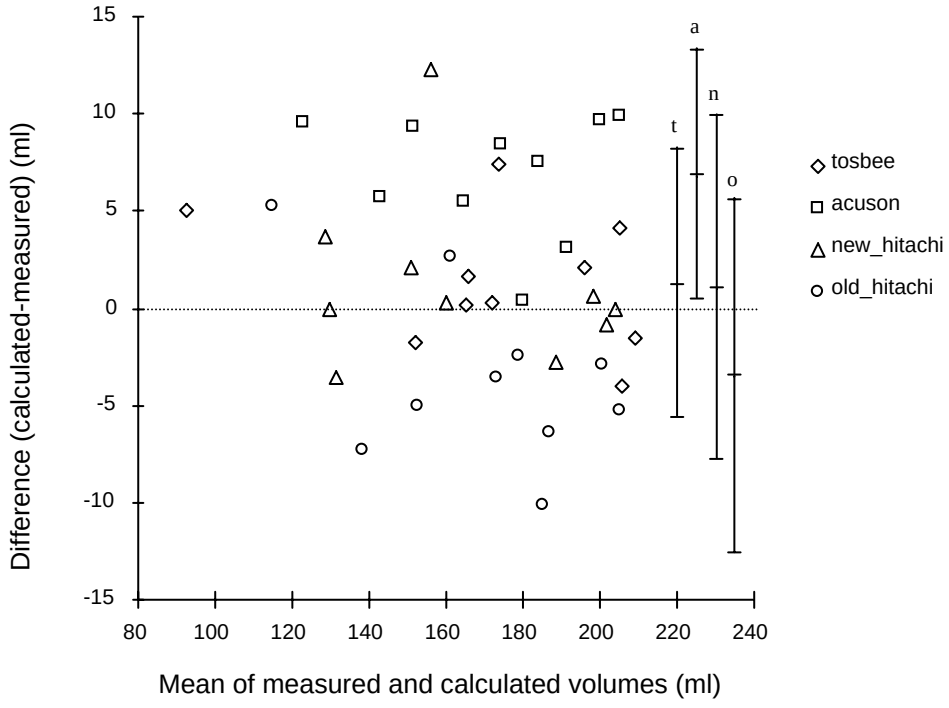

Figure 6.11 Radial scan tetrahedral volumes for the four ultrasound machines, (a) and (b) as for figure 6.10.

Table 6.4 The mean and standard deviation of the percentage error for all four machines for the radial scans.

	el	pla	tet	rta
Acuson 128XP	5.3 ± 10.6	5.9 ± 2.1	4.3 ± 2.2	2.7 ± 2.3
Hitachi EUB-415	-8.9 ± 2.4	0.7 ± 1.9	0.8 ± 2.2	0.2 ± 2.3
Tosbee RM3	-2.7 ± 9.0	1.1 ± 2.5	1.0 ± 2.4	-0.1 ± 2.3
Hitachi EUB-240	-9.9 ± 6.9	-0.4 ± 3.5	-1.8 ± 3.0	3.0 ± 2.7

Table 6.4 shows the mean and standard deviation of the percentage error for the four volume calculation methods for radial scans for all machines. Note that the standard deviations of all the volume calculation methods are very similar within and between machines, the only exception being the standard deviation for the Hitachi EUB-415 radial ellipsoid volumes which is comparable to the 3D methods.

Table 6.5 The mean and standard deviation of the slice separation and the distance between outline points for the kidneys scanned on the Tosbee machine.

	slice separation (mm)	point separation (mm)
radial	7.6 ± 2.3	5.3 ± 2.8
parallel	7.0 ± 2.1	5.0 ± 2.6
slanted	7.6 ± 2.5	5.1 ± 2.7

All kidneys appeared to be scanned consistently with little difference in the mean distance between ROI points and mean separation between image planes (table 6.5).

6.3.4 Discussion

The results show that the system produces acceptable results for a variety of ultrasound machines, scan techniques and volume estimation algorithms. The 3D volume algorithms (planimetry, tetrahedral and ray) have a significantly lower variance than the ellipsoid method (an SD of ~ 3% compared to ~10%) except for the Hitachi EUB-415.

The fact that there is no significant differences between scan techniques also indicates that osmotic volume changes were not significant. The kidneys were scanned over a period of about five minutes with the radial scans being acquired first followed by the parallel and slanted sequences. If there were a significant effect then this should have been reflected in an increase in volume especially between the radial and slanted scans.

Several factors influence the overall error, for instance image and scanner resolution, tracing error, number of slices through the object, number of ROI points, variation in acoustic propagation velocity and refractive index, calibration, errors in measuring the position and orientation of the Polhemus receiver relative to the transducer, etc. The small, but insignificant, differences seen between the variances of the scanning techniques and volume calculation methods may be due to a combination of the water displacement, rescan and retracing errors.

The mean percentage error reflects the overall systematic error for each machine. The large number of factors that influence the overall error probably explains the differences between the mean percentage errors. The Acuson had a greater systematic error than the other machines, which could be due to a number of reasons (alignment of the receiver etc.). The variance is the most important value as this indicates the degree of confidence that can be attached to any particular measurement.

All the machines performed more or less equally well in spite of marked differences in image quality. However, differences in image quality are likely to be important when scanning organs *in vivo* - on the assumption that the edge of an organ can be seen more easily and therefore outlined more easily on a higher quality image.

This experiment is limited in other ways, for instance, the transducers were held in a gantry and were stationary during image capture, rather than being hand held and moving. However, as the receiver position and orientation data is acquired very fast (4 ms), and the transducer generally moves slowly (a few cm per second), image registration errors caused by the time delay between the acquisition of the pose data and image capture will be very small. Another limitation of this work is that only one observer was used to acquire the data and outline ROIs. However, this work gives an indication of the

minimum error obtainable. *In vivo* errors are likely to be larger due to the differences outlined above.

The results are comparable to the results of others, for instance Gilja *et al* (1994) measured pigs kidneys to an accuracy of 6.5 ±2.9% (3.25 MHz), 9.8 ± 3.1% (5 MHz) and a fluid filled pigs stomach to an accuracy of 0.4 ± 6.9% (3.25 MHz). The system could perhaps be useful in diagnosing early rejection of transplanted kidneys and monitoring a decrease in volume associated with effective therapy, as suggested by Absy et al. (1987).

6.4 Scanning of fetal livers with ultrasound, CT and MR

6.4.1 Introduction

MRI has been used to estimate fetal liver, lung and brain volume in fetuses in the third trimester (Mansfield *et al*, 1990, Stehling *et al* 1990, Roberts *et al* 1994, Baker *et al* 1994, 1995). CT is used for measuring organ and tumour volumes in adults. Therefore it is interesting to see how 3D-US compares with MR and CT. Cadaveric fetal livers were chosen for this experiment, (mainly because the 3D-US system was initially intended for measuring fetal liver volumes *in utero*).

6.4.2 Method

Sixteen cadaveric fetal livers (8 - 38 ml) were placed on a Perspex plinth in a tank of distilled water. The livers had intact capsules and were fixed in 10% formalin saline. As the livers were denser than water they could be held in place under their own weight. An Acuson 128XP/3 ultrasound scanner (Acuson Corp., Mountain View, CA, USA) with a 5MHz curvilinear transducer was used to scan the livers. The transducer was held in a gantry running across the top of the tank and between 15 and 20 images, oriented radially, parallel and slanted at 30^{o} to the vertical, were taken through each liver (figure 6.6). The Fastrak receiver was attached to the US transducer as shown in figure 6.4.

A 328 x 228 image matrix was used with a pixel size of 0.2 x 0.2 mm and 7 bit resolution (pixel range 0-255 in steps of 2). For the parallel scans, the mean slice separation was around 3 mm (calculated retrospectively). This is comparable to the actual slice thickness in the focal region - estimated at between 3 and 6 mm for a similar machine (Acuson

128XP/10) using the Cardiff resolution test object (Gammex-RMI Ltd, Nottingham, UK) as described in chapter 7. After acquisition, the images (figure 6.12) were transferred from the PC to a Titan graphics supercomputer (Kubota Pacific Inc, Santa Clara, CA, USA) via a local area network (LAN). The edges of the livers were outlined on the computer monitor using a mouse, and the ROI (region-of-interest) points connected into a triangle mesh (figure 6.13) as for the kidneys and balloons.

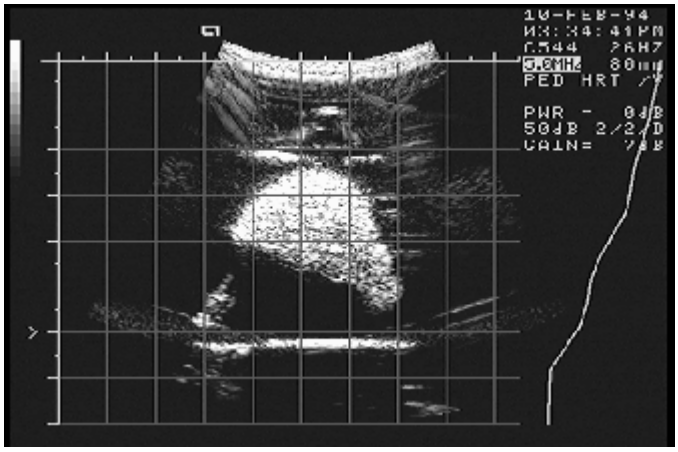

Figure 6.12 Acuson image of a cadavaric fetal liver.

The actual volume of the livers was measured by water displacement. The accuracy and precision (mean error ± SD) of the displacement technique was assessed by measuring the volume of seven accurately machined Perspex rods (3 - 73 ml) and was found to be 0.86 ± 0.65 ml (7.8 ± 9.8%).

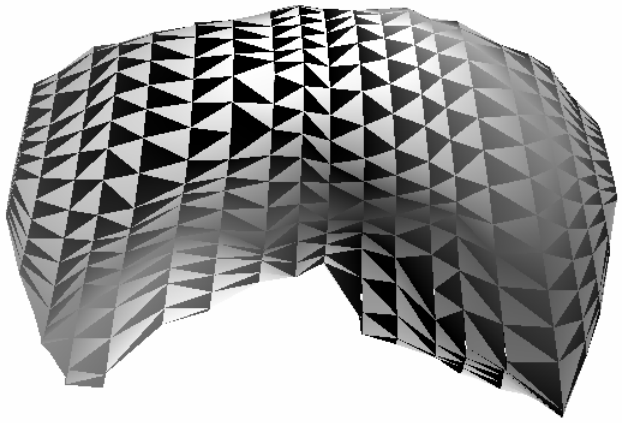

Figure 6.13 Surface rendering of a cadavaric fetal liver reconstructed from multiplanar ROIs.

Twelve of the 16 livers were placed on a Perspex sheet and scanned on a Siemens Somaton DRH CT scanner (Siemens AG, Erlangen, Germany). A slice thickness and separation of 2mm was used with a pixel size of 0.5 x 0.5 mm. Fifty five slices were acquired in total. The 12 livers that were also scanned on a Siemens Impact Magneton MR scanner (1 Tesla magnet and 15 mTesla gradient) as a 256 x 256 x 128 volume with pixel size of 0.97 x 0.97 x 1.25 mm (slice separation). Only 12 of the 16 livers were MR scanned due to limitations in fitting all the livers into the scan field at the same time, (only one scan session was available). The same 12 livers were also CT scanned, but of these only 11 could be analysed as one liver fell partially outside the field of view.

The CT and MR images were transferred to the Titan computer and the edges outlined using a mouse. Two sets of outlines were produced. One set followed the visible edge of the liver as closely as possible (for the planimetry volumes), and the other was traced a little way out to include all liver pixels not visible in the standard grey-level window. A display window was chosen with a central value close to the mean CT or MR pixel value of the livers, with a width sufficient to display most of the pixels. For example, for CT, the mean pixel value was about 1070 ± 6 and the display window 1000 ± 400.

The CT and MR planimetry volumes were calculated by multiplying the area of each ROI by the scan thickness and summing over the whole volume. For voxel counting, a threshold value midway between the average value of the background pixels and the average value of the object pixels was used, as suggested by Kennedy (1989). Software was developed for counting the number of pixels above a given threshold value within a ROI. The volume of the livers was calculated by multiplying the total voxel count by the voxel volume (0.97 mm^3 for MR and 0.5 mm^3 for CT).

6.4.3 Results

All four of the ultrasound volume algorithms produced values close to the line of identity (figure 6.14 (a)), but tended to slightly over-estimate volume (figure 6.14 (b)). The 95% limits of agreement are about twice as wide for the ellipsoid method, although the ellipsoid method has the smallest mean error. Table 6.6 shows the mean and standard deviation of the percentage error for the four volume algorithms and three scan techniques.

Table 6.6 Mean and standard deviation of the absolute (ml) and percentage error for the four volume estimation algorithms for each ultrasound scan technique on the 16 livers.

	radial		parallel		slanted	
	abs. error	% error	abs. error	% error	abs. error	% error
el	0.5 ± 2.0	2.9 ± 8.7	0.4 ± 1.9	1.8 ± 7.6	-0.4 ± 1.8	-1.5 ± 7.2
pla	1.2 ± 0.8	6.5 ± 5.2	0.9 ± 0.9	4.5 ± 4.5	-0.5 ± 1.0	-2.5 ± 5.9
tet	1.5 ± 1.1	7.7 ± 5.4	1.7 ± 1.3	8.6 ± 5.6	0.0 ± 1.5	0.2 ± 6.6
rta	1.0 ± 0.8	5.3 ± 4.7	0.9 ± 0.9	4.7 ± 4.4	-0.7 ± 1.0	-3.1 ± 5.6

The radial and parallel scan techniques are very similar with much the same mean difference and limits of agreement (figure 6.15). However, the slanted scans tended to underestimate volume with slightly wider limits of agreement compared to the other two methods (figure 6.15 (b)).

Table 6.7 Mean and standard deviation of the absolute (ml) and percentage error for voxel count and planimetry volumes for 11 CT and 12 MR livers.

Modality	Method	absolute error	% error
CT	voxel counting	-0.3 ± 1.4	-0.0 ± 9.7
MR	"	-0.7 ± 1.4	-3.1 ± 9.6
CT	planimetry	-3.6 ± 2.1	-18.9 ± 8.7
MR	"	-2.9 ± 1.8	-15.7 ± 8.6

The accuracy of the US radial RTA volumes is lower than for CT and MR voxel count volumes, although the variance is slightly smaller (figure 6.16(b)). The CT and MR volumes have a very similar mean difference and limits of agreement. Table 6.7 shows the mean and standard deviation of the percentage errors for the CT and MR voxel count and planimetry volumes. The variances of the MR and CT volumes are very similar. The MR and CT planimetry volumes on average significantly underestimate volume.

(a)

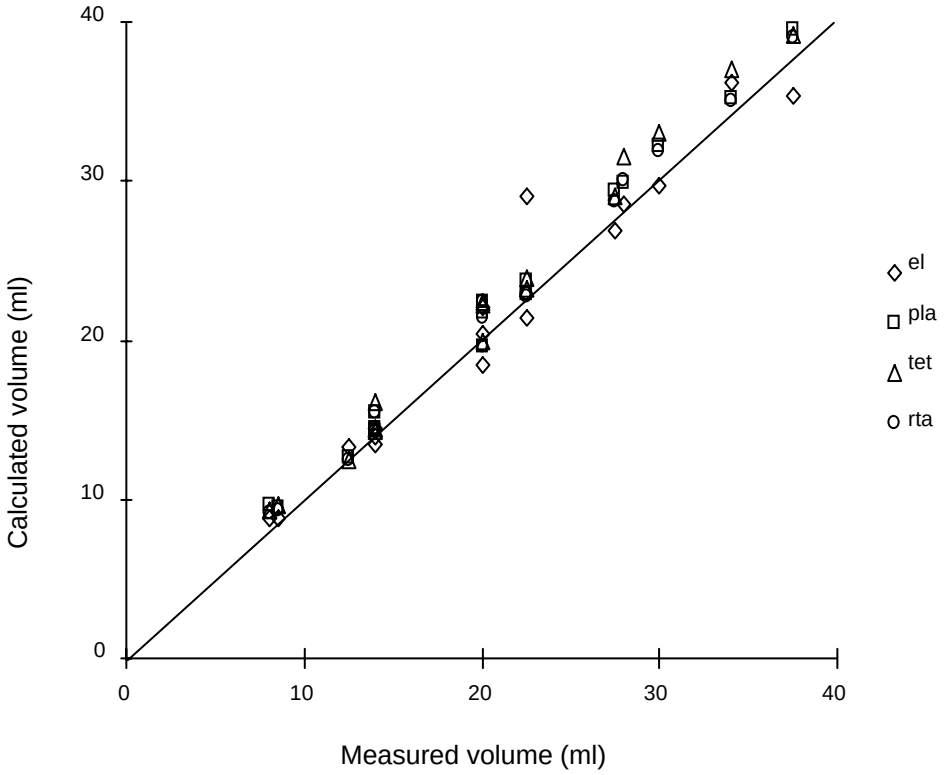

(b)

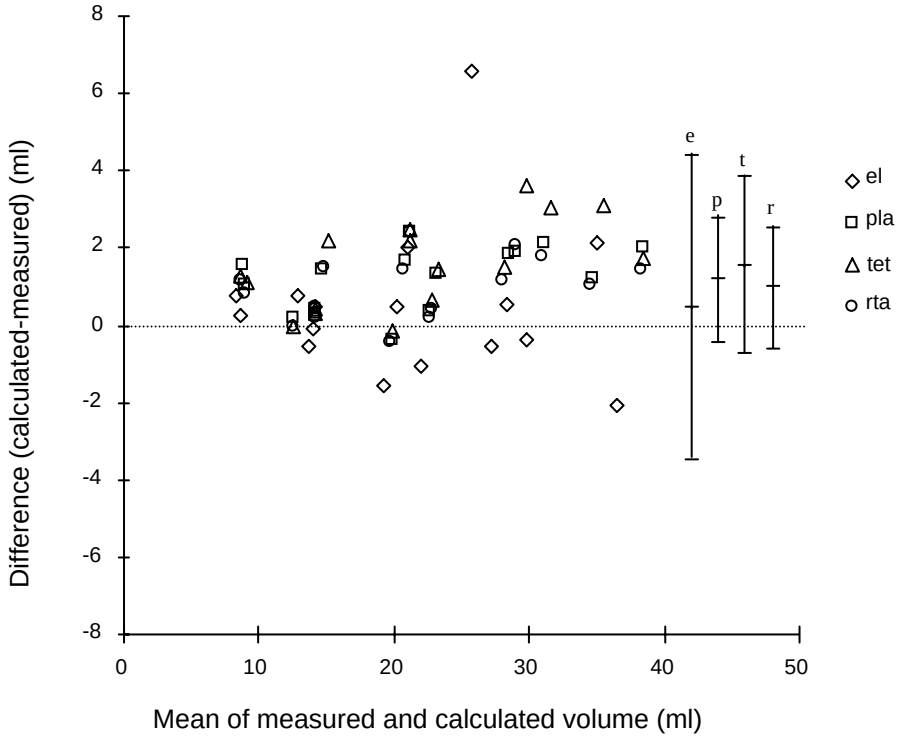

Figure 6.14 (a) Calculated ellipsoid (el), planimetry (pla), tetrahedral (tet), ray trace (rta) volumes versus measured volume (by water displacement) for radial US liver scans. The line of identity is shown. (b) Bland-Altman plot of the same data as in (a).

(a)

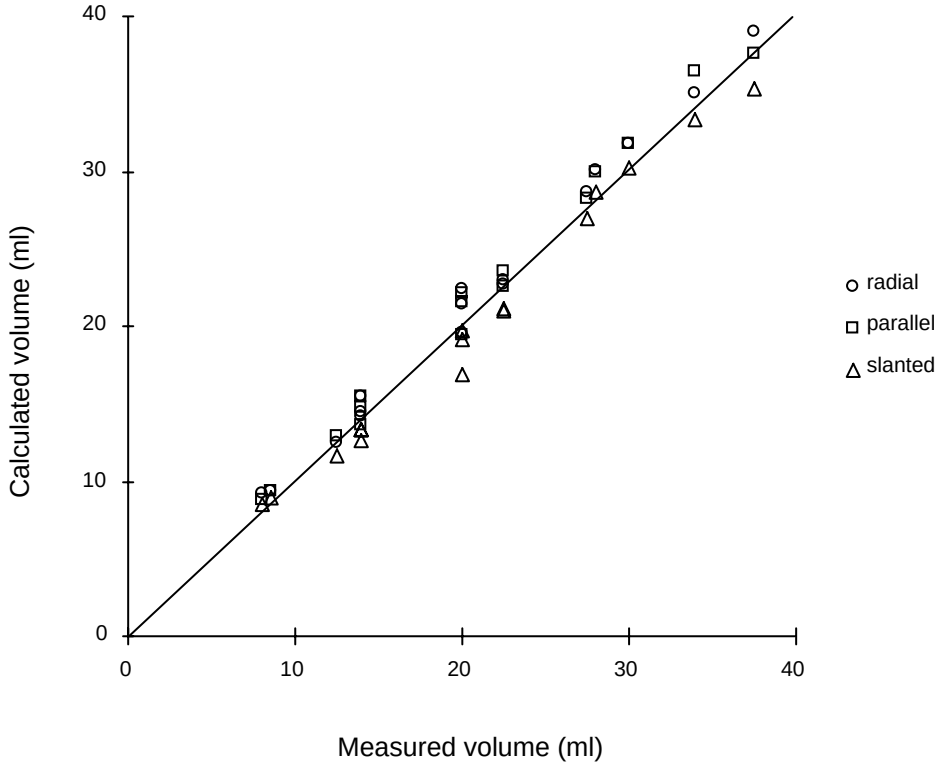

(b)

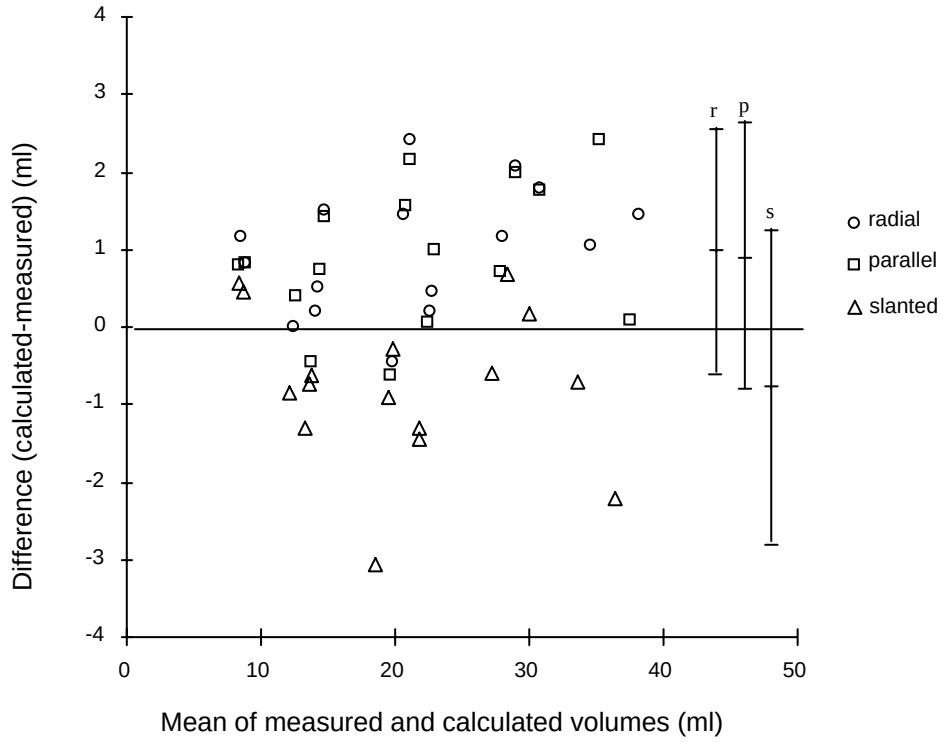

Figure 6.15 (a) Plot of the ray trace volumes versus scan technique. The line of identity is shown. (b) Bland-Altaman plot. Each limit of agreement is designated by the first letter of the scan technique.

(a)

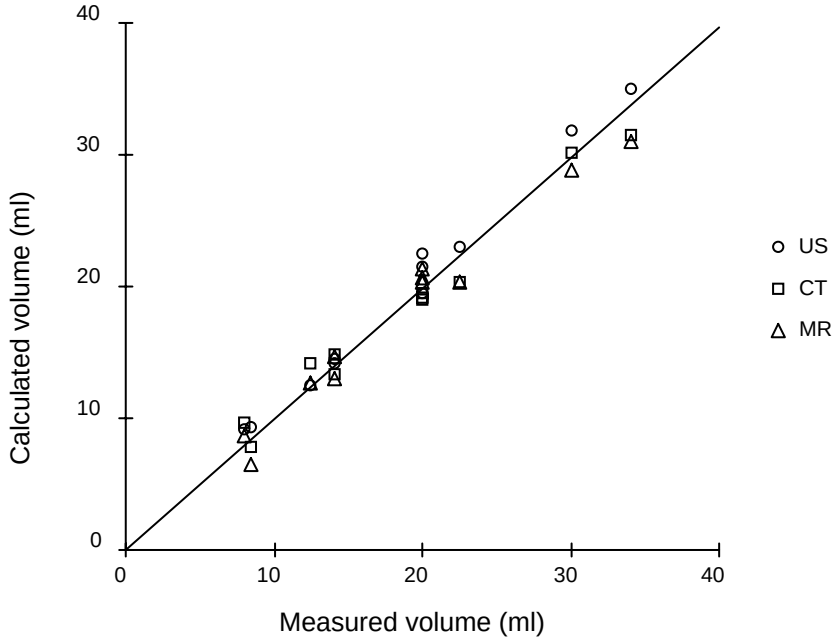

(b)

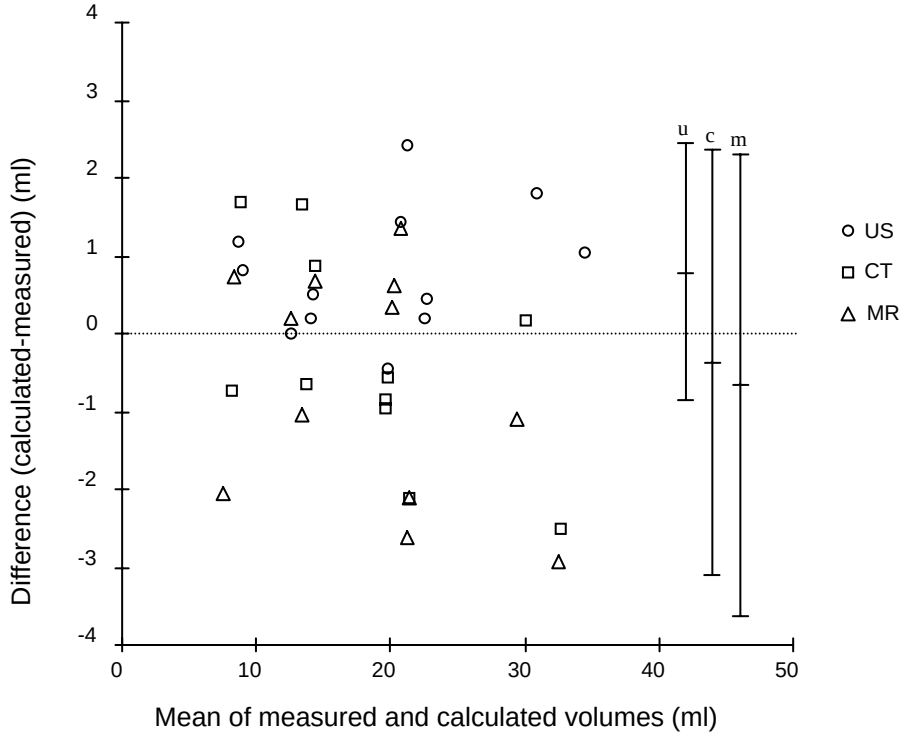

Figure 6.16 (a) US radial ray volumes and CT and MR voxel count volumes versus displacement volume. (b) Bland-Altman plot of the same data.

6.4.4 Discussion

The results show that under ideal conditions of scanning fetal livers against a high contrast uniformly low-level background, the accuracy of the 3D US system is lower than CT and MR, although the variance is significantly smaller ($p < 0.01$). This is corroborated by Gopal *et al* (1992) who obtained an *in vitro* SD of 2.27% for US and 8.01% for MR. It is interesting to note that the precision of CT and MR are very similar even although the MR voxels (0.97 mm^3) are about twice the volume of the CT voxels (0.5 mm^3). In comparison, the US voxels are about 0.12 mm^3 (0.2 x 0.2 x 3mm) in volume, which may account for the slightly smaller US variance.

The MR and CT results could perhaps be improved by increasing the image resolution. However, it should be born in mind that CT and MR tend to be used to acquire a section through the whole body rather than a limited region, requiring a lower resolution and therefore a larger pixel size. For ultrasound, the physical field of view tends to be smaller than that for CT or MR, therefore images are of higher resolution. In general, the overall accuracy will be mostly dependent on the ratio between the pixel and object dimensions and on slice thickness and separation.

A number of other factors influence the overall error, for example a difference between the velocity of sound in the fetal livers and the assumed value for soft tissue (1540 ms^{-1}) will result in distance and refraction errors. Propagation velocity is a function of temperature and the fixing process (Bamber and Hill, 1979). At ~ 22^o C, the temperature that out experiments were conducted, the data of Bamber and Hill suggests a propagation velocity of about 1590 ms^{-1} in fresh fetal livers which would lead to a 3.2% *under-estimate* of volume.

According to Bamber and Hill, formalin fixation results in a *decrease* in propagation velocity of the order of 1% which would result in an *over-estimate* of volume of 1%. No data on the propagation velocity in fresh and fixed human fetal livers are reported in the literature, and so more work in this area would be useful. However, the figures quoted above suggest that the effects of temperature and fixation are likely to be small and tend to cancel at temperatures below body temperature. Errors in delineating the margins of the liver are likely to be greater.

The results show that the planimetry, tetrahedral and ray volume estimation algorithms are equally as good, although perhaps as expected, the variance of the ellipsoid method is greater than the other three methods. There is little difference between scan techniques, although the slanted scans have greater variance and on average tend to underestimate volume. This may be due to blurring of the edge at shallower incident angles, leading to increased uncertainty in the true position of the edge.

The CT and MR planimetry volumes significantly overestimate volume because the edge spread function has the effect of extending margins beyond their true position. Hence volume measurements are dependent on window settings (Koehler *et al* 1979, Baxter and Sorenson 1979, Harris *et al* 1993). The CT and MR planimetry results demonstrate that the optimal window for viewing is not usually appropriate for measuring volume.

Although this *in vitro* study demonstrates that US volume measurements are comparable in accuracy to MR and CT, more work needs to be done on assessing *in vivo* errors. Tissue layers interposed between the transducer and organ of interest are known to produce significant image distortion due to velocity and refraction errors. In some cases, these distortions may need removing before accurate *in vivo* volume measurements can be carried out, for example, by the technique proposed by Carpenter *et al*, (1995). However, the biggest difference in moving from *in vitro* to *in vivo* will be that the surrounding background will no longer be uniformly low level and so the margin of the fetal liver will not be so clearly defined with such high contrast. This will result in greater variability in the apparent position of the edge.

6.5 Summary

The results show that the system is capable of measuring *in vitro* volume to an accuracy and precision of under 5%. In vivo errors are likely to be greater than this, for reasons, which are given in subsequent sections. Therefore, these results represent a lower limit for *in vivo* volume measurements. There is no significant difference between the three scan techniques or 3D volume algorithms. Figure 6.17 (a) shows a scatter plot of balloon, liver, kidney CAN volumes versus displacement volume. Figure 6.17 (b) is a Bland-Altman plot of the same data.

(a)

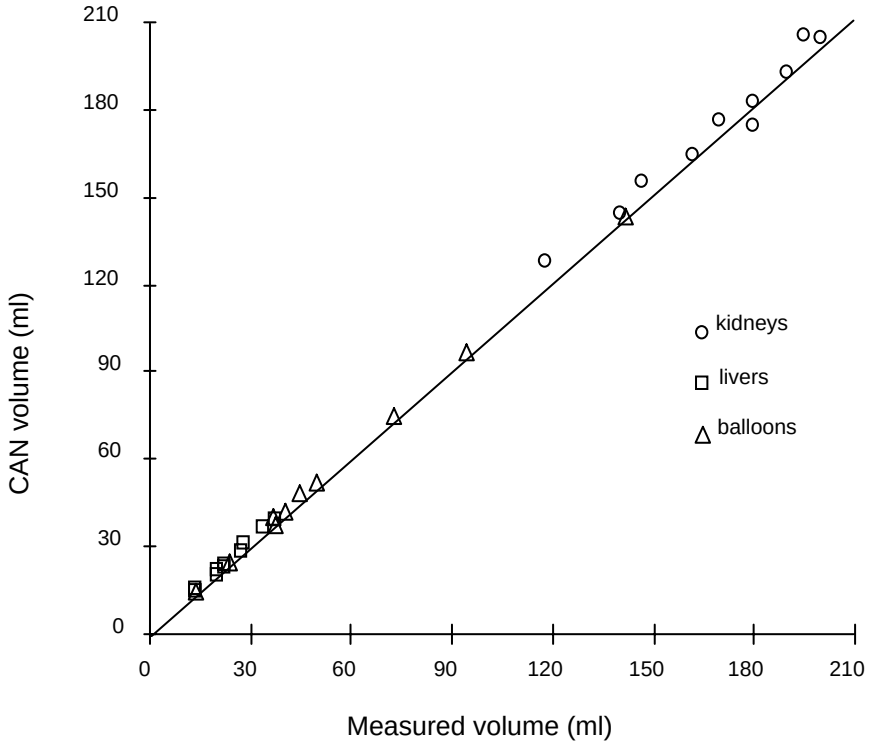

(b)

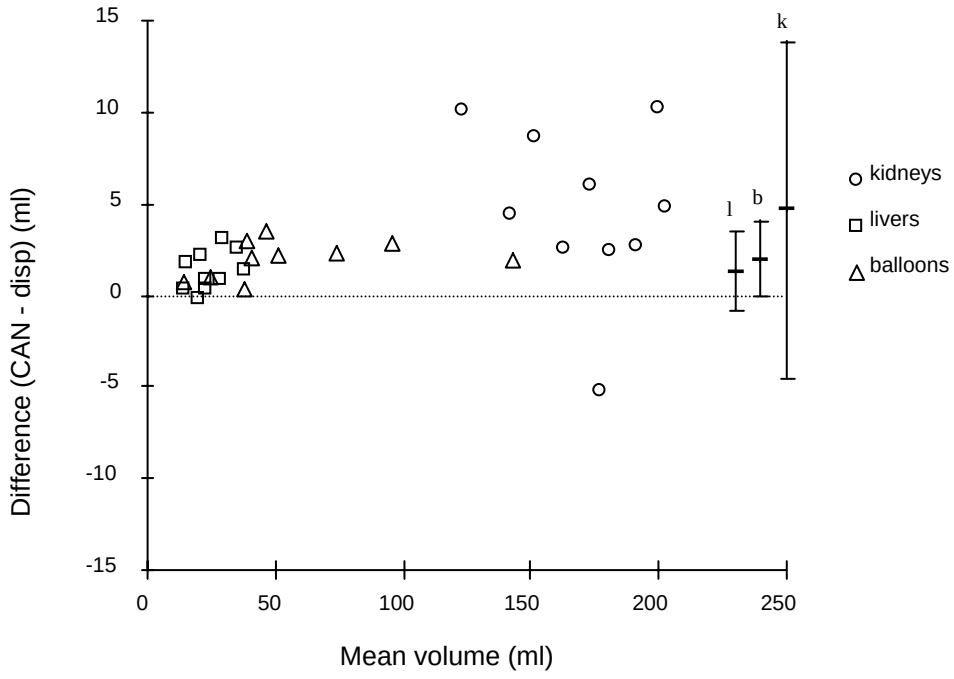

Figure 6.17 (a) Plot of balloon, liver and kidney CAN volumes versus water displacement (level) method. (b) Bland-Altman plot of the same data.

CHAPTER 7

Errors

7.1 Introduction

It was not the purpose of this project to exhaustively investigate all possible sources of error, but rather to gain some idea of the overall accuracy of the 3D system. However, it is possible to make general comments about errors. This chapter briefly discusses some of the factors that influence the accuracy of measuring volume using 3D ultrasound. For the purposes of this chapter, errors can be divided into objective and subjective errors. Or, to put it another way - machine errors and people errors. Objective errors are easier to quantify than subjective errors.

Subjective errors

1. Ability of an observer to draw a ROIs.
2. Organ movement.

Objective errors

1. Image resolution - i.e. the ratio of organ to pixel size.
2. Ratio of ROI point separation to ROI circumference.
3. Number of image planes sampling the organ.
4. Refraction and velocity errors.
5. Translation and rotation of ROIs due to Fastrak mis-alignment and signal perturbation.
6. Large scale vertical and horizontal accuracy of the ultrasound scanner.
7. Water displacement measurement of actual volume.

7.2 Subjective errors

7.21. Ability of an observer to draw ROIs

This can be divided up into two parts (a) basic proficiency in using a mouse or drawing device and (b) training in recognising the structure of interest. Point (a) can be

accomplished in a few weeks whereas (b) may take years. Table 6.3 shows that inter and intra-observer errors in measuring balloon volumes are of the order of 1 to 2%.

By far the largest error is likely to be associated with observer perception of a structure boundary in an ultrasound image. There are a number of physical reasons why this is so. For example, refraction errors result in displacement of structure boundaries (as discussed further in subsequent sections), and can produce shadowing effects. Also, if the border of a structure is nearly parallel to the ultrasound beam there is very little specular reflection. In some cases this can result in complete fade out of the edge, forcing the observer to make an intelligent guess as to the true position of the border. This error is difficult to quantify, but from personal experience, is probably 10% or greater in some cases.

7.2.2 Organ movement

This is a difficult problem to deal with. Movement can be broken down into two main areas (1) phasic movements, for example cardiovascular, respiratory and (2) random movements. Random movements are a particular problem, especially with fetuses, as they cannot be told to keep still. Random movements could result in a range of errors, for example, if an organ moves in the direction of scanning during scanning, the volume will be overestimated. Conversely if the organ moves in the opposite direction during scanning the volume will be underestimated. If the organ moves sideways, i.e. roughly normal to the scan direction, the organ will be sheared but with only a small error in volume (see section 7.5). One can envisage complicated situations arising where the errors cancel out - the organ may be reconstructed wrongly but be more or less the correct volume.

7.3 Objective errors

7.3.1. Image resolution - or the ratio of organ to pixel size

The higher the resolution of the captured video image, the greater the number of pixels defining the imaged object. The greater the number of pixels, the better the definition of edges, and therefore area can be calculated more accurately. In other words, objects appear less pixellated in higher resolution images. If two image capture resolutions are available, one twice the other, the same degree of detail can be achieved if an object

appears twice the size in the lower resolution capture. Therefore the important factor is not capture resolution *per se*, but rather the ratio of organ to pixel size. The relation between pixel size and the accuracy of calculating volume is equivalent to that seen in figure 7.1, which shows the percentage error in calculating area for a given number of ROI points. In this case read pixels for ROI points.

7.3.2 Effect of the number of ROI points on error

To investigate the variation in accuracy and the number of ROI points, a small C program was written to generate the xy coordinates of points on a circle of radius 100 units (using the equation $r^2 = x^2 + y^2$). (N.B. the radius of the model circle is not critical for this test - it should just be much greater than unity). The ROI points were converted from floating point to integer to simulate ROI points input by a mouse. The area of the circle was calculated using the algorithm described in chapter 2, (effectively the area below the bottom half of the circle subtracted from the area below the top half). The error in calculating volume will be directly proportional to the error in calculating area.

Figure 7.1 shows the percentage error for between 10 and 100 ROI points. 30 points were used in the theoretical tests and up to 30 points were traced in the *in vitro* experiments. Note that the error falls to ~1% at 30 points. The error is around 1.3% for 30 points.

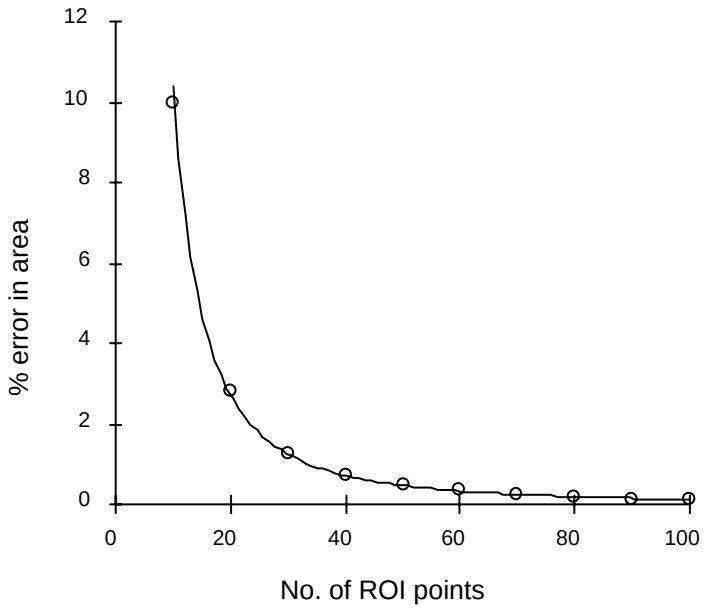

Figure 7.1 The percentage error in calculating the area of a circle for increasing number of ROI points.

In this theoretical study underestimation always occurs as the ROI points are assumed to be connected by straight lines. In reality the situation will be different as some traced ROI points will fall outside the true edge and some inside. ROIs will also vary in size, tending to decrease in size towards the ends of an object.

7.3.3 Effect of the number of image planes on error

To assess the effect of the number of image slices on accuracy, a prolate ellipsoid was generated with axes of 120, 40 and 20. Fifty ROI points were generated for each slice. Two techniques were used to generate the ROIs. In the first, equally spaced ROIs were generated, and in the second the angle subtended between the ROI points and the centroid was the same between ROIs resulting in more closely spaced ROIs in the polar regions.

Figure 7.2 shows a plot of the CAN volume versus number of ROIs. This shows that greater accuracy can be achieved with fewer slices when there is a concentration of ROIs towards the poles. For example with 20 slices, the error is 2% for the equal space model and only 1% for the equal angle model. A skillful ultrasonographer could perhaps make use of this.

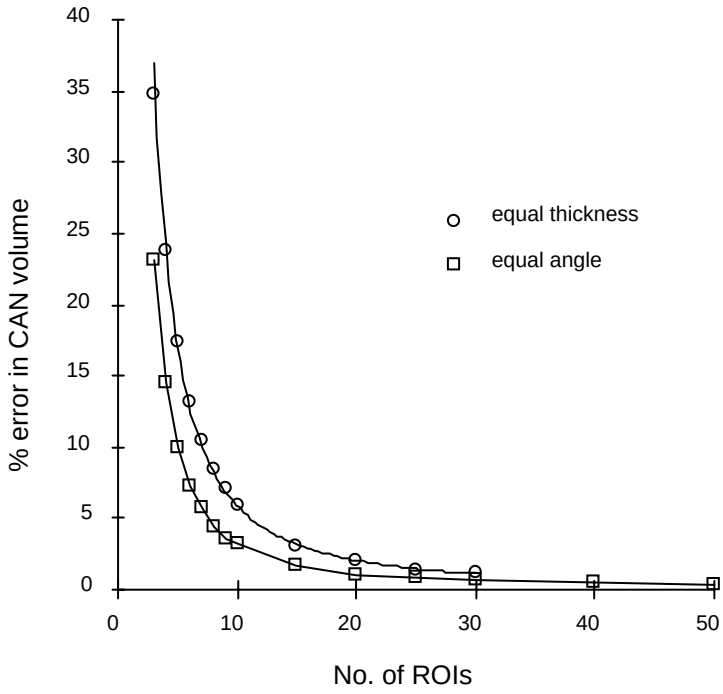

Figure 7.2 Plot of the CAN volume versus number of ROIs for a prolate ellipsoid with equally spaced ROIs and one with a greater concentration of ROIs near the poles.

Alternatively more images could be acquired than needed and some of the central ones not used for drawing ROIs. The planimetry and centroid tetrahedral volumes were also calculated and the errors were very similar to the CAN algorithm.

7.3.4 Refraction and velocity errors

Refraction and velocity errors cannot be treated separately. A difference between the acoustic propagation velocity of two media will result in a transmitted ultrasound beam being refracted if the incident angle is non-parallel to the surface normal. Therefore not only is the beam deviated, but the apparent length on the image will also be different. Practically, refraction will occur in 3D. However, the 3D problem can be simplified by independently considering 'in-plane' and 'out-of-plane' refraction. In-plane refraction occurs within the plane of an image, whereas out-of-plane refraction deviates the whole image from the incident plane.

7.3.4.1 In-plane refraction

Refraction occurs according to Snell's law which is depicted diagramatically in figure 7.3. A model was produced in Excel.

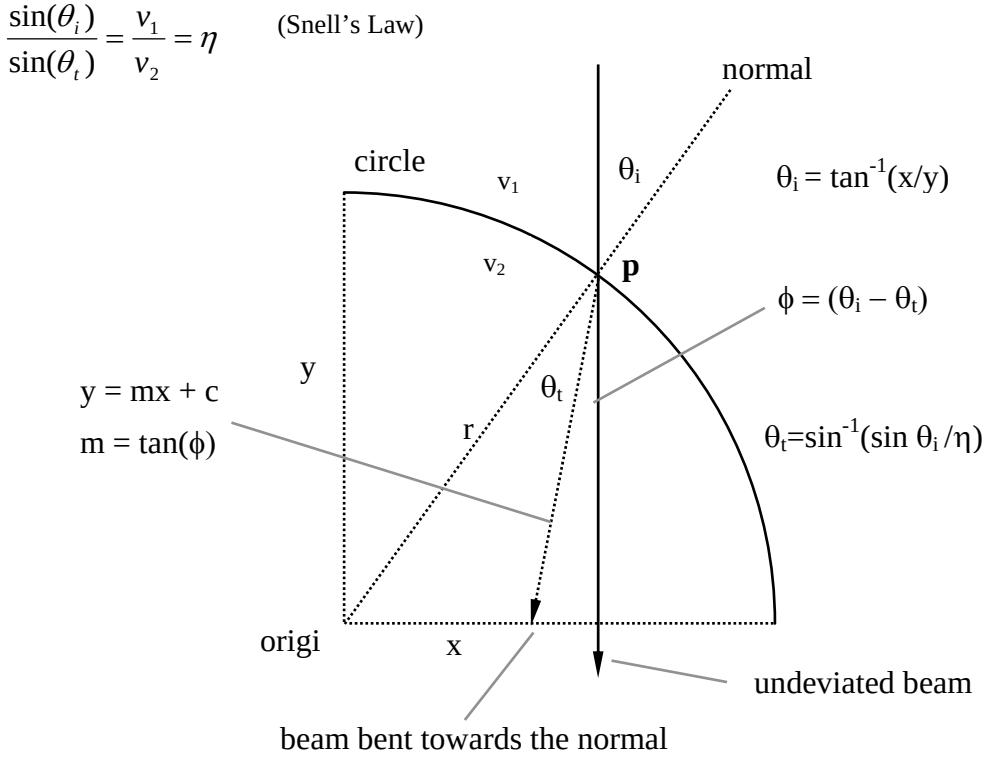

Figure 7.3 Schematic diagram of refraction.

A circle of radius r was generated of unity radius, x,y origin 0,0 using $r^2 = y^2 + x^2$, $\therefore y = (r^2 - x^2)^{1/2}$. Figure 7.3 shows a ray propagating through a medium with acoustic propagation velocity v_1 passing through into medium v_2 via a circular boundary. For $v_2 < v_1$ the ray is bent towards the normal as depicted in the diagram. The incident and transmission angles are as defined. The gradient of the transmission path is simply the tangent of the transmission angle. The equation of the transmission path can be found by substituting the x,y coordinates of a point on the line - in this case it is convenient to take the interaction point (**p**) on the boundary.

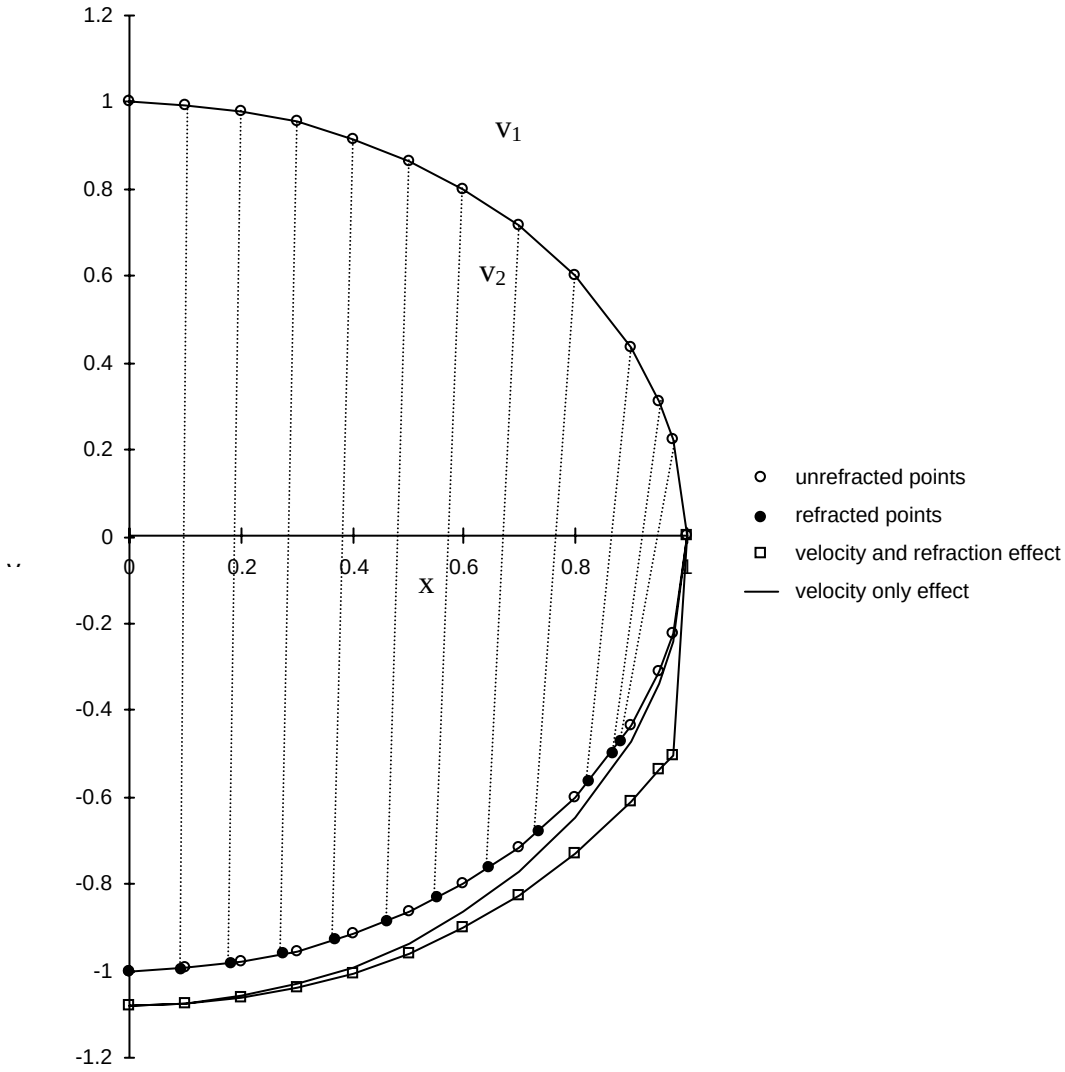

Figure 7.4 Refraction and velocity error when $v_1 > v_2$.

The bent transmitted beam propagates through the medium and is reflected at the far boundary and is assumed to come back along the same path to the transducer. From the

point of view of the transducer, the beam has travelled in a straight line without deviation, which in this model is only true at the apex of the circle. The angle of refraction increases as the angle between the normal increases, therefore the beam intercepts the circle in the model progressively towards the left of the straight through line as shown in figure 7.4. This intercept point is calculated by solving the equations of the refracted line (7.1) and that of the circle (7.2).

$$y = mx + c \tag{7.1}$$

$$y = (r^2 + x^2)^{1/2} \tag{7.2}$$

combining 7.1 and 7.2 we obtain:

$$mx + c = (r^2 + x^2)^{1/2} \tag{7.3}$$

after rearranging we arrive at:

$$(m^2 + 1)x^2 + 2cmx + (c^2 - r^2) = 0 \tag{7.4}$$

which we note is a quadratic equation of the form:

$$ax^2 + bx + c = 0 \tag{7.5}$$

which has two solutions given by:

$$x = \frac{-b \pm \sqrt{(b^2 - 4ac)}}{2a} \tag{7.6}$$

where in this case:

$$a = (m^2 + 1)$$

$$b = 2cm$$

$$c = (c^2 - r^2)$$

The two solutions correspond to the two x intercepts of the line with the circle, i.e. the interaction point **p** and the reflection on the far side of the circle. The y coordinates can be found by inserting the x values into equation 7.1 or 7.2.

The distance that the refracted beam has travelled is found by subtracting the position vectors of the two intercepts. This distance needs to be adjusted by the refractive index. In the first model example - a water filled cyst embedded in soft tissue, the refractive index (η) is = 1540/1480 = 1.04. Most ultrasound machines assume a velocity of sound of 1540 ms^{-1}. Therefore in the model, the beam has travelled through the 1480 ms^{-1} region with an assumed velocity of 1540 ms^{-1}. This will result in the distance travelled being over-estimated by a factor of 1.04. This is illustrated in figure 7.4 where the apparent far border of the circle is beyond the true border.

In figure 7.4, note that the refracted rays intercept the circle deeper than the original point. The effect becomes very much more pronounced at steeper angles to the normal. This effect tends to produce a constant increase in depth. The effect is of the circle shifted downwards. The inner line in figure 7.4 shows the effect of the velocity error when the refraction angle is ignored. Note that at shallower incident angles the velocity effect predominates, whereas at steeper angles the refraction effect predominates. The area of each semi-circle was calculated using equation 2.17.

The area of the unit semi-circle (shown in figure 7.4) is 1.56 and the refracted circle 1.67, this represents an increase of 7%. This theoretical experiment serves to show that refraction and velocity propagation effects combined can be significant. (N.B. a curvilinar array centred on a circle would tend to cancel refraction effects). The refractive index can be varied in the model and the effect on volume calculated. The circle could be replaced by an ellipse or any other geometric shape.

7.3.4.2 Out-of-plane refraction

Out-of-plane refraction is illustrated in figure 7.5. This was also modelled in Excel using the same refractive index as the in-plane refraction model. In this case the whole image

plane is refracted. The case is for an ultrasound beam impinging on a water filled cavity as in the previous example. In this case it is assumed that the beam passes through a rectangular prism. Therefore the error in measuring volume is directly proportional to the error in measuring the thickness of medium v_2 (Δa). As the incident angle increases so the beam bends progressively towards the normal.

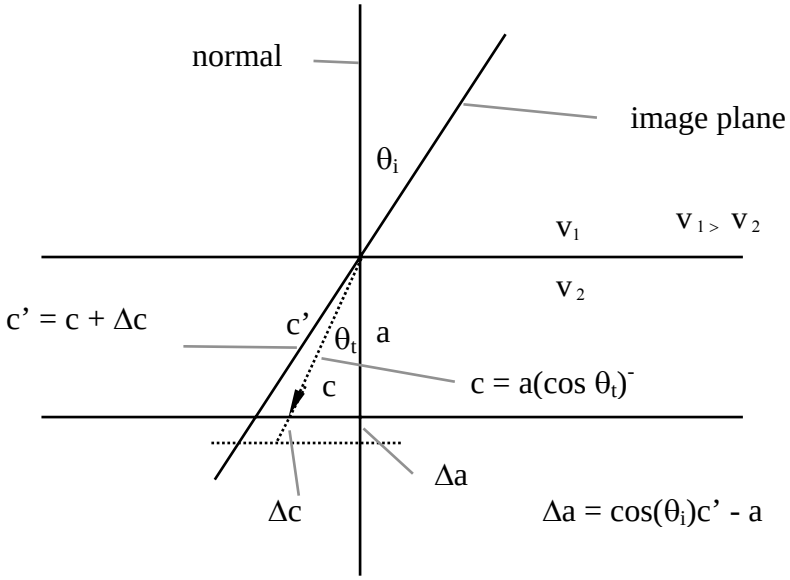

Figure 7.5 Out-of-plane refraction.

The consequence of this is that the path length to the far interface becomes shorter as the incidence angle (θ_i) increases. Figure 7.6 shows a plot of the percentage decrease in volume with incident angle. Note that when the beam is parallel to the normal, the error is just given by the difference between the refractive index and unity (i.e. only a velocity correction is necessary).

If an organ was being imaged by parallel slices tilted at 30^o to the vertical, the error would be ~ 3.6% by taking the mean of the curve in figure 7.6. If an organ were being imaged using the radial technique, say with images oriented at 0 ± 30^o the error is approximately equal to the mean incident angle, i.e. the error at 15^o which is ~ 3.8%. In

reality, the situation would be more complicated, for example, different parts of an image may be refracted differently.

Figure 7.6 Percentage error in volume for out-of-plane refraction versus incident angle.

7.3.5 Fastrak mis-alignment and signal perturbation

In most cases the ultrasound transducer is moved across the patient without a great change in angle. For example if a fetal organ 5 cm long is scanned at a depth of 9 cm using the transducer shown in figure 3.2, a sector angle of 56^o would be required. (This is taking into account the fact that the Fastrak receiver is 17.9 cm above the front face of the transducer in contact with the skin corresponding to a gearing ratio of 2). Chapter 5 showed that at about normal scanning height, the angular and positional accuracy over a 60^o excursion was 0.18 ± 0.06^o ($1.2 \pm 0.4\%$) and 0.0 ± 0.2 mm ($0.05 \pm 0.73\%$) respectively. Over the whole 60^o excursion, the chord length was measured as 9.96 cm, compared to the actual value of 10 cm (0.4 mm error). The angle was measured as 60.57^o compared to the actual value of 60^o.

To simplify the situation, positional and angular errors can be considered separately. Assume that an organ is being scanned with parallel scans as depicted in figure 7.7. Also assume that by chance all of the positional error is in the direction of the long axis of the organ, therefore the error only affects the two vectors shown (compare with figure 2.2).

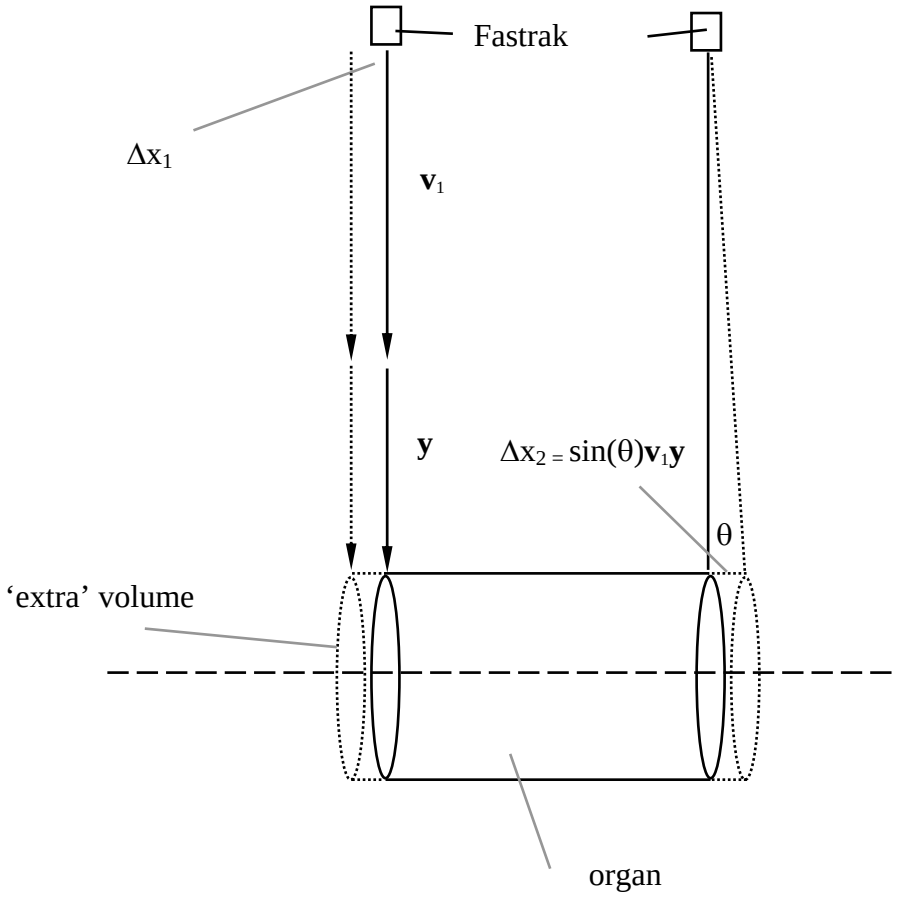

Figure 7.7 Positional and angular error.

If the vectors are perfectly aligned with the image plane, then the two vectors ($\mathbf{v}_1$,$\mathbf{y}$) can be considered to be a single vector, and therefore the receiver positional error will be transmitted all the way down to then end. (N.B. a single vector can be decomposed into any number of smaller vectors along its length with the same positional error).

The actual error will of course depend on the length and area of the object being scanned. For example, if a 10 cm long cylinder were scanned, the Fastrak positional error would increase the length by 0.04 cm. If the area of the cylinder was 10 cm (volume = 100 cm^3) the error in the volume would be 0.4 cm^3 or 0.4%. Considering angular error: if $\mathbf{v}_1$ and $\mathbf{y}$ are assumed to have a combined length of 20 cm, and that the Rx coordinate system happens to be rotated 0.18^o about the LOH axis, the error at the end of error will be $\sin(0.18^o)$ 20cm = 0.6 mm.

If the positional and angular errors acted in concert this would result in an overall positional error of 1 mm, which in the example above would result in a volume error of 1 cm^3 or 1%. The error could of course go the other way. In reality the situation would be very much more complicated.

Apart from displacement errors as discussed above, angular errors can lead to ROIs being skewed from their true orientation. Suppose that an ultrasound beam is cutting through a cylinder at right angles to the long axis. If the Fastrak errors are negligible a near perfect cylinder will be constructed from ROIs drawn on the images. However, errors in the measurement of orientation will result in the transformed ROIs being skewed. This could also arise through patient movement or if the scanned object is translated normally to the long axis of the organ. The same kind of error will also result if the Fstrak receiver is mis-aligned with the axes of the ultrasound transducer.

Figure 7.8 shows a schematic depiction of a parallelepiped with two ROIs on opposite faces. The volume of the parallelepiped is given by the product of area (A) and thickness (t). If t remains constant as the parallelepiped is tilted, the volume will decrease as a sine function. It follows that the volume between the two ROIs shown will also decrease as a sine function.

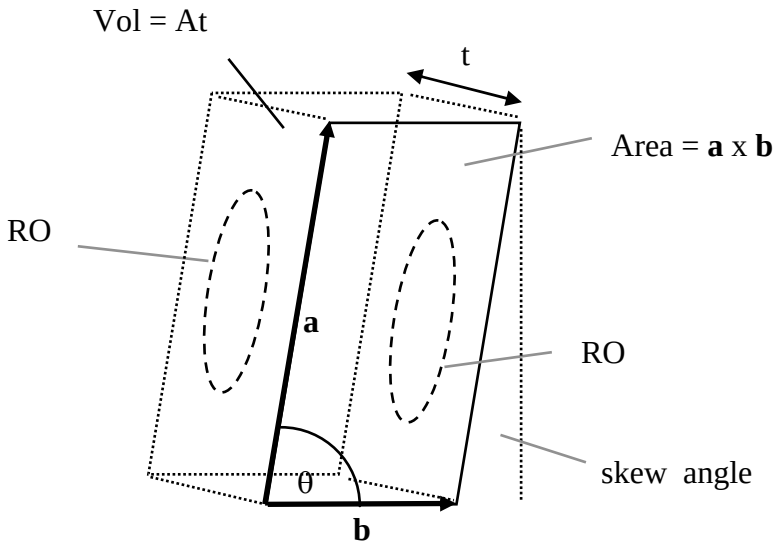

Figure 7.8 Skewed parallelepiped.

(N.B. this is an alternative way of understanding the planimetry method devised by Watanabe, although in that case the tilted ROIs correctly sample the shape of the organ, whereas in this case the tilt is a distortion). Figure 7.9 shows a plot of the percentage error in volume (sin(θ)-1) x 100.

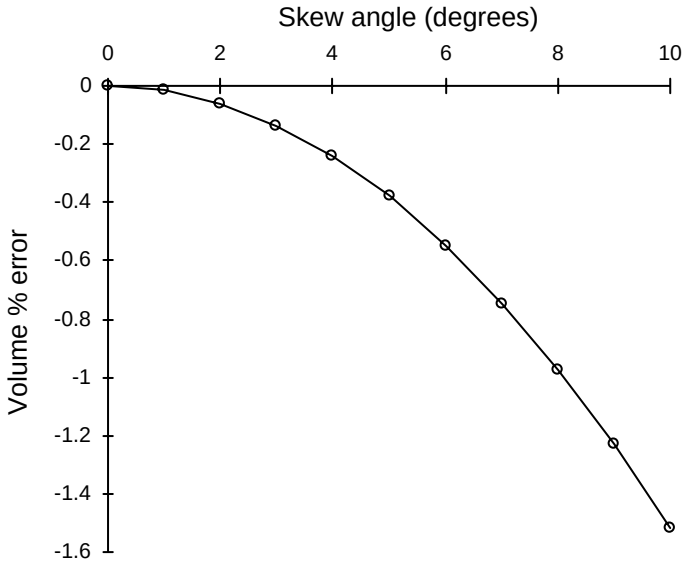

Figure 7.9 Percentage error in volume versus ROI skew angle.

These values show that there is a fair amount of tolerance - the error does not reach -1% until the skew angle is ~ 8^{o}. Over small receiver excursions systematic skew will be fairly small depending on how the rotation of the receiver coordinate system varies as a function of x,y,z.

7.3.6 Large scale vertical and horizontal accuracy of ultrasound scanners

7.3.6.1 Introduction

It is important to have some idea of the accuracy and resolution of an ultrasound scanner as this has a bearing on the accuracy of measuring volume.

7.3.6.2 Method

Two scanners were tested using the Cardiff resolution test object (Gammex-RMI Ltd, Nottingham, UK) which contains parallel wires of known separation embedded in tissue equivalent gel. The velocity of sound in the gel is ~1540 ms^{-1} at room temperature. The

tests involve measuring distances between wires and assessing the minimum wire separation that can be resolved.

Wires in the test phantom were imaged using an Acuson 128XP/10 scanner with a 5 MHz curvilinear probe. The maximum image depth was set to 14 cm with a medium depth focus (~ 7cm). The axial and horizontal resolutions, slice thickness, and the vertical and horizontal large scale caliper accuracies were measured. The vertical and horizontal large scale caliper accuracies quantifies the accuracy of measuring vertical and horizontal distances on an image. The scanner calipers are used to measure distances between successive pairs of wires. The measurements were repeated on an Hitachi EUB-240 with a 3.5 MHz linear array transducer. The maximum image depth was set to 18 cm with a medium depth focus (~ 9 cm).

7.3.6.3 Results

The results of the tests are shown in table 7.1. The Hitachi calipers could only read to an accuracy of 1 mm therefore the accuracy has been estimated as 1 ± 1mm. Figure 7.10(a) shows a scatter plot of caliper depth versus phantom depth for the Acuson 128XP/10 scanner. The values for the Hitachi are not included as they are deceptively accurate. The Hitachi caliper precision is only 1 mm but the caliper tends to fall exactly on the wires, which are at integer mm depths, therefore the scanner appears to have no error, (at least at depths below 80 mm). Figure 7.10(b) shows a Bland-Altman plot of the same data. Figure 7.11(a) shows the horizontal large scale caliper accuracy for the two machines and figure 11(b) shows a Bland-Altman plot of the same data. Note that the Hitachi SD is small compared to the mean error, which indicates a systematic error rather than a random error. However, these errors apply to the measurement of absolute depth relative to the top of the transducer.

7.3.6.4 Discussion

Qualitatively, the image quality of the Acuson scanner is much better than the Hitachi scanner. This is confirmed quantitatively by the test results. The large scale vertical and horizontal accuracies dictate the absolute accuracy with which the vertical and horizontal distances between two points can be measured. The error in measuring area will be dependent on the absolute size of the ROI. The error in measuring area can be estimated

by considering the error in measuring a square. Assume that a square, 50 mm on a side is being imaged.

Table 7.1 Accuracy and resolution values (mm) for ultrasound scanners. LSCA = Large Scale Caliper Accuracy.

	Acuson 128XP/10	Hitachi EUB-240
Vertical LSCA	0.16 ± 0.1	~ 1 ± 1.0
Horizontal LSCA	0.6 ± 0.5	2.4 ± 1.0
Axial resolution	< 1	1 - 2
Horizontal resolution	1.25 – 2.5	2.5 - 5
Slice thickness	3 - 6	6 - 9

For the Acuson 128XP/10 scanner, the mean error in measuring area will be (50 + 0.16) (50 + 0.6) = 25.38 cm^2 an error of 0.38 cm^2 (1.6%), and for the Hitachi EUB-240 (50 + 1.0) (50 + 2.4) = 26.72 , an error of 1.72 cm^2 (6.8%). The range for the Acuson is ± 0.3 cm^2.

(a)

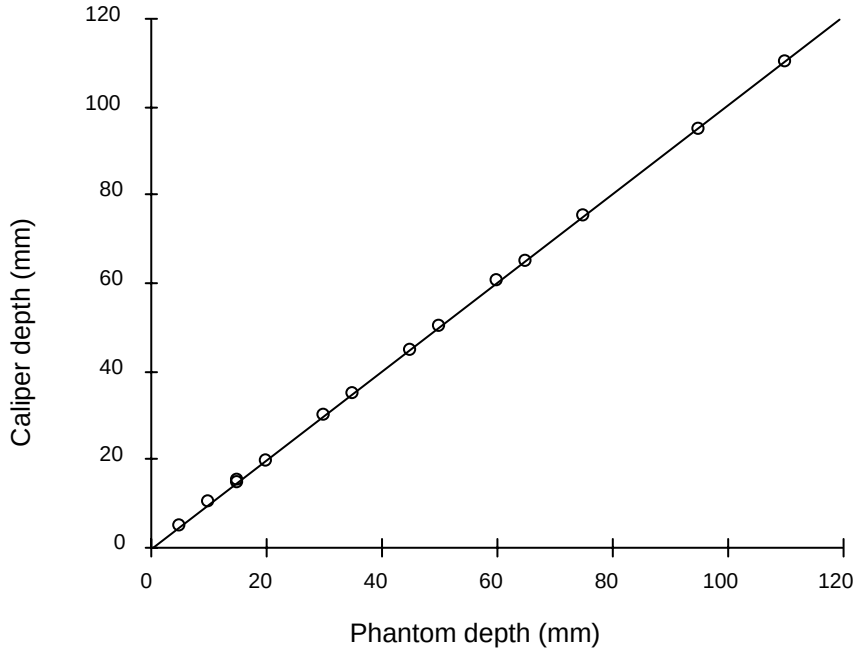

(b)

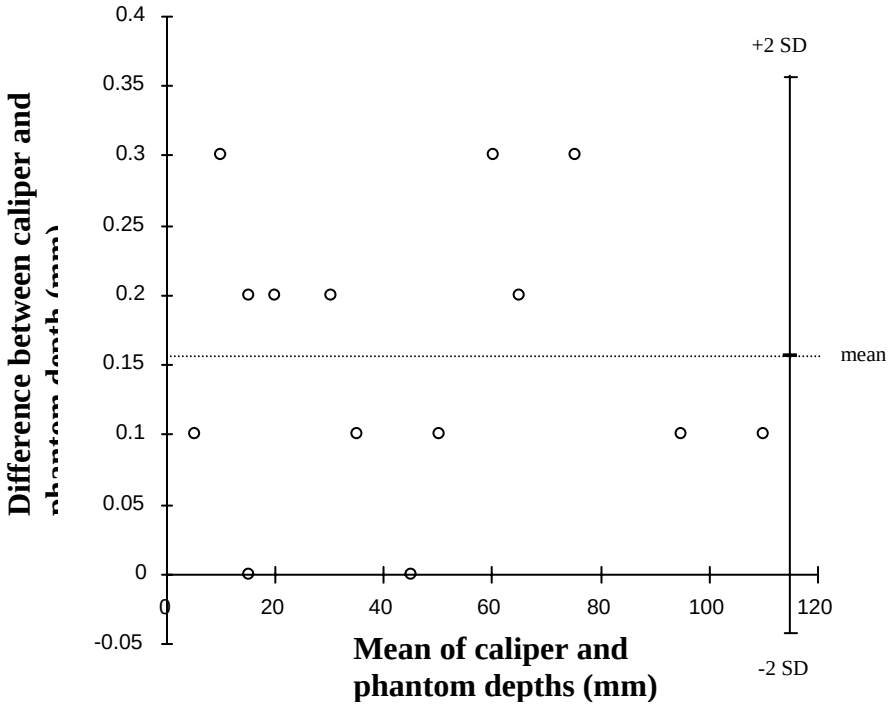

Figure 7.10 (a) Acuson 128XP/10 vertical caliper depth versus phantom depth. (b) Bland-Altman

(a)

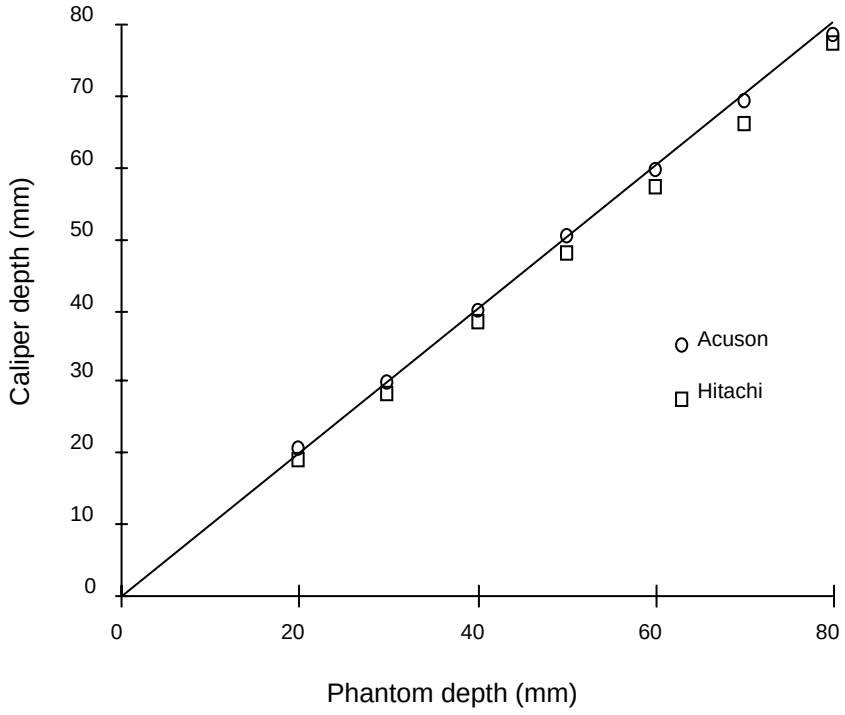

(b)

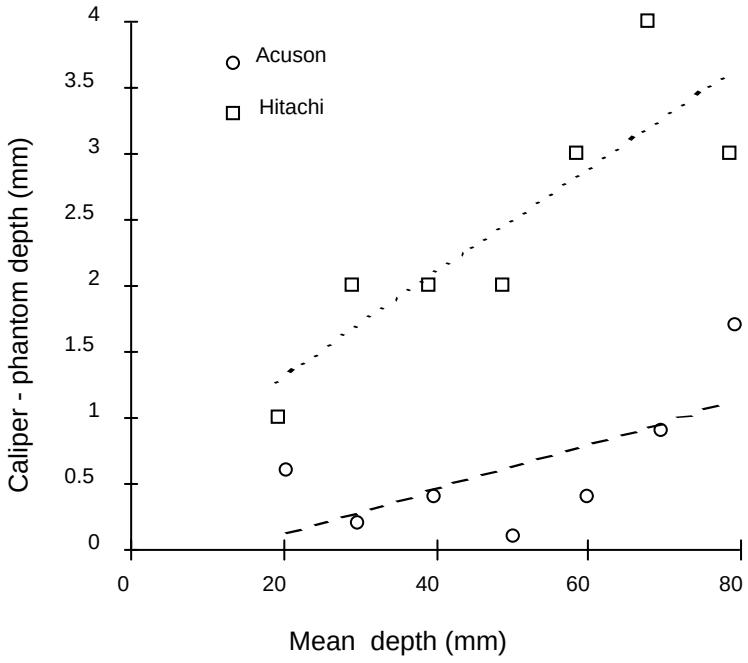

Figure 7.11 (a) Horizontal caliper depth versus phantom depth for an Acuson 128XP/10 and Hitachi EUB-240. The line of identity is shown. (b) Bland-Altman plot. Regression lines are shown to indicate the general trend of the data.

7.3.7 Accuracy of the displacement method of estimating volume

7.3.7.1 Introduction

Three methods were devised for measuring the actual volume of the objects used in the experiments. The first involved placing the objects in a graduated water cylinder and measuring the increase in water level. This method was used to calculate the actual volume of the kidneys and livers as described in sections 6.3.2 and 6.4.2. Generally, the smaller the bore of the cylinder the more accurate the volume measurement, therefore the smallest bore just able to fit the object should be chosen. The rise in the either the bottom or top of the meniscus is recorded. The object must be denser than water for this technique to be successful. This technique was used for measuring the volume of the porcine kidneys and fetal livers. (N.B. the balloon volumes could be measured directly by weighing, assuming a density of 1g cm^{-1} for water).

Two further methods were developed in an attempt to improve on the accuracy of the first method. Unfortunately the kidneys and livers were no longer available for these other techniques to be used. However, the rocks were used to compare the accuracy of the first method with the two new methods.

The second technique involves placing the object in a container with a spout projecting down and out of the side so that the over-flow can be collected in a container and weighed.

The third technique involves weighing a container of water before and after suspending the object below the surface. This technique works for objects of any density that are non-absorbing. If the object is more dense than water there will be a net downward force on the chord equal to the weight of the object minus the weight of the water displaced by the object. The effect of the suspended object is the same as adding a volume of water equal to that of the object. An invisible boundary can be imagined in the water of the same size and shape as the suspended object. The boundary is stationary as there is no net force, therefore the weight of the water in the container increases by the weight of the water displaced by the suspended object.

This principle can be thought of as an adjunct to Archimedes principle which states *that an object floating in a fluid displaces a weight of fluid equal to the weight of the object*.

The priciple used in this experiment could be phrased: *when an object is completely immersed in fluid, the weight of the fluid increases by an amount equal to the weight of fluid displaced - i.e. the volume of the object divided by the density of the fluid*.

7.3.7.2 Method

Ten irregularly shaped clay rocks (as described in chapter 3), were painted with varnish to protect against absorption of water. The assumption was made that the layer of varnish would not significantly increase the volume. About 10 cm of surgical suture was attached to each rock using a small amount of araldite. It was assumed that the araldite did not significantly increase the volume. Each rock was suspended in a 250 ml beaker of water placed on an electronic balance (Sartorius MC1, Sartorius AG, Gottingen, Germany) as shown in figure 7.12. The weight of water was measured before and after immersion to an accuracy of $\pm$ 0.01 g. The rocks were dried with a paper towel and the measurements repeated within an hour. The small length of chord between the connection point on each rock and the top surface of the water was ignored.

The rocks were also placed in an aluminium container with a downward projecting spout. The overflow was collected for a period of three minutes for each rock. (A few tests ascertained that most of the water that was going to overflow had done so by this time). The rocks were placed in the container before the chords were attached. The collected water was weighed on the same electronic balance.

The rocks were also placed in a 500 ml glass measuring cylinder, although the two largest rocks had to be placed in a 2000 ml cylinder. The height of the bottom of the meniscus was recorded before and after immersion of the rocks. The process was repeated a day or so later.

7.3.7.3 Results

The overflow and level techniques were compared with the weight technique. Figure 7.13(a) shows a scatter plot of the overflow and level volumes versus the weight volume.

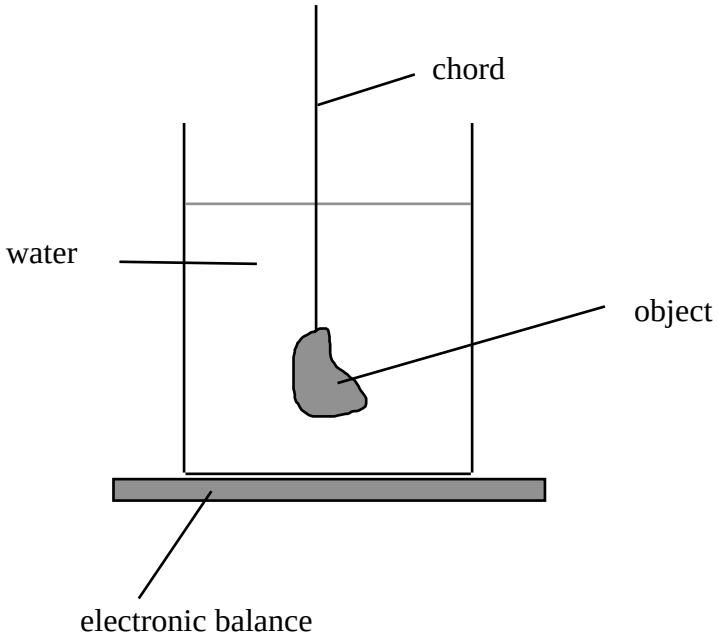

Figure 7.12 Schematic diagram of the weighing method of determining volume.

Figure 7.13(b) shows a Bland-Altman plot of the same data. Table 7.2 shows basic results and table 7.3 the repeatability of the techniques. Table 7.4 shows the agreement between the three techniques, and table 7.5 shows the agreement between the three techniques and voxel counting.

Table 7.2 The weight, overflow and level volume values.

rock	weighing	overflow	level
1	4.85	4.42	4.8
2	13.13	13.33	14.0
3	39.85	40.78	43.0
4	27.83	26.94	28.0
5	22.59	22.74	24.0
6	10.84	11.54	12.0
7	16.82	16.72	17.0
8	101.83	101.44	101.0
9	83.01	82.71	85.0
10	57.42	57.01	58.0

(a)

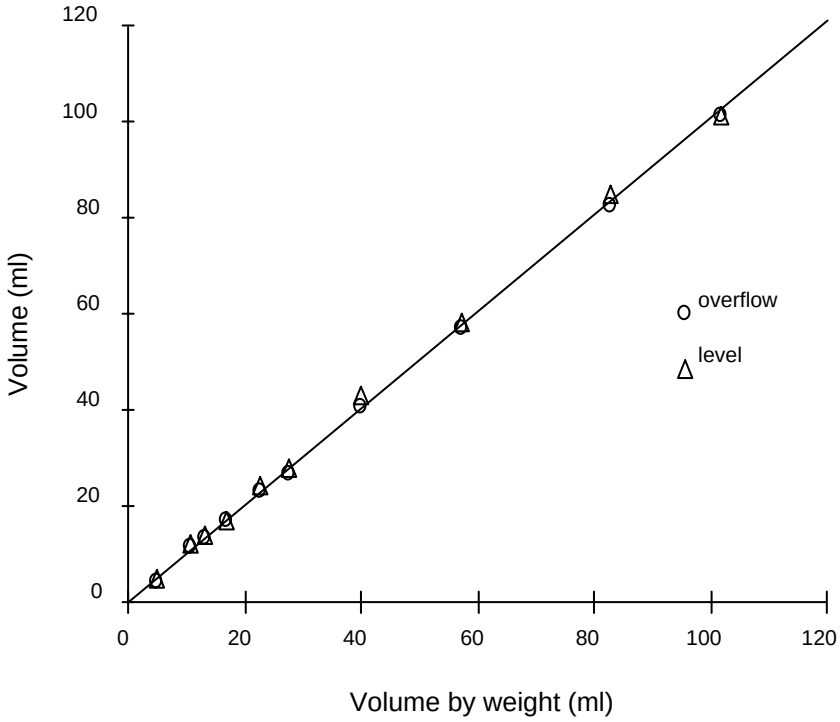

(b)

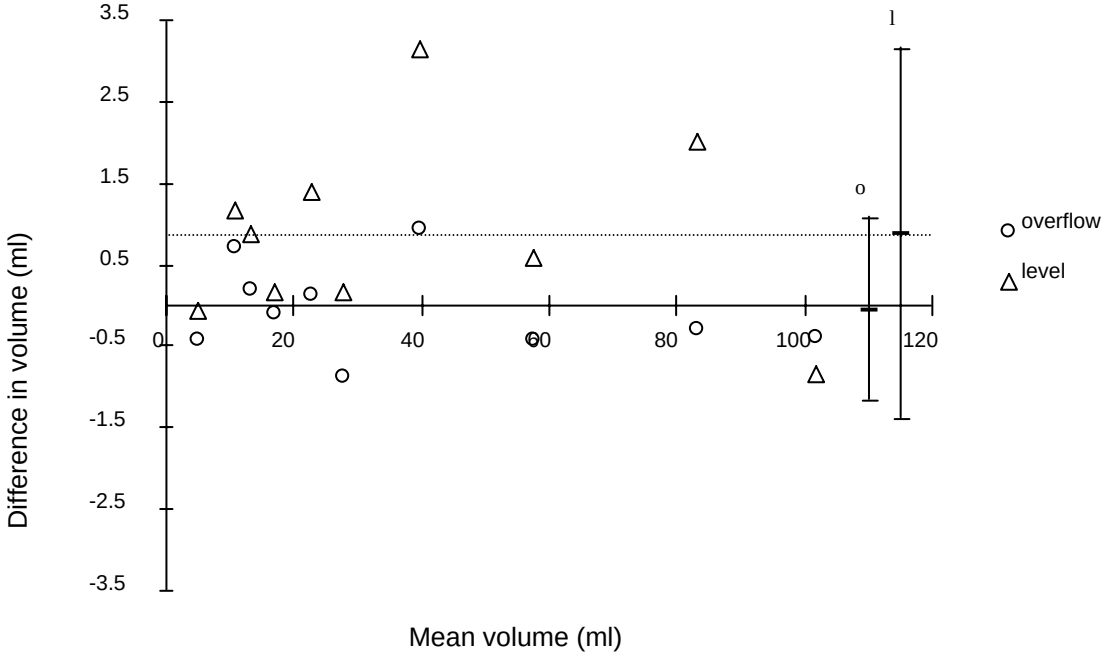

Figure 7.13 (a) Overflow and level volumes versus the weight volume. (b) Bland-Altman plot of the same data.

Table 7.3 Repeatability of the level, overflow and weighing displacement methods of measuring volume expressed as the mean ± SD of the difference in ml between two successive measurements.

method	mean	SD
level	-0.51	0.97
overflow	0.05	0.56
weight	0.017	0.033

Table 7.4 Agreement between the level, overflow and weighing displacement methods of measuring volume expressed as the mean ± SD of the difference between measurements made by two of the techniques.

methods	mean	SD
weight - level	-1.37	0.88
weight - overflow	-0.055	0.55
level - overflow	-1.43	0.95

Table 7.5 Agreement between voxel counting and the three displacement methods of calculating volume.

methods	mean	SD
voxel - weight	-1.41	1.23
voxel - overflow	-1.46	1.34
voxel - level	-0.04	0.85

7.3.7.4 Discussion

The weight method was the most repeatable and the level method the least repeatable. This is to be expected as the level method is subjective in that it relies on the observer to decide on the position of the meniscus which usually falls between marks. The weight and overflow methods agreed most closely. A surprising result is that the level method agrees most closely with the voxel volume. This result is difficult to explain but could perhaps be due to shrinkage of the rocks. The initial level volumes were measured at the

time of scanning (within a few days) whereas the overflow and weight volumes were carried out several months later. The level measurements repeated at the this later date do suggest that some of the larger rocks may have shrunk by 1 - 2 ml. Nevertheless, these results suggest that all three methods are reasonably accurate.

The level method is clearly the most convenient. The overflow method is quite tedious as three minutes are required to collect the overflow. The weighing method will provide the greatest accuracy for small objects. For large organs it may be difficult to obtain an electronic balance with the required dynamic range. (The weight technique could be used with a conventional balance but this would be very difficult).

7.4 Summary

A large number of factors affect the overall error in measuring volume. The overall *in vitro* accuracy and precision is of the order of a few percent. From this it can perhaps be inferred that the individual errors are of the same order, or smaller and are tending to cancel. However, the overall *in vivo* error is likely to be higher due to the large errors that can occur in delineating ROIs (~10% or greater).

CHAPTER 8

Conclusion

8.1 Introduction

This chapter summarises the main findings of the thesis, and some future avenues of investigation are suggested.

8.2 Main conclusions

This work has shown that in *vitro* volume measurements can be made to an accuracy and precision of less than 5% with a 3D ultrasound system utilising an external electromagnetic tracking device. Similar accuracies are obtained with various scanning techniques and volume calculation algorithms. The Fastrak device selected for the system is sensitive to metal but performs adequately in the clinical environment.

8.3 Advantages and disadvantages of the various volume algorithms

All of the volume algorithms apart from the ellipsoid method produce results which are not significantly different. Therefore it follows that if a reasonable number of cross-sectional images and ROI points are obtained it does not matter which algorithm is used. However, it is good engineering practice to have a number of back-up methods. Each method can serve as a check on the others, and provide useful information about the shape of the organ.

For example, if the ellipsoid volume is close to the others then this may indicate that the organ or structure is ellipsoidal in shape. If the centroid-tetrahedral method is over-estimating then this may be due to the organ being a 'banana' shape. If the tetrahedral, Gauss and RTA methods are low compared to the planimetry method then this may be due to holes in the surface due to incorrect triangulation.

The volume algorithms vary in ease of implementation. The ellipsoid method is clearly the most straight forward and requires the least number of calculations. Planimetry is the next easiest as triangulation is not required. The CAN method is dependent on good

triangulation of the surface and requires that all the triangle normals point either out of or into the surface. (If half the normals pointed out of the surface and half into the surface, the volume elements would cancel producing a result close to zero). This can be done by checking whether the end of a triangle normal is closer or further away from the centroid of the whole object than the triangle centroid.

Table 8.1. Summary of the advantages and disadvantages of the volume algorithms.

Algorithm	**Advantage**	**Disadvantage**
ellipsoid	Simple, quick	Can be very inaccurate
planimetry	Quick, ROIs do not have to be connected into a triangle mesh.	Adjacent image planes must be close in distance and angle and orthogonal to the long axis of the object. Difficult to use if there's more than one ROI in an image plane.
Centroid tetrahedral	Triangles do not have to be constructed from ROI points on adjacent image planes.	Must be a clear line of sight between the object centroid and each vertex. Holes must be treated as separate objects.
Slice tetrahedral	Better with shapes for which there is no clear line of sight between the object centroid and every vertex.	Holes have to be treated as separate objects. Each triangle must be assigned to a band.
CAN	Works for any closed surface. ROIs do not need to be in planes. Works on multiple objects.	Surface normals must point in a consistent direction.
RTA	As for the CAN. In addition, the volume of overlap of two or more superimposed objects can be calculated.	Computationally intensive and therefore slower than the other algorithms.

The direction of a normal is reversed by reversing the sign of the x,y and z components. However, ensuring that normals point in a consistent direction is difficult in cases where

regions of the mesh fold back into the object. (This difficulty does not occur with meshes produced by the marching cubes algorithm as the algorithm is able to consistently determine the local direction of surface normals). However, the sign of the triangle normal components are not important for the RTA and hence this algorithm is more robust in this respect.

8.4 Comparison of dedicated 3D-US transducers with remote localised 2D-US

Dedicated 3D transducers and remote localiser systems have inherent advantages and disadvantages and are therefore complimentary rather than competing. The dedicated 3D systems currently available comprise a linear or curvilinear transducer which is translated and/or rotated within an housing. So in effect dedicated and remote systems operate on the same principle. An advantage of remote localiser systems is that the sonographer can use his or her skill to obtain the best series of images for reconstruction. Dedicated 3D systems tend to be quite bulky as the transducer and mechanism have to be housed together. Compromises are bound to be made, for example, the transducer has to be smaller than it would be if it was stand-alone. Indeed, if some of the standard probes were placed inside a housing with a mechanical sweep mechanism they would be far too large to use.

Another fundamental problem with dedicated transducers is the volume of insonation. A typical 'footprint' might be $\pm 30^{o}$. The shallower angle of incidence at the extremes will lead to less well defined structure boundaries. The mechanical design of dedicated 3D systems restricts the field of view close to the transducer, therefore large structures cannot be imaged if at an insufficient depth below the transducer. With remote systems a much wider field of view is available right up to the transducer.

Dedicated 3D systems require that the transducer be kept stationary during the scan. This can be difficult with a hand held probe, especially if there is significant vibration from the sweep motor. Vibration is not an issue with remote localiser systems as position and orientation data are acquired in a very short time (~ ms).

There is a sign outside a local car wash - "some things are best done by hand" - this is still true of ultrasound.

8.5 Clinical trials

The system described in this thesis has been used to measure the volume of fetal livers and lungs at various gestations, as part of a wider project investigating intra-uterine growth retardation (see list of publications at the end of the thesis). MR has also been used to estimate fetal liver, lung and brain volume in fetuses in the third trimester (Mansfield *et al*, 1990, Stehling *et al* 1990, Roberts *et al* 1994, Baker *et al* 1994, 1995). Echo-planar imaging was performed in order to avoid as much as possible the problem of fetal movement. 2D slices were acquired in 30 ms, of the same order as ultrasound. Although echo-planar imaging is a superb obstetric research tool it is unlikely to become routine because of shear cost (hundreds of pounds per scan) and inconvenience.

MRI is not as accessible as US. For example, MR scanners are generally housed in an imaging centre removed from obstetric clinics. Mothers have to be carefully positioned in (a claustrophobic for some) scan aperture and not move for several minutes - away from human contact. There is the additional worry of metallic objects. Spouses, and especially children must be kept well away from the scan room. The loud banging noise made by the magnetic will be distressing to some mothers and may even disturb the baby.

The ultrasound experience is quite difference - there is a far more intimate a relationship between the mother and ultrasonographer, any worries or fears can be confidentially discussed. The mother and companions can see very clearly what is going on, ask questions and be told what they are seeing. There is no problem with children sitting and watching - apart from opening cupboards and running away down the corridor (as personally experienced by the author)

8.6 Future work

8.6.1 Metal compensation

The use of the Fastrak could be extended to clinical environments where there is significant interference from metal. It is possible to compensate for metal in the environment. Polhemus provide a service (at a price) for carrying out measurements at the customer site, or the machine can be purchased for around £100,000. The transmitter

is placed at a reproducible location and the receiver is moved to a number of known locations using a mechanical translation device. An array of error transformation matrices are built up for the whole space. (This was briefly discussed in the section 5.3.4). The matrices can be interpolated to correct for subsequent position and orientation readings which fall between the calibration points (in practice virtually every reading).

A cheaper compensation system could be developed utilising a device such as the Faro arm (Faro Technologies Inc, FL, USA) cost ~ £9,000. Some means would have to be devised for attaching the Fastrak reciever to a long plastic rod to ensure that the arm is far enough away to cause minimal disturbance of the transmitted magnetic field. Maybe this would be difficult to achieve, but it may be worth further investigation.

A major problem with the compensation approach is that the scan environment is constantly changing, the couch is moved according to the whim of the sonographer, couches move slightly anyway when patients get on and off. The position of the machine, auxiliary monitors, metal trolley etc. change position or are moved into or away from the immediate vicinity. Perhaps extra receiver could be placed at constant locations with respect to the transmitter to monitor the environment - if it changes then the separation and orientation between the transmitter and sentinel receiver will also vary.

The performance of the Fastrak system in a metal rich environment could perhaps be improved by having a pulse system. The electronics could be set up to only analyse the signal induced within the receiver coils within a certain time span from the first perturbation. The time span should be short enough to ensure that the magnetic field has not had time to reach and return from metal objects beyond the receiver. However, care must still be taken to ensure that metal is excluded from the direct line of sight and no significant amounts of metal should be closer to the transmitter than the receiver.

No doubt Polhemus will continue to refine their product. Perhaps they will produce a version that does not require any cable attachment (say by using an infrared connection like a remote control unit or chordless computer keyboard). This would make receiver even easier to use attach to the transducer - although this is not so much of a problem as the ultrasound probe has a cable attachment anyway. (Perhaps even chordless ultrasound

probes could be developed in the future). It would also be useful if the Fastrak system was produced as a PC board (a lower accuracy system is in fact already available).

8.6.2 Multi-directional image acquisition

If sequences of images were acquired from multiple directions, it may be possible to delineate the boundary of an organ more accurately. It can be difficult to see the poles of an ellipsoidally shaped organ with transverse image sections. However, if sagittal images are taken the ends can be better delineated. Two or more sets of ROIs (for example transverse and sagittal) could be combined. The RTA can be used to calculate the volume of an object enclosed by two or more merged triangle meshes.

8.6.3 Use of Doppler and contrast agents

The 3D system could be used on images containing flow information (Doppler). Segmentation of Doppler images should be easier, and enable 3D images of vascular trees etc. to be obtained. Ultrasound contrast agents are also beginning to be used which may be useful in 3D work.

8.6.4 Computational Medical Imaging

Ultrasound technology continues to improve resulting in improved image quality. This improvement should lead to better elucidation of anatomy and tissue characterisation. This could facilitate computational studies, for example finite element analysis (FEA) to be carried out. Rudimentary FEA studies have already been carried out, for example, Lee at al. (1993) carried out finite element analysis on models of the iliac artery wall derived from 2D ultrasound images of cadaveric iliac arteries. Lee et al. were able to predict sites of plaque fracture to within 15^{o} of that found by experiment, but were unable to predict balloon inflation pressures required to produce the lesions.

However, they suggest that this may be possible with better ultrasound images, particularly combined to produce a 3D model of the vessel wall. They also suggest that predictions could be improved by more accurate values for the material properties of normal and diseased vessel walls. Allied to this, improvements in ultrasound tissue characterisation could also lead to more accurate *in vivo* FE models. It is possible to

envisage the application of this type of technique to many parts of the vasculature, particularly the heart. A lot of computer power is required (Lee et al. carried out the FEA on a CRAY X-MP supercomputer) but this is becoming less of a problem as the cost of computing continues to fall.

8.6.5 Simulated ultrasound imaging

Scientifically, the best way to validate *in utero* volume measurements would be to scan a mother about to undergo a termination of pregnancy, however their are serious ethical considerations that makes this difficult. This problem could possibly be overcome by developing computer code to accurately simulate *in vivo* imaging.

The ray tracing algorithm could perhaps form the basis of code to simulate refraction and velocity effects. Such a model could prove useful in overcoming ethical dilemmas in validating the *in vitro* measurement of organ volume. A possible way to do it at present would be to scan a mother prior to undergoing termination of pregnancy. There are three issues here. One is a moral one - if you disagree with terminations is it right to use material from the aborted fetus? It was for this reason that this form of validation was not carried out for this thesis. A second issue is that an ultrasound examination immediately prior to termination would be very stressful for the mother (especially seeing a little life moving on the screen). This kind of research could also tip the balance in favour of a termination if the mother new that some good would result.

The Polkinghorne report (Polkinghorne 1989) recommends that a mother only be told about the possible use of material from the adorted fetus *after* she has given consent for the termination to proceed. The committee also suggest that there be a clear separation between those who obtain the material (i.e. the obstreticians) and the researchers (who may be other obstreticians). They suggest the formation of a central tissue bank where fetal tissue can be stored and given out to research groups. The idea is that the ‘providers’ do not know where the material is going and the researchers do not know its provenance.

If an accurate enough model cold be produced then it might be possible to realistically simulate the scanning of a baby in the womb and therefore estimate the actual error in estimating organ volume.

In some ways this work would be analogous to the American development of computer code able to accurately simulate the detonation of nuclear warheads. In this case real bomb data was used to refine the model. (N.B. in 1996, it was been suggested that the Americans share this information with the French to obviate Pacific bomb tests). As computers continue to get cheaper but also increase in speed and memory an accurate ultrasound simulator enters the realm of the possible.

Ultrasound will increase in use as medical procedures become less invasive. Such procedures, for example ‘keyhole surgery’ are heavily reliant on real time imaging, for which ultrasound is eminently suited. Less invasive procedures are less traumatic and painful for the patient, and result in a shorter time in hospital. Patients recover faster, and procedures are cheaper (less time in hospital, fewer drugs, less doctor time etc.)

REFERENCES

Absy M, Metreweli C, Matthews C, Al Khader A. Changes in transplanted kidney volume measured by ultrasound. Brit. J. Radiol. 1987; 60:525-529.

Ammeraal L. Programming principles in computer graphics. John Wiley, Chichester, 1986.

Alyassin AM, Lancaster JL, Downs JH. Evaluation of new algorithms for the interactive measurement of surface area and volume. Med. Phys. 1994; 21:741-752.

Austin JHM, Gooding CA. Roentgenographic measurement of skull size in children. Radiology 1971; 99:641-646.

Baker PN, Johnson IR, Gowland PA, Freeman A, Adams V, Mansfield P. Estimation of fetal lung volume using echo-planar magnetic resonance imaging. Obstetrics and Gynaecology 1994; 83: 951-954.

Baker PN, Johnson IR, Gowland PA, Freeman A, Adams V, Mansfield P. Measurement of fetal liver, brain and placental volumes with echo-planar magnetic resonance imaging. Br. J. Obstet. Gynaecol. 1995; 102:35-39.

Bamber JC, Hill CR. Ultrasonic attenuation and propagation speed in mammalian tissues as a function of temperature. Ultrasound in Med. & Biol. 1979; 5:149-157.

Bamber JC, Hill CR. Ultrasonic propagation through fixed and unfixed tisues tissues. Ultrasound in Med. & Biol. 1979; 5:159-165.

Bartsch G, Egender G, Hubscher H, Rohr H. Sonometrics of the prostate. J. Urol. 1982; 127:1119-1121.

Basset O, Gimenez G, Mestas JL, Cathignol D, Devonec M. Volume measurement by ultrasonic transverse or sagittal cross-sectional scanning. Ultrasound in Med. & Biol. 1993; 17:291-296.

Baxter BS, Sorenson JA. Factors affecting the measurement of size and CT number in computed tomography. Investigative Radiology 1981; 16:337-341.

Bland JM, Altman DG. Statistical methods for assessing agreement between two methods of clinical measurement. Lancet 1986 I:307-310.

Bland JM, Altman DG. Comparing methods of measurement: why plotting difference against standard method is misleading. Lancet 1995; 346:1085-1087.

Blankenhorn DH, Chin HP, Strikwerda S, Bamberger J, Hestenes JD. Common carotid artery contours reconstructed in three dimensions from parallel ultrasonic images. Radiology 1983; 148:533-537.

Blaas HG, Eik-Nes SH, Berg S, Angelsen B, Olstad B. Three-dimensional imaging of the brain cavities in human embryos. Ultrasound Obstet. Gynecol. 1995; 5:228-232.

Blum MD, Bahnson RR, Lee C, Deschler TW, Grayhack JT. Estimation of canine prostatic size by in vivo ultrasound and volumetric measurement. J.Urol.1985; 133:1082-1086.

Brann BS, Wofsy C, Wicks J, Brayer B. Quantification of neonatal cerebral ventricular volume by real-time ultrasonography: Derivation and in vitro confirmation of a mathematical model. J. Ultrasound Med. 1990; 9:1-8.

Brann BS, Wofsy C, Papile L, Angelus P, Backstrom C. Quantification of neonatal cerebral ventricular volume by real-time ultrasonography: In vivo validation of the cylindrical coordinate method. J. Ultrasound Med.1990; 9:9-15.

Brann BS, Qualls C, Papile L, Wells L, Werner S. Measurement of progressive cerebral ventriculomegaly in infants after grades III and IV intraventricular hemorrhages. J. Pediatr. 1990; 117:615-621.

Brann BS, Qualls C, Wells L, Papile L. Asymmetric growth of the lateral cerebral ventricle in infants with posthemorrhagic ventricular dilation. J. Pediatr. 1990; 118:108-112.

Brinkley JF, Moritz WE, Baker DW. Ultrasonic three-dimensional imaging and volume from a series of arbitrary sector scans. Ultrasound in Med. & Biol. 1978; 4:317-327.

Carpenter DA, Kossoff G, Griffiths KA. Correction of distortion in US images caused by subcutaneous tissues: results in tissue phantoms and human subjects. Radiology 1995; 195:563-567.

Cline HE, Lorenson W E, Ludke S. Two algorithms for the three-dimensional reconstruction of tomograms. Med. Phys. 1988; 15:320-327.

Cook T, Cook PN, Lee KR, Batnitzky S, Wong BYS. An algorithm for volume estimation based on polyhedral approximation. IEEE Trans. Biomed. Eng. 1980; BME-27:493-500.

Cooke JM, Zyda MJ, Pratt DR, McGhee RB. NPSNET: Flight simulation dynamic modelling using quarternions. Presence 1992; 1:404-420.

Docker MF, Duck FA. The safe use of diagnostic ultrasound. British Institute of Radiology 1991.

Dodge HT, Sandler H, Ballew DW, Lord JD. The use of biplane angiocardiography for the measurement of left ventricular volume in man. Am. Heart. J. 1960; 60:762-776.

Eaton LW, Maughan WL, Shoukas AA, Weiss JL. Accurate volume determination in the isolated ejecting canine left ventricle by two-dimensional echocardiography. Circulation 1979; 60:320-326.

Ennis BM, Zientek DM, Ruggie NT, Billhardt RA, Klein LW. Characterization of a saphenous vein graft aneurysm by intravascular ultrasound and computerized three-dimensional reconstruction. Catheterization and Cardiovascular Diagnosis 1993; 28:328-331.

Feynman R P, Leighton R B, Sands M. The Feynman Lectures on Physics (Addison-Wesley, Reading, MA), 1964: 2:3-4.

Fine D, Perring S, Herbetko J, Hacking CN, Fleming JS. Three-dimensional imaging of the gallbladder and dilated biliary tree: reconstruction from real-time B-scans. Brit. J. Radiol. 1991; 64:1056-1057.

Foley FD, van Dam A, Feiner SK, Hughes JF. Computer graphics: principles and practice. Addison-Wesley, New York, 1990.

Gardener JE, Lees WR, Gillams A. Volume imaging with US. Radiology 1991; 181(P):133.

Geiser EA, Lupkiewicz SM, Christie LG, Ariet M, Conetta DA, Conti CR. A framework for three-dimensional time-varying reconstruction of the human left ventricle: sources of error and estimation of their magnitude. Computers and biomedical Research 1980; 13:225-241.

Geirsson RT, Christie AD, Patel N. Ultrasound volume measurements comparing a prolate ellipsoid method with a parallel planimetric area method against a known volume. J. Clin. Ultrasound 1982; 10:329-332.

Ghosh A, Nanda NC, Maurer G. Three-dimensional reconstruction of echocardiographic images using the rotation method. Ultrasound in Med. & Biol. 1982; 8:655-661.

Gilja OH, Thune N, Matre K, Hausken T, Odegaard S, Berstad A. In vitro evaluation of three-dimensional ultrasonography in volume estimation of abdominal organs. Ultrasound in Med. & Biol. 1994; 20:157-165.

Gilja OH, Smielvoli AI, Thune N, Matre K, Hausken T, Odegaard S, Berstad A. In vitro evaluation of three-dimensional ultrasonography in volume estimation of abdominal organs. Ultrasound in Med. & Biol. 1995; 21:25-32.

Gohari P, Berkowitz RL, Hobbins JC. Predication of intrauterine growth retardation by determination of total intrauterine volume. Am. J. Obstet. Gynecol. 1977; 127:255-260.

Gopal AS, King, DL, Katz J, Boxt LM, King DL, Jr, Shao MY-C. Three-dimensional echocardiographic volume computation by polyhedral surface reconstruction: *In vitro* validation and comparison to magnetic resonance imaging. J. Am. Soc. Echocardiogr. 1992; 5:115-124.

Gueret P, Meerbaum S, Wyatt HL, Uchiyama T, Lang TW, Corday E. Two-dimensional echocardiographic quantitation of left ventricular volumes and ejection fraction. Circulation 1980; 62:1308-1318.

Hamper UM. Trapanotto V. Sheth S. DeJong MR. Caskey CI, Three-dimensional US: preliminary clinical experience. Radiology 1994; 191:397-401.

Harris KM, Adams H, Lloyd DCF, Harvey DJ. The effect on apparent size of simulated pulmonary nodules of using three standard CT window settings. Clinical Radiology 1993; 47:241-244.

Hastak SM, Gammelgaard J, Holm HH. Transrectal ultrasonic volume determination of the prostate - a preoperative and postoperative study. J. Urol. 1982; 127:1115-1118.

Helak JW, Reichek N. Quantitation of human left ventricular mass and volume by two-dimensional echocardiography: in vitro validation. Circulation 1981; 63:1398-1407.

Hell B, Walter FA, Schreiber S, Blase H, Bielke G. Three-dimensional ultrasonography in maxillofacial surgery. A new diagnostic tool. International Journal of Oral & Maxillofacial Surgery 1993; 22:173-177.

Henderson J, Wilson K, Jago JR, Whittingham TA. A survey of the acoustic outputs of diagnostic ultrasound equipment in current clinical use. Ultrasound in Med. & Biol. 1995; 21:699-705.

Hodges TC, Detmer PR, Burns DH, Beach KW, Strandness DE Jr. Ultrasonic three-dimensional reconstruction: *in vitro* and *in vivo* volume and area measurement. Ultrasound in Med. & Biol. 1994; 20:719-729.

Jiang L, Siu SC, Handschumacher MD, Guererro JL, Vazquez de Prada JA, King ME, Picard MH, Weyman AE, Levine RA. Three-dimensional echocardiography In vivo validation for right ventricular function. Circulation 1994; 89:2342-2350.

Keats TE, Enge IP. Cardiac mensuration by the cardiac volume method. Radiology 1965; 85:850-855.

Kelly IMG, Gardener JE, Lees WR. 3-dimensional fetal ultrasound. Lancet 1992; 339:1062-1064.

Kelly IMG, Gardener JE, Brett AD, Richards R, Lees WR. Three-dimensional US of the fetus. Radiology 1994; 192:253-259.

Kennedy DN, Filipek PA, Caviness VS. Anatomic segmentation and volumetric calculations in nuclear magnetic resonance. IEEE Trans. Biomed. Eng. 1989;
BME-8: 1-7.

King DL, King DL Jr, YiCi Shao M. Three-dimensional spatial registration and interactive display of position and orientation of real-time ultrasound images.
J. Ultrasound Med. 1990; 9:525-532.

Kirschener-Hermanns R, Klein HM, Muller U, Schafer W, Jakse G. Intra-urethral ultrasound in women with stress incontinence. Brit. J. Urol. 1994; 74:315-318.

Klein H, Marqaurt M, Polz H, Schuller G. 3D reconstruction of fetal images based on ultrasound. In: Computer Assisted Radiology. 534-538. Ed: Lemke, H.U.; Inamura, K.; Jaffe, C.C.; Felix, R. Proceedings of the International Symposium, Berlin, 1993.

Koehler PR, Anderson RE, Baxter B. The effect of computed tomography viewer controls on anatomical measurements. Radiology 1979; 130:189-194.

Kok-Hwee Ng, Evans JL, Vonesh MJ, Meyers SN, Mills TA. Arterial imaging with a new forward-viewing intravascular ultrasound catheter, II, Three-dimensional reconstruction and display of data. Circulation 1994; 89:718-723.

Kreyszig E 1993 Advanced Engineering Mathematics (New York: John Wiley)

Lancaster JL, Eberly D, Alyassin A, Downs JH, Fox PT. A geometric model for measurement of surface distance, surface area, and volume from tomographic images. Med. Phys. 1992; 19: 419-431.

Lees WR, Chong WK, Lawrence R, Gardener J. Intravascular ultrasound with 3D reconstruction: a new way to image vascular disease. Brit. J. Radiol. 1991; 64:655.

Lees WR, Gerdener JE, Gillams A. Three-dimensional US of the fetus. Radiology 1991; 181(P):132.

Lees WR, Gardener JE, Brett AD, Davey MK. Assessment of 3D US image acquisition. Radiology 1993; 189(P):341.

Levine RA, Handschumacher MD, Sanfilippo AJ, Hagege AA, Harrigan P. Three-dimensional echocardiographic reconstruction of the mitral valve, with implications for the diagnosis of mitral valve prolapse. Circulation 1989; 80:589-598.

Levine SC, Filly RA, Creasy RK. Identification of fetal growth retardation by ultrasonic estimation of total intrauterine volume. J. Clin. Ultrasound. 1979; 7:21-26.

Linker DT, Moritz WE, Pearlman AS. A new three-dimensional echocardiographic method of right ventricular volume measurement: in vitro validation, J. Am. Coll. Cardiol. 1986; 8:101-106.

Littrup PJ, Williams CR, Egglin TK, Kane RA. Determination of prostate volume with trasnrectal US for cancer screening, part II. Accuracy of in vitro and in vivo techniques. Radiology 1991; 179:49-53.

Mansfield P, Stehling MK, Ordidge RJ, Coxon R, Chapman B, Blamire A, Gibbs P, Johnson JR, Symonds EM, Worthington BS, Coupland RE. Echo-planar imaging of the human fetus *in utero* at 0.5 T. Brit. J. Radiol. 1990; 63:833-841.

Martin RW, Bashein G, Detmer PR, Moritz WE. Ventricular volume measurement from multiplanar transesohageal ultrasonic imaging system: an *in vitro* study. IEEE Trans. Biomed. Eng. 1990; BME-37:442-449.

Martin RW, Bashein G, Nessly ML, Sheehan FH. Methodology for three-dimensional reconstruction of the left ventricle from transesophageal echocardiograms. Ultrasound in Med. & Biol. 1993; 19:27-38.

Martin RW, Bashein G, Zimmer R, Sutherland J. An endoscopic micromanipulator for multiplanar transesophageal imaging. Ultrasound in Med. & Biol. 1977; 3:163-178.

Matsumoto M, Inoue M, Tamura S, Tanaka K, Abe H. Three-dimensional echocardiography for spatial visualisation and volume calculation of cardiac structures. J. Clin. Ultrasound 1981; 9:157-165.

McLachlan MSF, Williams ED, Fortt RW, Doyle FH. Estimation of pituitary gland dimensions from radiographs of the sella turcica. Brit. J. Radiol. 1968; 41:323-330.

Moritz WE, Pearlman AS, Mc Cabe DH, Medema DK, Ainsworth ME, Boles MS. An ultrasonic technique for imaging the ventricle in three dimensions and calculating its volume. IEEE Trans. Biomed. Eng. 1983; BME-30:482-492.

Newnham JP, Evans SF, Michael CA, Stanley FJ, Landau LI. Effects of frequent ultrasound during pregnancy. Lancet 1993; 342:887-891.

Picot PA, Rickey DW, Mitchell R, Rankin RN, Fenster A. Three-dimensional doppler imaging. Ultrasound in Med. & Biol. 1993; 19:95-104.

Pini R, Monnini E, Masotti L, Greppi B, Gerofolini M. Echocardiographic computed tomography of the heart: preliminary results. J. Am. Coll. Cardiol. 1989; 49:896.

Pleet H, Graham JM, Smith DW. Central nervous system and facial defects assocaited with maternal hyperthermia at four to 14 weeks' gestation. Pediatrics 1981; 67:785 -789.

Polkinghorne J, Review of the guidance on the research use of fetuses and fetal material. (Cm 762) HMSO London 1989.

Pretorius DH, Nelson TR, Jaffe JS. 3-dimensional sonographic analysis based on color flow Doppler and gray scale image data: a preliminary report. Journal of Ultrasound in Medicine 1992; 11:225-232.

Raichlen JS, Trivedi SS, Herman GT, St.John Sutton MG, Reichek N. Dynamic three-dimensional reconstruction of the left ventricle from two-dimensional echocardiograms. J. Am. Coll. Cardiol. 1986; 8:364-370.

Rasmussen S. Liver volume determination by ultrasonic scanning. Brit. J. Radiol. 1972; 45:579-585.

Robb RA, Barillot C. Interactive display and analysis of 3-D medical images. IEEE Trans. Biomed. Eng. 1989; BME-8:217-226.

Roberts N, Garden AS, Cruz-Orive LM, Whitehouse GH, Edwards RHT. Estimation of fetal volume by magnetic resonance and stereology. Bri.t .J Radiol. 1994; 67: 1067-1077.

Rosenfield K, Kauffman J, Pieczek AM, Langevin RE, Palefski PE. Human coronary and peripheral arteries: on-line three-dimensional reconstruction from two-dimensional intravascular US scans. Radiology 1992; 184:823-832.

Rosenfield K, Losordo DW, Ramaswamy K, Pastore JO, Langevin RE. Three-dimensional reconstruction of human coronary and peripheral arteries from images recorded during two-dimensional intravascular ultrasound examination. Circulation 1991; 84:1938-1956.

Salvesen KA, Eik-Nes SH, Undheim JO, Okland O. Routine ultrasonography in utero and school performance at age 8-9 years. Lancet 1992; 339:85-89.

Salvesen KA, Vatten LJ, Eik-Nes SH, Hugdahl K, Bakketeig LS. Routine ultrasonography in utero and subsequent handedness and neurological development. BMJ 1993; 307:159-164.

Saunders RD. Limits on patient and volunteer exposure during clinical magnetic resonance diagnostic procudures: recommendations for the practical implementation of the board's statement. National Radiological Protection Board 1991; 2:1

Sawada H, Fujii J, Kato K, Onoe M, Kuno Y. Three dimensional reconstruction of the left ventricle from multiple cross sectional echocardiograms, Value for measuring left ventricular volume. Br. Heart J. 1983; 50:438-42.

Schiller NB, Acquatella H, Ports TA, Drew D, Goerke J, Ringertz H, Silverman NH, Brundage B, Botvinick EH, Boswell R, Carlsson E, Parmley WW. Left ventricular volume from paired biplane two-dimensional echocardiography. Circulation 1979; 60:547-555.

Schlesinger, AE, Hildebolt, CF, Siegel, MJ, Pilgrim, TK. Splenic volume in children: simplified esitmation at CT. Radiology 1994; 193:578-580.

Sehgal CM, Broderick GA, Gorniak RJ, Arger PH. Three-dimensional imaging of prostates with transrectal sonography. Radiology 1993; 189(P):342.

Shinozuka N, Okai T, Kohzuma S, Mukubo M, Shih Chen-Ting, Maeda T, Kuwabara Y, Mizuno M. Formulas for fetal weight estimation by ultrasound measurements based on neonatal specific gravities and volumes. Am. J. Obstet. Gynecol. 1987; 157:1140-5.

Stehling MK, Mansfield P, Ordidge RJ, Coxon R, Chapman B, Blamire A, Gibbs P, Johnson JR, Symonds EM, Worthington BS, Coupland RE. Echo-planar imaging of the human fetus *in utero.* Magn. Reson. Med. 1990; 13:314-318.

Stroud KA. Engineering mathematics. London, Macmillan, 1984.

Styles RA, Neal DE, Powell PH. Reproducibility of measurement of prostatic volume by ultrasound. Eur. Urol. 1988; 14:266-269.

Teicholz E, Cohen MV, Sonnenblick EH, Gorlin R. Study of left ventricular geometry and function by B-scan ultrasonography in patients with and without asynergy. N. Engl. J. Med. 291:1220-1226; 1974.

Tortoledo FA, Quinones MA, Fernandez GC, Waggoner AD, Winters WL. Quantification of left ventricular volumes by two-dimensional echocardiography: a simplified and accurate approach. Circulation 1983; 67:579-584.

Watanabe Y, Nose Y, Sanefuji SA, Yokota M, Nakamura M. A method to estimate volume and surface area of organ by two-dimensional echocardiography. IEEE Trans. Biomed. Eng. 1981; BME-28:294-296.

Watanabe Y. A method for volume estimation by using vector areas and centroids of serial cross-sections. IEEE Trans. Biomed. Eng. 1982; BME-29:202-205.

Wells PNT. The safety of diagnostic ultrasound. Brit. J. Radiol. 1987: Supl. 20.

Wyatt HL, Heng MK, Meerbaum S, Hestenes JD, Cobo JM, Davidson RM, Corday E. Cross-sectional echocardiography I. Analysis of mathematical models for quantifying mass of the left ventricle in dogs. Circulation 1979; 60:1104-1113.

Wyatt HL, Heng MK, Meerbaum S, Hestenes JD, Cobo JM, Davidson RM, Corday E. Cross-sectional echocardiography III. Analysis of mathematical models for quantifying volume of symmetric and asymmetric left ventricles. American Heart Journal 1980; 100:821-828.

Wollschlager H, Zeiher AM, Klein H, Kasper W, Wollschlager S. Transesophageal echo computer tomography: a new method for dynamic 3-D imaging of the heart. J. Am. Coll. Cardiol. 1989; 13:68A.

Zimmermann R, Hebisch G, Huch R, Huch A. Letter. Lancet 1993; 342:1359.

Publications

Journal Publications

Hughes SW, D'Arcy TJ, Maxwell DJ, Chiu W, Milner A, Saunders JE, Sheppard RJ, Volume estimation from multiplanar 2D ultrasound images using a remote electromagnetic position and orientation sensor. Ultrasound in Med. Biol. 1996; 22: 561-572.

Hughes SW, D'Arcy TJ, Maxwell DJ, Saunders JE, Ruff C, Chiu WSC, Sheppard RJ. Application of a new discreet form of Gauss' theorem for measuring volume. Physics in Medicine and Biology 1996; 41:1809-1821.

D'Arcy TJ, Hughes SW, Chiu W, Milner AD, Maxwell DJ, Saunders JE. Estimation of fetal lung volume using enhanced 3-dimensional ultrasound: a new method and first result. Brit. J. Obstet. Gynaecol. 1996; 103:1015-1020.

Hughes SW, D'Arcy TJ, Maxwell DJ, Saunders JE, Sheppard RJ. Accuracy of a new system for estimating organ volume using ultrasound. Physiological Measurement 1997; 18:73-84.

Hughes SW, D'Arcy TJ, Maxwell DJ, Saunders JE. In vitro estimation of fetal liver volume using US, CT and MR. Physiological Measurement, 1997.

Abstracts/Proceedings

D'Arcy TJ, Hughes SW, Chiu W, Maxwell DJ. Accurate ultrasound estimation of fetal organ volume using a three-dimensional multimedia PC-based system. Proceedings of the Rontgen Centenary Congress, Birmingham, p 458, 1995.

D'Arcy TJ, Hughes SW, Chiu WC, Maxwell DJ. Volumetric measurement of fetal livers based on 3-dimensional ultrasound imaging. British Medical Ultrasound Society, December 1994, (Br. J. Radiol Proceedings 1995).

D'Arcy TJ, Hughes SW, Chiu WC, Maxwell DJ. The measurement of fetal liver volume using magnetic resonance imaging, computerised tomography and a computerised 3-

dimensional ultrasound system. The Blair Bell Research Society / R.C.O.G. February 1995, (Br. J. Obstet & Gynaecol Proceedings 1995).

D'Arcy TJ, Hughes SW, Chiu WC, Milner A, Maxwell DJ. The estimation of fetal lung volume using 3-dimensional ultrasound. Registrar's Prize Meeting, Section of Obstetrics and Gynaecology, Royal Society of Medicine, February 1995 (Proceedings RSM).

Hughes SW, D'Arcy TJ, Chiu WC, Maxwell DJ, Saunders JE. Three dimensional ultrasound and measurement of volume. IPSM, York, March 1995.

D'Arcy TJ, Hughes SW, Chiu WC, Maxwell DJ. IUGR: fetal weight or organ volume. Invitation Lecture Victor Bonney Society Meeting May 1995.

D'Arcy TJ, Hughes SW, Chiu WC, Maxwell DJ. Antenatal measurement of fetal lung volume using a new 3-dimensional ultrasound system. The British Congress of Obstetrics and Gynaecologists July 1995.

Hughes SW, D'Arcy TJ, Maxwell DJ, Chiu W, Milner A, Saunders JE. Volume estimation from multiplanar 2D ultrasound images using an electromagnetic registration device. 1995 World Congress on Ultrasonics, Berlin, September 3 to 7.

Hughes SW, D'Arcy TJ, Chiu W, Maxwell D, Milner A, Saunders JE. Volume estimation of fetal and neonate organ volume using 3D ultrasound. 5th International Conference on Fetal and Neonatal Physiological Measurement, plus Therapeutic Technology, Keele University, 2-5 September 1995.

D'Arcy TJ, Ruff C, Hawkes D, Hughes SW, Bhalerao A, Chiu W, Maxwell D, Saunders JE. Volume estimation of shape characterisation of fetal organs. 5th International Conference on Fetal and Neonatal Physiological Measurement, plus Therapeutic Technology, Keele University, 2-5 September 1995.

Chiu W, D'Arcy TJ, Hughes SW, Maxwell D, Saunders J. The development of a portable 3-dimensional ultrasound system. 5th International Conference on Fetal and Neonatal Physiological Measurement, plus Therapeutic Technology, Keele University, 2-5 September 1995.

Chiu W, D'Arcy TJ, Hughes SW, Maxwell DJ, Saunders JE. The development of a portable 3-dimensional ultrasound system. 1995 World Congress on Ultrasonics, Berlin, September 3 to 7.

Hughes SW, D'Arcy TJ, Ruff CJ, Maxwell DJ, Saunders JE. Measurement of Organ Volume volume using 3D ultrasound. In: Computer Assisted Radiology, 1996, 210-215. Ed: Lemke, HU, Vannier, MW, Inamura, Farman, AG, Proceedings of the International Symposium on Computer and Communications Systems for Image Guided Diagnosis and Therapy, Berlin.

Acknowledgements

I would like to thank the following people for their help and support. Mr Tom D'Arcy, who was my main clinical collaborator throughout this project. Daryl Maxwell and John Saunders (the directors of fetal medicine and medical physics respectively). Dr. Adrian Timothy for paying for my college fees and for introducing me to Mr. Anthony Kenny, who arranged initial funding through the Muirhead Trust, and later from Tommy's Campaign. Prof. Anthony Milner for his enthusiastic encouragement throughout the project. Roy Snow, Chris Bunton and John Pilmer of the medical physics workshop at St. Thomas' Hospital for constructing the Fastrak test wheel and Fastrak transducer attachments. Dr. Andrew Coleman and Dr. John Hearns of the medical physics department, for helpful discussions and checking parts of the thesis. Anabel Langton, Lucy Buxton, Clear Casey and Helen Otton of Tommy's Campaign. For their unstinting support. BT for providing most of the funding for this project. Acuson UK for the loan of a 128XP/3 ultrasound scanner for six months of the project. The hospital carpenters for making the wooden Fastrak transmitter stand. Last, but not least, I would like to thank my supervisor, Dr.Rodney Sheppard of King's College London.